

Capturing the dynamics of Direct Contact Condensation

Citation for published version (APA):

Safavi Nic, S. S. (2023). *Capturing the dynamics of Direct Contact Condensation: A numerical and experimental study*. [Phd Thesis 1 (Research TU/e / Graduation TU/e), Chemical Engineering and Chemistry]. Eindhoven University of Technology.

Document status and date:

Published: 09/10/2023

Document Version:

Publisher's PDF, also known as Version of Record (includes final page, issue and volume numbers)

Please check the document version of this publication:

- A submitted manuscript is the version of the article upon submission and before peer-review. There can be important differences between the submitted version and the official published version of record. People interested in the research are advised to contact the author for the final version of the publication, or visit the DOI to the publisher's website.
- The final author version and the galley proof are versions of the publication after peer review.
- The final published version features the final layout of the paper including the volume, issue and page numbers.

[Link to publication](#)

General rights

Copyright and moral rights for the publications made accessible in the public portal are retained by the authors and/or other copyright owners and it is a condition of accessing publications that users recognise and abide by the legal requirements associated with these rights.

- Users may download and print one copy of any publication from the public portal for the purpose of private study or research.
- You may not further distribute the material or use it for any profit-making activity or commercial gain
- You may freely distribute the URL identifying the publication in the public portal.

If the publication is distributed under the terms of Article 25fa of the Dutch Copyright Act, indicated by the "Taverne" license above, please follow below link for the End User Agreement:

www.tue.nl/taverne

Take down policy

If you believe that this document breaches copyright please contact us at:

openaccess@tue.nl

providing details and we will investigate your claim.

Capturing the dynamics of Direct Contact Condensation

A numerical and experimental study

S.S. Safavi Nic

Nederlandse titel: Het vastleggen van het dynamische gedrag van Directe Contact Condensatoren: modellering en experimentele studie van stoom injectoren

Copyright © 2023 by S.S. Safavi Nic, Eindhoven, The Netherlands.

All rights reserved. No part of the material protected by this copyright notice may be reproduced or utilised in any form or by any means, electronic or mechanical, including photocopying, recording or by any information storage and retrieval system, without the prior permission of the author.

A catalogue record is available from the Eindhoven University of Technology Library
ISBN: 978-90-386-5824-7

Cover images licensed via Adobe Stock

Printed by: ADC Nederland

Capturing the dynamics of Direct Contact Condensation

A numerical and experimental study

Proefschrift

ter verkrijging van de graad van doctor aan de Technische
Universiteit Eindhoven, op gezag van de rector magnificus,
prof. dr. S.K. Lenaerts, voor een commissie aangewezen
door het College voor Promoties, in het openbaar te
verdedigen op 9 oktober 2023 om 13:30 uur

door

Seyyed Sherwin Safavi Nic
geboren te Teheran, Iran

Dit proefschrift is goedgekeurd door de promotoren en de samenstelling van de promotiecommissie is als volgt:

Voorzitter: Prof. dr. ir. M. Sint Annaland
1^e promotor: Prof. dr. ir. J.A.M. Kuipers
Co-promotor: Dr. ir. K.A. Buist

Leden: Prof. dr. ir. N.G. Deen
Prof. dr. ir. A. van der Schaaf
Prof. dr. ir. C Poelma Technische Universiteit Delft
Prof. dr. ing. M. Schluter Technische Universität Hamburg
dr. ir. M.A.I. Schutyser Wageningen Univeristy & Research

Het onderzoek of ontwerp dat in dit proefschrift wordt beschreven is uitgevoerd in overeenstemming met de TU/e Gedragscode Wetenschapsbeoefening.

To those who supported and inspired me

Summary

To ensure a certain level of food safety in dairy products it is required to apply heat treatment to inactivate micro-organisms and/or harm-full enzymes which naturally occur in the ingredients. Direct Contact Condensation is a suitable technology in which steam is directly brought into contact with the product to achieve a fast heating rate, reaching higher temperatures and as consequence intensify the process and minimize product damage. However, when the mixing of the two fluids is not done efficiently it can cause severe damage to the product resulting in a loss of quality and even loss in production efficiency. Modelling the transport phenomena in DCC is beneficial to optimize the process however experimental data for validation was lacking.

In this work an experimental set-up was presented in which a transparent steam injector was incorporated to visualize the steam cavity. The steam cavity was recorded using a high speed camera and an image processing protocol was developed to analyze the data. The experimental data and image analysis supplemented with temperature and pressure measurement, were processed with Machine Learning (ML) models to develop a data driven model to predict the regime maps. The ML algorithms identified that the best parameters to generate condensation regime maps are the steam pressure, subcooling temperature, water Prandtl number, velocity ratio between gas/liquid and the channel pressure. The condensation outcomes were presented with various two-dimensional regime maps. New regime maps are proposed using the Prandtl number and velocity ratio as dimensionless parameters. When introducing a second steam cavity it was found that this cavity influenced the temperature gradient to such an extent that the two jets show oscillating behaviour, which has been classified as "*Interfacial oscillation*". Increasing the channel pressure reduces the regime map such that only chugging and bubbling regime were observed.

The regime maps are a useful tool to identify what type of flow regime is to be expected when operating a DCC process. It however does not provide insights in the transport phenomena or determine the performance of the process. The use of validated, transient models to predict temperature, phase fraction and velocity gradients is essential and can improve the operation of DCC. It was chosen to develop a one-dimensional two-fluid model to gain on computational speed. The benefit of this approach is that the model can simulate time-scales up to hours to match the time-scales of protein induced fouling. The model was tested against a wide range of steam mass fluxes, inlet water temperatures, water Reynolds number and channel pressures to prove the steady-state performance. In addition two dynamic tests were conducted in which the water flow rate was step wise decreased or the steam pressure was adjusted throughout the experiment. In general the model showed good agreement provided that the flow inside the channel was homogeneous.

Whilst the 1D model performed well and showed good agreement with experimental data it also demonstrated that it requires homogeneous flow. The use of a Computational Fluid Dynamics (CFD) model is useful to investigate flow directionality, temperature gradients

and to optimize the injector design. The CFD model presented in this work uses an Eulerian Multiphase model (EMP) with a RANS $k-\omega$ turbulence model. The experimental data generated was only suitable for qualitative validation due to the formation of large gas bubbles as well as the volume averaged velocity profiles due to the LED front lighting. The experimental data was obtained using a high-speed camera and PIVlab to obtain velocity fields. The model does produce a similar flow structure, and velocity gradients. Local hotspots were detected in the predicted temperature fields when the "jetting" regime was observed. The simulations for the experiments in the "bubbling" regime featured a large radial temperature gradient which is inline with the observations with the 1D model.

The objective of high heat treatment, using Direct Contact Condensation (DCC), is to ensure a high level of food safety. The industrial challenge, in the food industry, is to balance food safety with product quality and process efficiency. The product quality is affected by several heat induced side reactions such as maillard and protein denaturation. The process efficiency is mostly determined by protein fouling as a consequence of denaturation. The formation of a protein rich deposit layer causes fouling of the system resulting in a loss of effective production time and an increase in cleaning cycles. To model this phenomena a transient flowsheet model was developed that features a laminar flow heat-exchanger and a steam injector. Protein denaturation was modelled using a reversible unfolding reaction step followed by a pseudo second order aggregation step. Pilot scale experiments were conducted to generate samples throughout the process to determine the degree of denaturation and validate the model. The formation of the deposit layer is described in the segment after the DCC using a flow averaged model incorporating diffusion of species through the mass boundary layer as well as adsorption to the wall and desorption from the wall. The addition of desorption kinetics was necessary to incorporate the increase of friction due to decreasing hydrodynamic area. The model shows good agreement with experimental data and is capable of capturing the process dynamics, both for the heat exchanger and the DCC. The deposit layer formation model is in agreement with the trend observed in the experimental data but is not fully capturing the process dynamics.

Samenvatting

Om een hoog niveau van voedselveiligheid te garanderen, en daarbij een langere houdbaarheid datum, krijgen zuivel producten een hitte-behandeling om bacteriën en enzymen te deactiveren. Verhittings technieken waarbij verzadigde stoom rechtstreeks in het product wordt geïnjecteerd genieten de voorkeur vanwege de snelle energie overdracht en korte proces tijden. Hierdoor wordt het risico op product schade zoals Maillard reacties of eiwit denaturatie verminderd. Dit is echter wel op voorwaarde dat de twee stromen (stoom en product) homogeen mixen en recirculatie vermeden wordt. Wanneer dit niet het geval is dan is er een risico dat het product wordt oververhit waardoor het product significante schade oploopt dat impact zal hebben op geur, kleur en smaak. Daarnaast zal de productie lijn, als gevolg van eiwit reacties, vervuild raken waardoor de productie kosten oplopen door verlies in operationele efficiëntie en toename in schoonmaak cycli. Het kan voordelig zijn om de impact van het toegepaste proces (de techniek als mede de operationele condities) op de product kwaliteit en proces efficiëntie vooraf te voorspellen om zodoende het proces te optimaliseren en risico's te verminderen.

Om het voorspellend vermogen van een model te valideren, is het noodzakelijk om kwalitatief sterke experimentele data te verzamelen. Hiervoor was een pilot schaal experimentele opstelling ontworpen waarin een stoom injector met een transparant segment was verwerkt. Het transparante segment, waarin een saffier glasplaat is verwerkt, werd verlicht met 2 LED lampen en de stoom pluim werd opgenomen met een hoge-snelheids camera. Een combinatie van camera beelden en sensor data zijn geanalyseerd met behulp van Machine Learning (ML) algoritmes. Hieruit werden de belangrijkste parameters die het proces beïnvloeden geïdentificeerd. Parameters zoals Prandtl getal, snelheid ratio's tussen stoom/product, subcooling temperatuur, stoomdruk en kanaaldruk zijn gebruikt om de condensatie regimes in kaart te brengen. Deze techniek was ook valide met de introductie van een tweede stoom pluim en identificeerde een extra regime ("*Interfacial oscillation*") als gevolg van fluctuerende temperatuur gradiënten.

De condensatie kaarten zijn nuttige middelen om een inschatting te maken van wat voor type gedrag de stoom pluim zal vertonen onder bepaalde operationele condities. Ze geven echter geen inzicht in temperatuur gradiënten. Om dit te voorspellen is een een-dimensionaal dynamisch model ontwikkeld om stof en warmte overdracht te berekenen. Het voordeel van dit model is de snelle convergentie, dat in een aantal seconden plaats vind, en hierdoor kan het model toegepast worden om lange productie tijden te simuleren. Dit is relevant omdat eiwit vervuiling op dezelfde tijdschaal plaats kan vinden. Het model was getest tegenover stationaire data om zodoende de macroscopische voorspellingen te valideren. Daarnaast werd het model ook getest tegenover dynamische data waarin het waterdebiet stapsgewijs werd aangepast en de stoomdruk werd gevarieerd. Voor beide dynamische testen reageerde het model adequaat en betrouwbaar mits de stroming in het kanaal homogeen was. Voor experimenten waarbij de stoom pluim marginaal het kanaal penetreerde, en daardoor een radiale temperatuur gradiënt veroorzaakte, waren de resultaten minder betrouwbaar.

Doordat het 1D model vooral werkt onder voorwaarde dat de stroming homogeen is, is het noodzakelijk om een Computational Fluid Dynamics (CFD) model te ontwikkelen. Dit type model is in staat om de drie-dimensionale stroming te modelleren en hiermee de vloeistof stroming (snelheid en richting) en temperatuurgradiënten te bepalen. Hiermee kan het ontwerp van de injector geoptimaliseerd worden of condities bepaald worden waarin de stroming al dan niet homogeen is. In dit CFD model is de meer fase fysica gemodelleerd als Eulerian-Eulerian meer-fase met een $k-\omega$ RANS model. Om dit model te valideren zijn de beelden van de hoge-snelheids camera geanalyseerd met behulp van PIVlab om de snelheid en richting in kaart te brengen. De beperkingen van deze methode zijn enerzijds afkomstig van de belichtingsmethode. Door de LED lampen die aan het vooraanzicht geplaatst zijn, naast de camera, ontstaat er een volume gemiddelde snelheid vector. Dit maakt een directe vergelijking met model data onmogelijk. Een andere beperking was fysisch bepaald doordat er grote gasbellen gevormd werden die invloed uitoefenen op de meetmethode. Hierdoor zijn de experimentele resultaten enkel geschikt voor een kwalitatieve validatie. De model resultaten kwamen overeen met de gegenereerde snelheidsvectoren en lieten dezelfde recirculatie patronen zien. De analyse van de temperatuur voorspellingen lieten zien dat condities waarin een "jet-condensatie regime ontstond, dat de recirculatie patronen verantwoordelijk zijn voor oververhitting. De condities waarin "bubbel-condensatie plaats vond resulteerde in marginale stoom pluim penetratie en daardoor tot een radiale temperatuurgradiënt.

De industriële uitdaging voor hittebehandeling is om een balans te vinden tussen voedselveiligheid, productkwaliteit en productie-efficiency. De laatste twee aspecten worden vooral bepaald door hittegevoelige reacties zoals eiwit denaturatie en vervuiling. De formatie van een eiwitrijke vervuiling laag zorgt ervoor dat productietijden verkort worden en schoonmaak cycli toenemen. Om dit proces te modelleren zijn experimenten op proef-fabriek schaal uitgevoerd waarin twee laminaire buizen warmtewisselaar de voorverwarming van het product verzorgden en een stoom-injector om de sterilisatiegraad te behalen. Dit proces is in zijn geheel gemodelleerd met behulp van een flowsheet model waarin alle productiestappen verwerkt zijn. De eiwit reacties zijn verwerkt in een drie-staps reactie model met daarin een reversibele ontvouwing en een tweede orde aggregatie reactie. Het reactie model is gevalideerd tegenover monster analyse uit de proeffabriek experimenten en de druksensoren zijn gebruikt om het vervuilingsmodel te valideren. Het vervuilingsmodel is geïmplementeerd in het stromingsmodel na de stoom-injector en bevat een adsorptiemodel van bulkvloeistof naar de wand alsmede een desorptiemodel als gevolg van turbulente fricties. De procesdynamiek werd goed door het model gerepresenteerd en het effect van de formatie van de vervuiling slaag op de procesdruk werd accuraat voorspeld.

Contents

Summary	i
Samenvatting	iii
Contents	vi
1 Introduction	1
1.1 Direct Steam Injection	3
1.2 Heat induced protein reactions	4
1.3 Thesis outline	9
References	11
2 An objective classification of condensation regimes in Direct Contact Con- densation	15
2.1 Introduction	17
2.2 Materials and methods	19
2.3 Machine learning models	24
2.4 Results and discussion	26
2.5 Conclusion	37
References	39
3 A transient mechanistic two-fluid model for Direct Contact Condensation	41
3.1 Introduction	43
3.2 Model description	45
3.3 Materials and methods	52
3.4 Results and discussion	54
3.5 Conclusion and future work	58
References	59
4 A Computational Fluid Dynamics model to analyze the mechanics inside a Steam Injector	61
4.1 Introduction	62
4.2 Model description	64
4.3 Eulerian Multiphase Flow	64
4.4 Materials and methods	68
4.5 Experimental set-up	69
4.6 Results and discussion	72
4.7 Conclusion	76
References	77

5	Dynamic model to predict heat-induced protein denaturation and fouling in a Direct Contact Steam Condensation process	79
5.1	Introduction	81
5.2	Model description	83
5.3	Model implementation and verification	89
5.4	Materials and methods	93
5.5	Results and discussion	94
5.6	Conclusion	100
	References	101
6	Epilogue	105
6.1	Conclusions	105
6.2	Outlook	107
	References	108
	List of publications	109
	Acknowledgements	111
	Curriculum Vitae	115
7	Appendix A	117

Chapter 1

Introduction

Heat treatment is applied in the food industry to ensure a certain level of food safety for the final product by inactivating micro-organisms and/or harmful enzymes which naturally occur in the ingredients. The level of required food safety is strongly related to the target group of the product and is directly linked to the applied temperature and the duration at which this temperature is maintained. Fresh dairy products, for instance, require a minimum pasteurization time of 30 min at 69°C (or 30 seconds at 80°C). However, dairy products that need to remain stable on the shelf at ambient conditions require a more strict heat treatment in the temperature range of 135-150°C to also destroy spore-forming bacteria [1-3]. The objective of heat treatment is to achieve a certain degree of inactivation of bacteria. This is expressed using the F_0 -value given by Equation 1.1 in which Δt is the average residence time, T the target temperature, T_{ref} and z_{ref} are respectively the reference temperature and temperature resistance coefficient for the species of interest [4].

$$F_0 = \Delta t 10^{\frac{(T - T_{ref})}{z_{ref}}} \quad (1.1)$$

When indirect heating technologies are employed, the heating rate is significantly low and therefore the product can get severely damaged and which results in a lower sterilization temperature for longer time to achieve the desired F_0 -value. With direct contact heating the heating rate is fast and therefore a higher temperature for a short time is achievable to reach the same F_0 -value as when working with indirect heating technologies. An example of these differences for a $F_0 = 6$ min is given by Figure 1.1. This process intensification is beneficial for product stability as well as process efficiency. The drawback of Ultra High Heat-Treatment (UHT) temperature regimes is the additional side reactions that may cause colour formation, loss of nutrients [5] and a reduced process efficiency [6-8]. The reduction in process efficiency is a result of the formation of a protein-rich deposit (fouling) layer, which increases the resistance for heat transfer. The consequences are a higher energy consumption to compensate for the loss in efficiency for energy transfer as well as an increase of the amount of cleaning cycles. Both of these have a significant impact on the sustainability of dairy processing as well as on the optimal utilization of processing equipment.

In order to increase the food safety and minimize the rate of chemical reactions it can be favorable to apply direct heating technologies instead of indirect heating technologies.

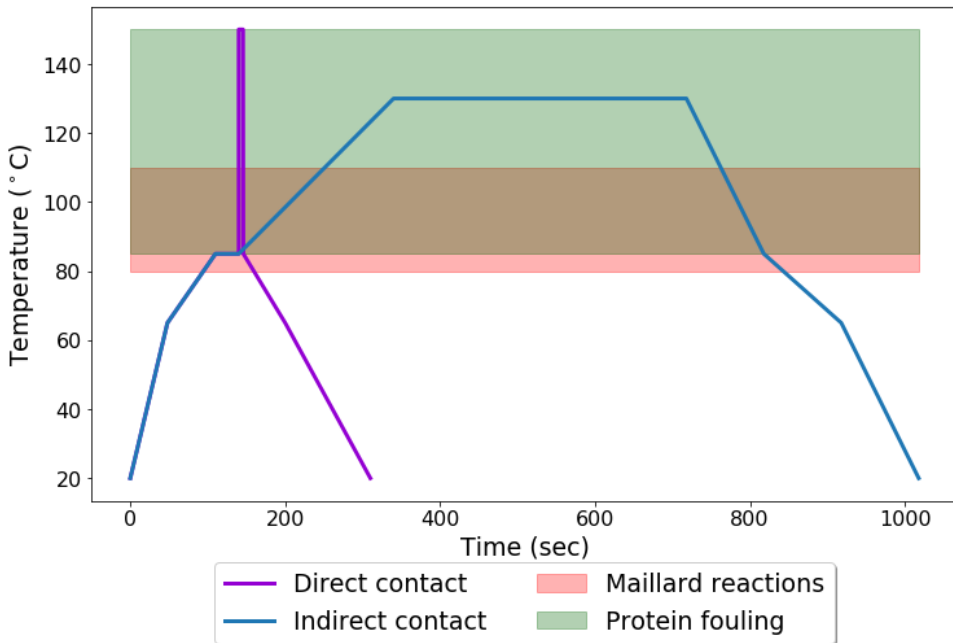


Figure 1.1: A comparison between UHT process with direct and indirect heating technologies. The pre-heating is generally the same in which indirect heating methods are used to pre-heat the product until 85°C . After this step, with direct heating technologies, the product is heated to 150°C and kept at that temperature for a short time. Using a vacuum vessel the added steam is flashed and the product is cooled and afterwards indirect heating methods are used to further cool the product. Both processes achieve a $F_0 = 6$ min.

The latter features a slow heating rate and as a result the side reactions are more severe. There are two options for direct heating methods: Direct Steam Injection (DSI) and Steam Infusion (SI). Malgren et al. [9] found that both technologies provide food safe products with no significant differences in chemical composition. The main difference is in the particle size distribution of the large protein aggregates which can result from the bubble formation during steam injection. However in practice this depends on the type of steam injector used. In industrial applications it is most common that the DSI is applied for low solid content processes (up-to 35% dry matter) and the SI unit for high solid content processes (up-to 50% dry matter). At this stage the hypothesis is that the bubble formation by steam injection causes the larger aggregates, however, it is not clear what the exact effect of different types of injectors is on the heat-transfer and reaction pathways and associated chemical kinetics. To study this phenomena it would be necessary to develop models to predict the condensation behaviour and study the impact on protein reactions. This thesis focusses on the application of a DSI as it is mostly used in the industry.

The most commonly applied model for protein denaturation and fouling is the model described by De Jong et al. [7]. This model describes the process of fouling related to

the denaturation of β -lactoglobulin, by considering three states of the protein: native, unfolded and aggregated. Furthermore the model assumes a pseudo-second order reaction for aggregation and a first order denaturation of the native β -lactoglobulin [10]. This relatively simple description of the reaction mechanism does not take into account the refolding of the Whey protein [11]. As a result the total amount of denatured protein is over-estimated [9] and the location of fouling deposit is estimated wrongly. Furthermore it leaves out the effect of pH and presence of minerals in solution or ionic strength, which can have a radical outcome on reaction kinetics of aggregation with only a small change in concentration [12–14]. Currently most literature describes the effect of these parameters in a qualitative manner, a quantitative description of these phenomena, however, has not yet been reported.

1.1 Direct Steam Injection

There are two methods for direct heating: steam injection and steam infusion. Both mechanisms achieve high heating rates and allow direct contact condensation (DCC). For steam injection, pressurized steam is injected and condensed into the stream of flowing milk. For steam infusion the milk is sprayed into a steam infusion chamber. Steam infusion is far more expensive to apply in the industry. It can be used to process milk concentrates up to 50% dry matter whilst an injector is limited to 30% dry matter. Both systems dilute the milk and thus increase the milk volume. The steam that is condensed into the milk is removed by vaporization in a vacuum chamber after the sterilization step[15].

Direct steam injection can cause high temperature and velocity gradients. One of the challenges of DCC is to uniformly distribute the heat through the processing unit. Direct heating will, if poorly executed, cause a non-uniform product. Parts of the product stream will contain denatured proteins due to extensive overheating. Furthermore, parts might not be heated enough to destroy the bacterial spores that can cause spoilage. However, the intended result of direct steam injection, if executed right, would lead to a uniform product stream with limited protein denaturation, while still destroying all biological material. Extensive research into the steam injection process could prevent design flaws.

There are different types of steam injectors. The injector in Figure 1.2 is an example of cross injection of steam into a cold product stream[16, 17].

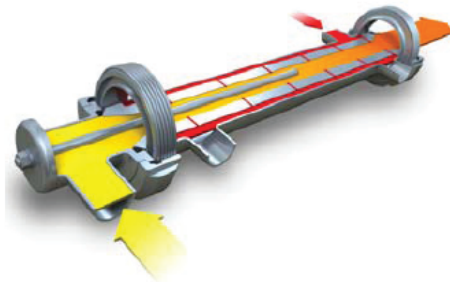


Figure 1.2: A steam injector[18]

The injector in Figure 1.2 is a direct steam injector using a manifold. The manifold has several nozzles, located in the wall of the inner pipeline. Steam is added in the outer cylinder of the manifold counter-currently, whilst the product stream runs through the inner pipe. The pressure of the steam is higher than the pressure of the product stream, ensuring that steam flows through the nozzles, condensing into the product[18]. There is still much to know about the mixing and heating rate of a manifold injector. A numerical study could help fine-tune a multiple hole injection system, to ensure good mixing rates in order for the product to be uniformly heated. An accompanying experimental study is necessary to validate numerical models.

1.2 Heat induced protein reactions

When milk is heated a number of different chemical reactions occur that change the physics and chemistry of the product. The chemical reactions that are of interest and relevant for this work are those that impact the protein. Therefore this section will focus on protein reactions.

1.2.1 Whey protein interactions

Whey proteins are nowadays popular amongst athletes as they have a well-recognized nutritional benefit such as protection to muscle loss, enhanced muscle synthesis and improved glycemic control [19–22]. In bovine milk whey proteins account for roughly 20% of the proteins. In this section the structure and stability of whey proteins are discussed.

Table 1.1: Composition of Whey proteins per kg bovine milk [23]

Component	amount (wt%)	diameter (nm)
Whey	6.0-6.2	
β -lactoglobulin	3.1-3.5	7
α -lactalbumin	1.2-1.3	3.5
BSA	0.4	12
Other	1.9-2.3	7-12

Whey proteins (listed in Table 1.1) are globular proteins with a well defined tertiary structure when in native state. The forces that are responsible to maintain this structure are:

- Covalent disulphide bonds
- Electrostatic forces
- Hydrophobic interactions
- Ionic bonds (salt bridges)
- van der Waals forces
- Hydrogen bonds

The covalent disulphide bonds are not only responsible for the protein structure (intramolecular force) but also play an important role for protein aggregation (intermolecular force) upon disruption of this tertiary structure. In general the stability of the globular protein is either disrupted by strong pH variations or by temperature. In this work the stability is mostly effected by temperature which causes the unfolding of the protein (i.e. the tertiary structure is lost). As a result reactive groups are exposed which can result in protein aggregation. The unfolded protein can also fold back into a (misfolded) native protein. The aggregated protein is viewed to be a denatured protein.

Effect of pH on whey protein stability

The pH of the system has a strong influence on the stability of the protein structure, both for Whey and Casein proteins. The electrostatic interactions of proteins are influenced by the pH. The proteins contain several amino acids with ionizable groups such as Aspartic Acid (Asp), Glutamic acid (Glu), Lysine (Lys), Arginine (Arg) and Histine (His). The net charge of the protein molecule at a neutral pH is either positive or negative depending on the relative number of charged amino acids that are present in the structure. At the isoelectric pH (pI) the net charge of the protein is zero [24]. The electrostatic interaction can influence the attractive/repulsiveness of intramolecular interactions but may also influence the intermolecular interactions by strengthening the interaction between the internal amino groups. It is expected that for pH higher then the pI that the electrostatic repulsion increases.

Next to the electrostatic interaction, the pH also influences the reactivity of the free SH-groups, which has the ability to form disulfide bridges intra as well as inter molecular. The free SH groups are active between $6.5 < pH < 8$ and form the strongest links for aggregation in this range [25, 26]. This was also found in the result of Leeb et al. [13] in which the particle size decreased with increasing pH.

1.2.2 Whey-Casein interactions

The major part of the protein composition in bovine milk consists of caseins ($\sim 80\%$ of all proteins). Normally the casein protein is found in a micellar form of which the debate regarding its structure is still ongoing. The casein protein is a cluster of different types of casein as listed by Table 1.2. Currently the main accepted model of the casein micelle is the

model of Holt et al. [27]. The model emphasises the role of a colloidal calcium phosphate, in which calcium is bound by (in)organic phosphates, that acts as an important building block. The micelle is stabilized both by electrostatic and by steric repulsion by κ -casein which is located at the surface which causes the micelle to be "hairy". The exact shape and size of the micelle is however still under debate as the sample preparation influences the micelle.

Table 1.2: Composition of Casein per kg bovine milk [28]

Component	amount (wt%)
Casein	26.92
α_{s1} -Casein	10.25
α_{s2} -Casein	2.75
β -Casein	9.6
κ -Casein	3.45

The interaction of the casein micelle and whey proteins (WP) occurs via κ -casein located at the micelle surface. The reaction pathway schematic (Figure 1.3) gives a proper representation of the different phenomena [29]. Via pathway A the whey proteins form primary whey protein aggregates which either remain in the liquid phase or can bind itself to the casein micelle. Alternatively an unfolded whey protein can attach itself to the casein micelle (pathway B). The complex formation of WP and κ -casein might as well take place in the liquid phase after the dissociation of κ -casein following pathway C or larger aggregates are formed after dissociation of complexes from the micelle surface (pathway D).

These reaction pathways are highly influenced by process conditions as well as the pH, calcium level and concentration of lactose. Especially the dissociation of κ -casein and the micelle bound complexes is influenced by the pH.

In the range of $6.0 < \text{pH} < 8.0$ the main driver of protein aggregation are the free thiol-groups. With increasing pH more thiol groups are activated and thus the reactivity increases [25, 26]. This also influences the reaction pathway for casein-whey interaction as illustrated in Figure 1.4 from the work of Vasbinder et al. [30]. At low pH the amount of activated thiol-groups is low and the aggregates that are being formed are large and stick to the surface of the micelle [30, 31]. With increasing pH the denatured WP will form a mono-layer at the surface of the casein micelle. With a near-neutral pH complexes are found in the liquid phase (pathway A and B). It is thus in line with the work of Leeb et al. [13] who concluded that the size distribution decreases with increasing pH. It is worthwhile to note that Anema et al. [32] concluded that (within the range $6.5 < \text{pH} < 6.7$) the main cause of changes in casein micelle size was by whey-protein aggregation but that the association rate between whey and casein was much lower than the loss in native protein.

In practice the (high protein) dairy products are produced in a pH range of $6.5 < \text{pH} < 6.9$. Within this range the reaction between κ -casein and unfolded β -lactoglobulin takes place at the surface of the casein micelle. Therefore it is proposed to adjust the aggregation reaction to take into account the reaction between WP and casein in the productional range. It is not favorable to go above or below this pH range. Below this pH range the recipe is highly instable as the aggregation goes fast due to lower repulsions as the

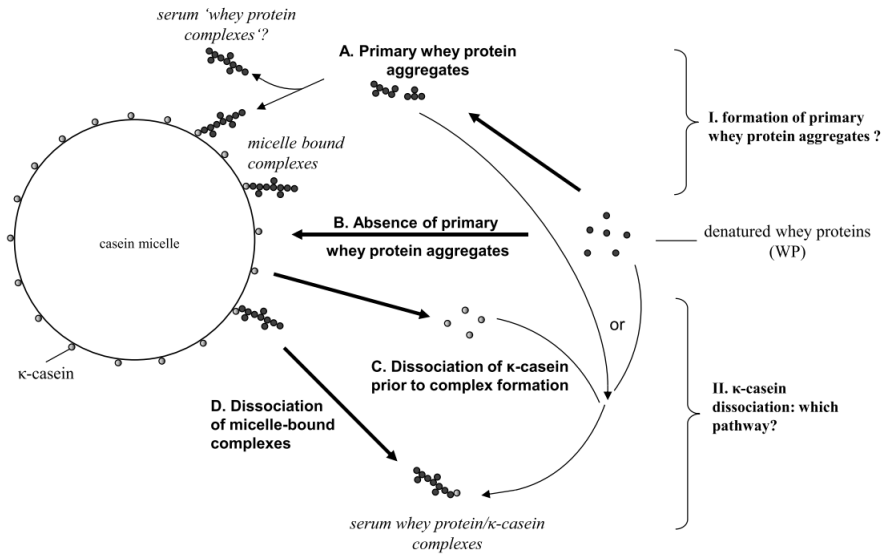


Figure 1.3: Schematic overview of the reaction pathways for protein aggregation [29]. The casein micelle has a radius of 50nm and β -lactoglobulin has a radius of 3.5nm [27].

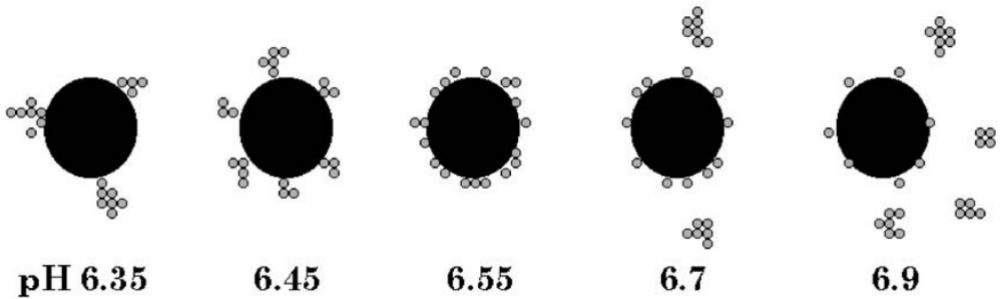


Figure 1.4: Schematic representations of the interaction of casein micelles and whey proteins at different pH values [30].

pH moves towards the iso-electric point. Above this pH range the casein micelle loses integrity as κ -casein starts to dissociate and the micelle becomes heat-sensitive. As a consequence the micelles loses the steric repulsion and simultaneously the electrostatic repulsion decreases. Equation 1.2 represents the reaction between unfolded whey protein (c_U) and Casein (c_C) both with an unidentified reaction order (n_1 and n_2)



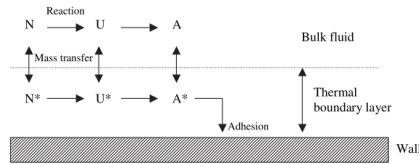
1.2.3 Protein fouling

Fouling in heat-exchangers and holding cells limit both production time and cause a loss in efficiency in heat transfer. The mechanism of fouling as well as the composition of the fouling layer has been investigated extensively over the last decade but there is no alignment on the exact mechanism of fouling. Moreover the models published have only been validated for temperatures lower than $T < 95^{\circ}\text{C}$. The differences in protein composition found in Table 1.3 show that it might not be feasible to have a single reaction model in place. In high-protein production, both on factory and pilot plant scale, it was observed that the pipes and heat-exchangers are completely blocked during thermal processing when the temperature approaches the UHT region (i.e. $T > 100^{\circ}\text{C}$).

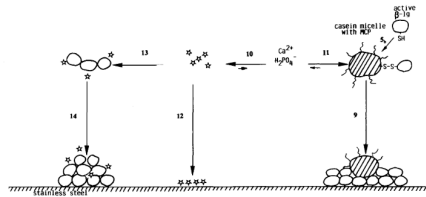
Table 1.3: Composition (% DM) of type A deposit layer ($T < 100^{\circ}\text{C}$) and type B ($T > 100^{\circ}\text{C}$) deposit layer in of a PHE with comparison to bulk fluid composition.

	T < 100°C [33]		T > 100°C [34]	
Component	Skimmed Milk	Deposit	Whole Milk	Deposit
Total Protein	37.20	44.40	26.83	15-20
Whey	6.10	33.30	5.37	3.45-4.6
Casein	31.10	11.10	21.50	11.55-15.40
Minerals	7.40	45	5.69	70-80
Calcium	1.32	15.70	-	-
Phosphate	2.04	23.00	-	-
Lactose	52.60	0.02	39.84	-

The model of de Jong et al. [10] is at this moment the most accepted fouling model and has been applied by various researchers [35, 36]. The mechanism of fouling is however still a matter of debate. In line with the findings in Table 1.3 Visser et al. [33] proposed to correlate the reaction mechanism to the concentration of whey proteins for temperatures lower than 100°C . Even though they found traces of casein in the deposit layer it was assumed that the casein micelles are entrained by whey proteins rather than participating in the reaction (Figure 1.5b). It is known that non-soluble minerals play a role in deposit layer formation but it is not clear what this role exactly is and which layer is formed first, proteins or minerals [33, 37]. The reaction model proposed by de Jong et al. [10] follows the conclusions of Visser et al. [33] and proposes to link the model to the unfolded whey protein as this intermediate state contains the reactive thiol groups that may cause the deposit formation. Another reaction mechanism was proposed by Georgadis et al. [35] in which they developed a model including a hydrodynamic boundary layer in which the deposit layer is formed. Interestingly no motivation was given whether the aggregates are responsible for the formation of the deposit layer.



(a) Mechanism proposed by [35]



(b) Complex mechanism with the interplay of whey/casein and salt particles [33].

Figure 1.5: Mechanisms of fouling

As the experimental data that was used to derive these models was obtained for temperature ranges between $65^\circ\text{C} < T < 95^\circ\text{C}$ it can be that these models are not valid at higher temperatures. Based on the finding of Burton et al. [34] it is likely that the reaction mechanism and related model is casein dominated for UHT temperature ranges. It is therefore important to have data on the protein composition to establish the right model and to validate the kinetic model.

1.3 Thesis outline

The outline of this thesis is as follow:

- **Chapter 2:** This chapter presents the experimental set-up and the generation of regime maps to describe the process mechanisms. A machine learning algorithms were employed to identify the key-influencing parameters, optimize the regime maps and develop a predictive model.
- **Chapter 3:** In this chapter a one-dimensional transient model is presented to predict the performance of a DSI, the temperature, velocity and pressure gradients. The benefits of this modelling approach is the low computational costs whilst being accurate.
- **Chapter 4:** Whilst the 1D model demonstrated good agreement with experimental data it also demonstrated that it works best for homogeneous flow conditions. In this chapter a CFD model is presented that is suitable to assess the flow homogeneity and predict temperature gradients. Such a model is beneficial to support equipment design.

- **Chapter 5:** In this chapter a model is presented to predict the performance of a pilot-plant line that contains tubular heat-exchangers and a DSI. This model predicts the performance of the equipment, the temperature gradient and pressure profiles. This information is crucial to predict the denaturation of proteins and fouling in the DSI.

References

- [1] EFSA. “Opinion of the Scientific Panel on Biological Hazards on *Bacillus cereus* and other *Bacillus* spp in foodstuffs .” *The EFSA Journal* 1 (2005), pp. 1–48.
- [2] P.E. Granum and T. Lund. “*Bacillus cereus* and its food poisoning toxins”. *FEMS microbiology letters* 157.2 (1997), pp. 223–228.
- [3] A. Rajkovic, N. Smigic, and F. Devlieghere. “Contemporary strategies in combating microbial contamination in food chain”. *International Journal of Food Microbiology* 141 (2010), S29–S42.
- [4] J.v. Doornmalen and K. Kopinga. “Temperature dependence of F-D- and z-values used in steam sterilization process”. *Journal of applied microbiology* (2009), pp. 1054–1060.
- [5] M. Van Boekel. “Effect of heating on Maillard reactions in milk”. *Food Chemistry* 62.4 (1998), pp. 403–414.
- [6] P. Blanpain-Avet, C. André, M. Khaldi, *et al.* “Predicting the distribution of whey protein fouling in a plate heat exchanger using the kinetic parameters of the thermal denaturation reaction of β -lactoglobulin and the bulk temperature profiles”. *Journal of Dairy Science* 99.12 (2016), pp. 9611–9630.
- [7] P. de Jong, M.C. te Giffel, H. Straatsma, and M.M. Vissers. “Reduction of fouling and contamination by predictive kinetic models”. *International Dairy Journal* 12.2-3 (2002), pp. 285–292.
- [8] T. Davies, S. Henstridge, C. Gillham, and D. Wilson. “Investigation of whey protein deposit properties using heat flux sensors”. *Food and Bioproducts processing* 75.2 (1997), pp. 106–110.
- [9] B. Malmgren, Y. Ardö, M. Langton, *et al.* “Changes in proteins, physical stability and structure in directly heated UHT milk during storage at different temperatures”. *International dairy journal* 71 (2017), pp. 60–75.
- [10] P. de Jong. *Modelling and optimization of thermal processes in the dairy industry*. Delft University of Technology: ISBN:90-9009034-7, 1997.
- [11] X.D. Chen, Z.D. Chen, S.K. Nguang, and S. Anema. “Exploring the reaction kinetics of whey protein denaturation/aggregation by assuming the denaturation step is reversible”. *Biochemical Engineering Journal* 2.1 (1998), pp. 63–69. DOI: 10.1016/S1369-703X(98)00018-7.
- [12] H.B. Wijayanti, N. Bansal, and H.C. Deeth. “Stability of Whey Proteins during Thermal Processing: A Review”. *Comprehensive Reviews in Food Science and Food Safety* 13.6 (2014), pp. 1235–1251. DOI: 10.1111/1541-4337.12105.
- [13] E. Leeb, N. Haller, and U. Kulozik. “Effect of pH on the reaction mechanism of thermal denaturation and aggregation of bovine β -lactoglobulin”. *International Dairy Journal* 78 (2018), pp. 103–111.
- [14] V. Liyanaarachchi, W.S. “Caseins and their interactions that modify heat aggregation of whey proteins in commercial dairy mixtures”. *International Dairy Journal* (2018). DOI: 10.1016/j.neubiorev.2016.08.016.

References

- [15] N. Datta, A. Elliot, M. Perkins, and H. Deeth. *Ultra-high-temperature (UHT) treatment of milk: Comparison of direct and indirect modes of heating*. 2002.
- [16] A. Shah, I.R. Chughtai, and M.H. Inayat. “Experimental study of the characteristics of steam jet pump and effect of mixing section length on direct-contact condensation”. *International Journal of Heat and Mass Transfer* 58.1-2 (2013), pp. 62–69. DOI: 10.1016/j.ijheatmasstransfer.2012.11.048.
- [17] Y. Takeya, S. Miwa, T. Hibiki, and M. Mori. *Application of steam injector to improved safety of light water reactors*. Jan. 2015. DOI: 10.1016/j.pnucene.2014.07.045.
- [18] F. Innings and L. Hamberg. “Steam condensation dynamics in annular gap and multi-hole steam injectors”. *Procedia Food Science* 1 (2011), pp. 1278–1284. DOI: 10.1016/j.profoo.2011.09.189.
- [19] D.K. Layman. “The Role of Leucine in Weight Loss Diets and Glucose Homeostasis”. *The Journal of Nutrition* 133.1 (2003), 261S–267S. DOI: 10.1093/jn/133.1.261S.
- [20] D.K. Layman and J.I. Baum. “Dietary Protein Impact on Glycemic Control during Weight Loss”. *The Journal of Nutrition* 134.4 (2004), 968S–973S. DOI: 10.1093/jn/134.4.968S.
- [21] S. Séverin and X. Wenshui. “Milk Biologically Active Components as Nutraceuticals: Review”. *Critical Reviews in Food Science and Nutrition* 45.7-8 (2005). PMID: 16371332, pp. 645–656. DOI: 10.1080/10408690490911756.
- [22] E. Ha and M.B. Zemel. “Functional properties of whey, whey components, and essential amino acids: mechanisms underlying health benefits for active people (review)”. *The Journal of Nutritional Biochemistry* 14.5 (2003), pp. 251–258. DOI: [https://doi.org/10.1016/S0955-2863\(03\)00030-5](https://doi.org/10.1016/S0955-2863(03)00030-5).
- [23] J. de Wit. “Nutritional and Functional Characteristics of Whey Proteins in Food Products”. *Journal of Dairy Science* 81.3 (1998), pp. 597–608. DOI: 10.3168/jds.S0022-0302(98)75613-9.
- [24] S. Damodaran. “Amino Acids, peptides and proteins”. *Fennema’s food chemistry 4th edition*. CRC Press, 2008. Chap. 5, pp. 217–330.
- [25] G. Unterhaslberger, C. Schmitt, C. Sanchez, C. Appolonia-Nouzille, and A. Raemy. “Heat denaturation and aggregation of β -lactoglobulin enriched WPI in the presence of arginine HCl, NaCl and guanidinium”. *Food Hydrocolloids* 20 (2006), pp. 1006–1019. DOI: 10.1016/j.foodhyd.2005.10.017.
- [26] Mounsey, J and OKennedy, B. “Conditions limiting the influence of thiol-disulphide interchange reactions on the heat-induced aggregation kinetics of β -lactoglobulin”. *International Dairy Journal* 17.9 (2007), pp. 1034–1042. DOI: <https://doi.org/10.1016/j.idairyj.2006.12.008>.
- [27] C. Holt, P.A. Timmins, N. Errington, and J. Leaver. “A core-shell model of calcium phosphate nanoclusters stabilized by β -casein phosphopeptides, derived from sedimentation equilibrium and small-angle X-ray and neutron-scattering measurements”. *European Journal of Biochemistry* 252.1 (1998), pp. 73–78. DOI: 10.1046/j.1432-1327.1998.2520073.x.

- [28] C. Holt. “Structure and Stability of Bovine Casein Micelles”. *Advances in Protein Chemistry* 43 (Jan. 1992), pp. 63–151. DOI: 10.1016/S0065-3233(08)60554-9.
- [29] L. Donato and F. Guyomarc’h. “Formation and properties of the whey protein/ κ -casein complexes in heated skim milk A review”. *Dairy Science and Technology* 89.1 (2009), pp. 3–29. DOI: 10.1051/dst:2008033.
- [30] A.J. Vasbinder and C.G. De Kruif. “Casein–whey protein interactions in heated milk: the influence of pH”. *International dairy journal* 13.8 (2003), pp. 669–677.
- [31] S.G. Anema. “Effect of Milk Concentration on Heat-Induced, pH-Dependent Dissociation of Casein from Micelles in Reconstituted Skim Milk at Temperatures between 20 and 120 °C”. *Journal of Agricultural and Food Chemistry* 46.6 (1998), pp. 2299–2305. DOI: 10.1021/jf970909+.
- [32] S.G. Anema. “Role of κ -casein in the association of denatured whey proteins with casein micelles in heated reconstituted skim milk”. *Journal of Agricultural and Food Chemistry* 55.9 (2007), pp. 3635–3642. DOI: 10.1021/jf062734m.
- [33] J. Visser and T.J. Jeurink. “Fouling of heat exchangers in the dairy industry”. *Experimental Thermal and Fluid Science* 14.4 (1997), pp. 407–424.
- [34] H. Burton. “Reviews of the progress of dairy science”. *Journal of Dairy Research* 33 (1966), pp. 225–243.
- [35] M.C. Georgiadis and S. Macchietto. “Dynamic modelling and simulation of plate heat exchangers under milk fouling”. *Chemical Engineering Science* 55.9 (2000), pp. 1605–1619.
- [36] S. Guan and S. Macchietto. “A Novel Dynamic Model of Plate Heat Exchangers Subject to Fouling”. 43 (2018), pp. 1679–1684.
- [37] C. Hagsten, A. Altskär, S. Gustafsson, *et al.* “Composition and structure of high temperature dairy fouling”. *Food Structure* 7 (2016), pp. 13–20.

Chapter 2

An objective classification of condensation regimes in Direct Contact Condensation

Abstract

Intensified heat treatment, using Direct Contact Condensation (DCC), is applied in the production of dairy products to ensure a high level of food safety. The key challenge with a DCC are the protein reactions and fouling that limit operational efficiency and sustainability. Using a condensation regime map can improve operational decision making. Pilot plant scale experiments were conducted for a wide range of steam mass fluxes and inlet temperatures at high and low channel pressures. High-Speed images were recorded and analysed to obtain penetration lengths and plume area. The experimental data and image analysis supplemented with temperature and pressure measurement, were processed with Machine Learning (ML) models to develop a data driven model to predict the regime maps. The Linear Discriminant Analysis (LDA) was found to be the most suitable model. From the machine learning models it was also found that the best parameters to make a condensation regime map are the steam pressure, channel pressure, subcooling temperature, water Prandtl number and the relative velocity ratio between gas and liquid. The condensation outcomes were presented with various two-dimensional regime maps. New regime maps are proposed using the Prandtl number and velocity ratio as dimensionless parameters.

List of symbols

Symbol	Description	Units
c_p	Specific heat capacity	J/kgK
μ	Dynamic viscosity	$Pa\cdot s$
k	Thermal conductivity	W/mK
v_i	Velocity of phase "i"	m/s
T_{sat}	Saturation temperature	K
T_i	Temperature of phase "i"	K
h_i	Enthalpy of phase "i"	J/kg
d_{32}	Gas bubble diameter	m
a_{if}	Interface area bubble-liquid	m^{-1}
$m_{g \rightarrow l}$	Condensation volumetric rate	kg/m^3s
α_i	Heat transfer coefficient phase "i"	W/m^2K
ε_g	Volume fraction of gas	–

This chapter is based on S.S. Safavi Nic, T.H.P. van Veen, K.A. Buist, R.E.M. Verdurmen, and J.A.M. Kuipers. An objective classification of condensation regimes in Direct Contact Condensation. *AIChE Journal* (Apr. 2023)[38].

2.1 Introduction

It is therefore important that the flow patterns in the injector are such that the residence times are as short as possible and that hot condensate mixes rapidly with the cold milk. Mapping the behavior of steam condensation into a condensation regime map can improve operational decision making.

Table 2.1: Description of the distinguished condensation regimes [39–41].

Chugging (C)	Steam-water interface fluctuates around the nozzle exit and moves in and out of the nozzle
Bubbling (B)	Bubble formation around the nozzle exit, cyclic growth, detachment and collapse
Jetting (J)	Steam velocity was (super)sonic and the steam-water interface was stable and smooth

A regime map provides an overview of the type of condensation behaviour that can be observed under certain operational conditions. The most relevant operational regimes can be found in Table 3.2. In addition to the mentioned regimes some researchers also identified several. However, for many of these subcategories it is not clear at what exact conditions these experiments were performed [42, 43]. This was also reported by Heinze et al[44] when using the experimental data from Xu et al [45] to validate the model in their work. An overview of most relevant research is provided in Table 5.1. Parameters such as steam pressure and channel pressure are not reported precisely, usually only as an indicative range or not reported [39, 40, 46]. These parameters are important because they influence the physical properties of steam and the saturation temperature of water. Clerx et al [47] reported the exact experimental conditions per run however the results were not used to generate reliable regime maps.

Table 2.2: Overview of various research on steam injection into stagnant pool and flowing water bodies. Experimental data is listed however not all values are reported (NR).

Injector type	Orientation	Water temperature [°C]	Steam mass flux [kgm ⁻² s ⁻¹]	Channel pressure [bar]	Steam pressure [bar]	Author
Stagnant pool	Vertical	60-90	0-50	atm	NR	[40, 46]
Co-Current	Vertical	10-90	0-1500	NR	NR	[39]
Cross flow	Vertical	25-74	40-135	2.44-3.16	2.2-3.5	[47]
Co-current	Vertical	20-70	110-500	1.5	2-8	[42, 45]
Co-current	Horizontal	20-60	200-650	1-5	1-5	[43]

The goal of the present work is to investigate the critical parameters that determine the boundaries of condensation regimes of direct steam injection in industrial applications. A data driven model was used to predict the regime boundaries to elucidate the role of critical parameters. This study is divided into three parts; (1) producing a condensation regime map using a pilot-plant scale setup with industrial conditions; (2) determining which parameters are most influential in controlling the condensation regime and finally (3) developing a data driven model to predict the regime map.

2.2 Materials and methods

2.2.1 Experimental set-up

The experimental setup is schematically represented in Figure 2.1. As can be seen from the diagram, the setup has a fully closed water cycle and a steam generation input. Water is stored in a 339 L cylindrical stainless steel tank (1) and is fed to the rectangular injection channel using a Optidrive E3 IP66/NEMA 4X pump with a capacity of 275-890 L/h. Steam is generated (3) using a CERTUSS E6-72M electrical steam generator with a capacity of 0-48 kg/h at 9 bar. A pressure reduce valve (4) is used to control the pressure and mass flow rate towards the injector. The latter is measured using a Proline Promass 80F Coriolis mass flow sensor. An ADCA FLT16 float and thermostatic steam trap (5) is introduced before injection into the channel to remove remaining condensate and inert gases to ensure a steady flow of saturated steam into the channel. The channel pressure is regulated using a back pressure control valve (6). The injector channel is illuminated by two LED lights (10) and are placed on both sides of the camera. The condensation phenomenon is recorded using a FASTCAM SA-Z 2100K-M-128GB high-speed camera at 20kHz(11) with a Sigma 105mm F/2.8 EX DG OS HSM Macro lens. The heated water is stored in a second 339 L stainless steel water buffer tank (7) before it is taken on by the heat-exchanger (9) to cool and returned to the feed tank. An overview of the experimental conditions is reported in Table 2.3.

The steam injector is a rectangular channel with two injection points, as shown schematically in figure 2.2. The first segment of the injector is 415 mm long and is required for flow stabilization. The length was taken as 40 times the hydraulic diameter. The injection points are placed after the flow development segment and both have a diameter of 4 mm. The steam can be directed either through the top, bottom or both injectors using valves. The mixing segment is optically accessible using Sapphire glass, placed on the front and backside of the injector. The injector has in total 8 sensor slots placed on the top side (A) and 8 on the bottom (B). The first sensor after the injection point is placed 6.5 mm after the injection point. The distance to the other sensor slots is 19 mm with exception of a 27 mm distance between sensor slot 6, 7 & 8.

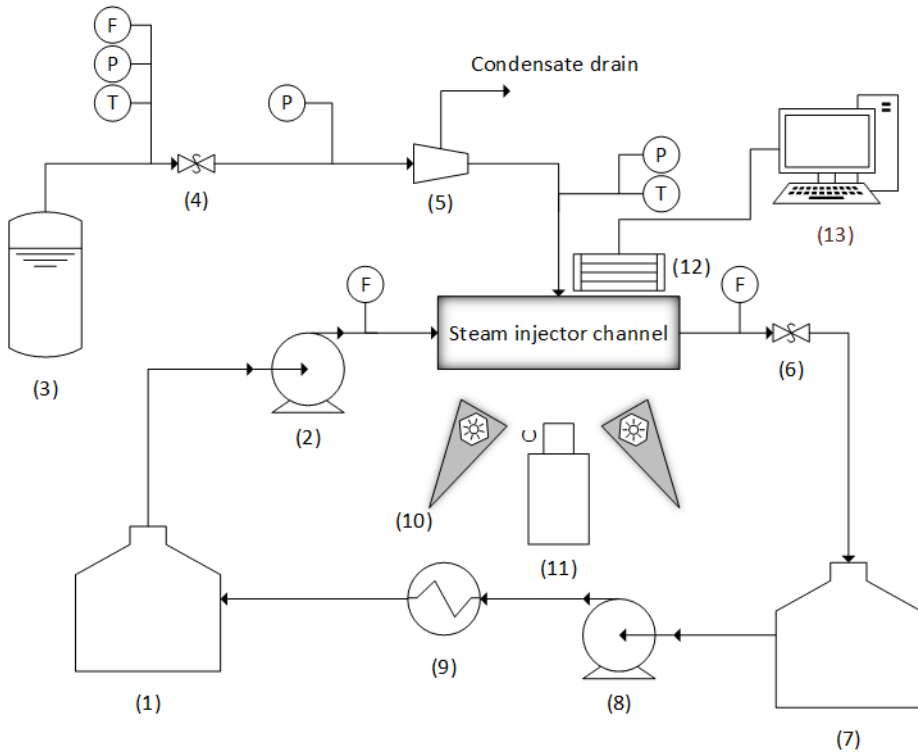


Figure 2.1: Schematic representation of the experimental rig. (1) Water tank, (2) Pump, (3) Steam generator, (4) Pressure reduce valve, (5) Condensate drain, (6) Back pressure valve, (7) Hot water tank, (8) Pump, (9) Plate heat exchanger, (10) LED front lighting (11) High speed camera, (12) data logger, (13) Computer

The sensor slots are suitable to place temperature and pressure sensors. Temperature is measured with type 12 mineral insulated T-type thermocouples. Pressure is measured with MAKS-6(X) ultraminiature high temperature pressure transducers from Kulite. All sensor data is collected using a NI cDAQ-9185 data acquisition system (12) (with modules NI-9220, NI 9401 and NI 9213), which is transferred to a computer (13) and logged via LabVIEW-software. The recordings of the high-speed camera are processed via Photron FASTCAM Viewer 4.

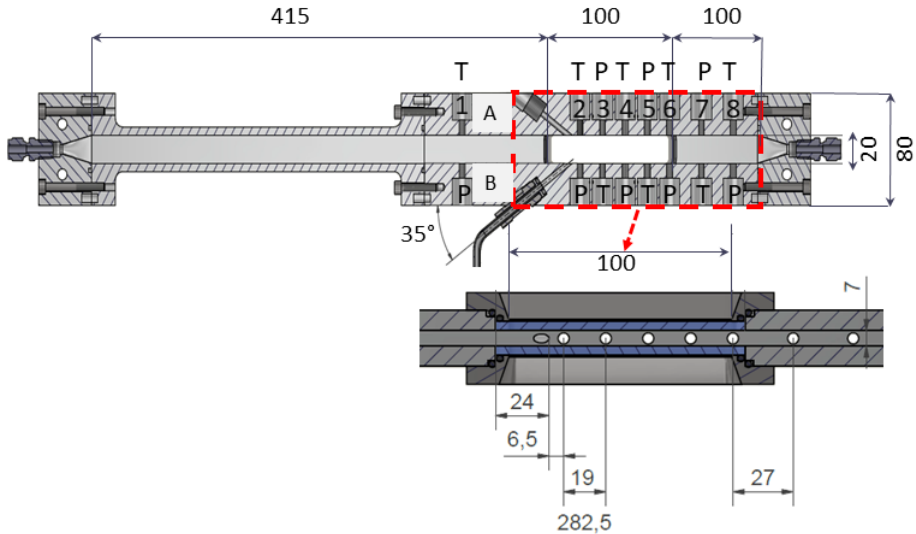


Figure 2.2: Schematic representation of the steam injector. $L=615$ mm, $H=20$ mm, $W=7$ mm. The channel has a 100 mm long sapphire glass window placed front and back for optical access of the injector

Table 2.3: Overview of the experimental conditions.

Variable	Value	Accuracy	Unit
Liquid inlet temperature	15-85	0.4%	$^{\circ}\text{C}$
Channel pressure	1.2-4.2	1.1%	bar
Steam pressure	1.2-8.2	0.5%	bar
Steam mass flux	10-1100	0.8%	$\text{kgm}^{-2}\text{s}^{-1}$
Subcooling	130-280	0.4%	$^{\circ}\text{C}$
Water Reynolds number	7300-12500		(-)

2.2.2 Image analysis

Objective classification methods for condensation regime determination are necessary to study the subtle transitions between regimes that cannot be determined visually and are subjected to operator biases. To this end, automated processing of the recording is preferred to analyze and compute relevant condensation characteristics such as the steam plume length. In this work, the Image Processing Toolbox in MATLAB R2020b is used to analyze the images and determine properties such as the plume length, area and oscillation characteristics.

The MATLAB scripts loads the original image (figure 2.3a) and proceeds, in the case of jetting and bubbling with binarization (figure 2.3b) of this image, depending on a manually fixed threshold value that is applied to the complete image. The use of a manually fixed

threshold can be sensitive to a bias affecting the objective regime classification. For this reason in subsection 2.2.2 the sensitivity of this parameter is assessed. As a result the image is processed such that only the steam bodies of interest remain. This processing involves two steps; filling and clearing. First, holes in the image are filled. After the filling step, small objects that are not of interest are removed resulting in Figure 2.3c. When these steps have been performed, the resulting binary image shows only the steam bodies of interest. These steam bodies are then labeled to allow for individual analysis. Individually connected areas where a steam body is present are now labeled with ascending integers such that the first body is labeled with 1's in the matrix. Finally the properties of these regions, such as area, centroid and extrema of the steam body are determined. An example can be found in Figure 2.3d.

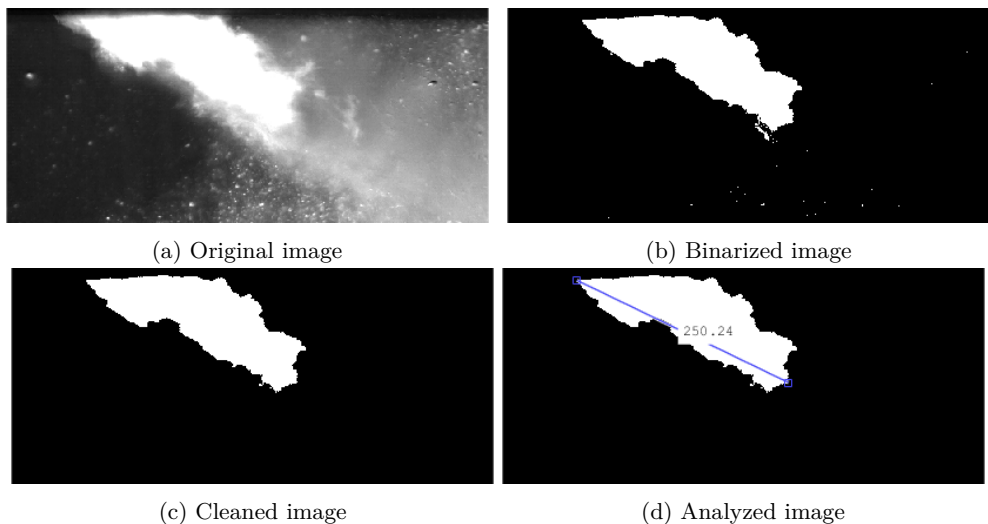


Figure 2.3: Steps of image pre-processing for bubbling and jetting regimes.

For the chugging regime, some additional processing steps are required before the binarization of the image. Due to weak internal reflection of light (see Figure 2.4a), some steam pockets appear darker than the background. Therefore, these steam pockets are rejected in the binarization due to the global thresholding. The visibility of steam bodies can be improved by using filters and contrasting to enhance edges of the pockets, and subsequently filling these pockets. Accordingly, a new step is added to the existing procedure: texture analysis, which is the characterization of various regions by texture in an image. This is done by quantifying texture qualities (e.g. rough/smooth) as a function of spatial variation in pixel intensities [48]. The images are processed using a local standard deviation filtering which returns an image that has equal dimensions as its original, but each pixel entry is now the result of the standard deviation of a defined neighborhood, 3-by-3 in this work. On edges in the original image, the local standard deviation is high due to high local variation in pixel intensity. An example is provided by Figure 2.4b. After rescaling and adjusting the image, the pixels on the edges have now a high intensity, allowing the edge to pass the binarization process as shown by Figure 2.4c. The hole filling function is especially helpful in the chugging regime where the absolute pixel intensity of the re-

gions cells are relatively low, but the variation between the bubble and the background is relatively high.

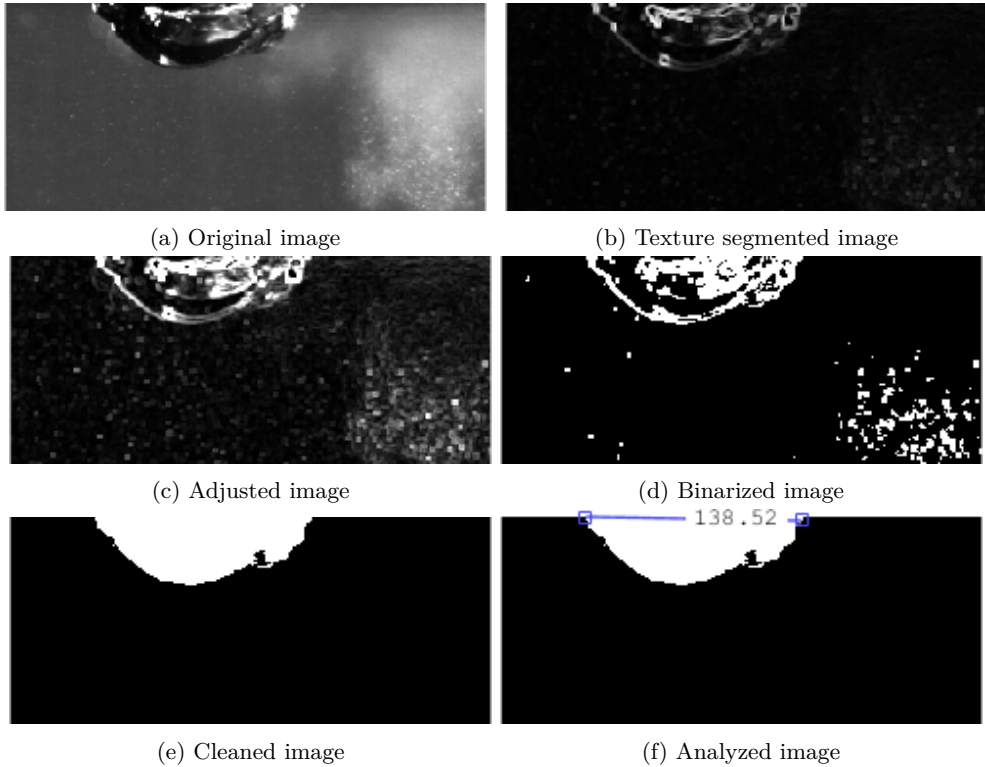


Figure 2.4: Steps of image pre-processing for chugging regime.

Thresholding Verification

In order to apply image binarization it is necessary to determine a threshold value, as described in subsection 2.2.2. This process is susceptible to bias, as employing a low threshold results in loosened binarization where the steam plume characteristics could be artificially increased. For each experiment the appropriate threshold is selected enabling the correct determination of the plume characteristics.

Figure 2.5 shows a sensitivity plot for the penetration length for various thresholds. Applying a low value (i.e. a wide threshold) captures more grey pixels and increases the binarization area. A high value (i.e. a narrow threshold) results in a lower penetration length. The penetration length decreases linearly by increasing the threshold. After a specific threshold, all pixels are converted to black and no steam plume can be detected, which is indicated by the abrupt ending of the graph. The standard deviation however flattens out and reaches a minimum. This implies that the overall variance of the measurement is minimized at the minimum of the graph. At this threshold value, the binarization

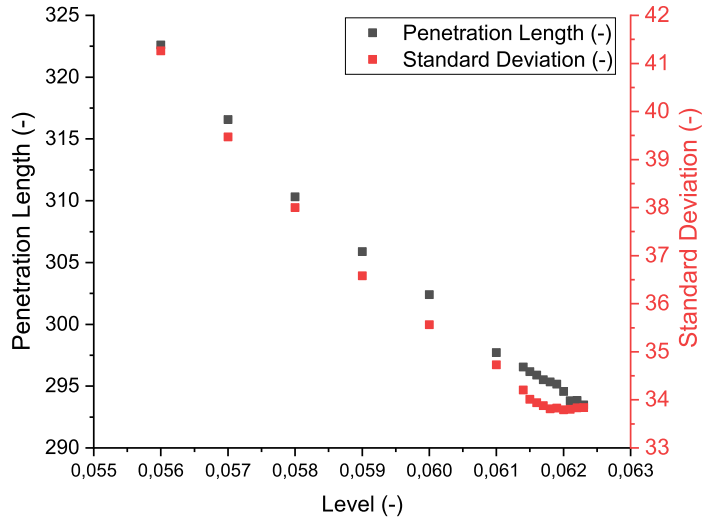


Figure 2.5: Sensitivity of the penetration length and standard deviation for a range of thresholds levels from wide to narrow.

is expected to resemble the original image closest and should therefore be selected. This method is employed for each digital image analysis to ensure consistency among the experiments and obtain the best possible accuracy in determining the penetration length.

2.3 Machine learning models

The goal of this work is to investigate the critical parameters that determine the boundaries of the condensation regimes. In our study 299 experiments were conducted with 79 different variables being logged whereas 2000 frames were recorded and saved per experiment. This data can be used to find correlations between various system parameters and the condensation process. Machine learning (ML) is implemented to facilitate data processing and utilize algorithms to build a model that can classify samples based on the input data.

The machine learning methods used in this work focus on statistical classification and used to assign a specific class (regime) to experimental samples using existing data on explanatory variables termed features. In this work, three classification models will be implemented and compared; the k -NN algorithm preceded by principal component analysis (PCA), linear discriminant analysis (LDA), and quadratic discriminant analysis (QDA).

The general implementation structure is visualized in Figure 2.6. The first step in this approach is data pre-processing (1). In this step a feature selection method is applied to identify the situation where two or more parameters are highly linearly related, (multi)collinearity.

Additionally, in this step a separation is made in which data is divided into a training and testing set using a 80/20 ratio.

The next step is to reduce the dimensionality (2) of the data set. There are several benefits of this step. Firstly, dimensionality reduction vastly reduces computation time because computation in high-dimensional data is costly [49]. Secondly it can remove random noise from the data and finally it removes unwanted degrees of freedom and thereby reduces the impact of properties that do not hold much variance and therefore reduce predictive power of the algorithm [50, 51]. Feature selection as dimension reduction is applied on the data set for all models.

Additionally, prior to application of the k -NN model, principal component analysis (PCA) is implemented, which is one of the most commonly applied dimension reduction methods in general and for k -NN specifically [52, 53]. PCA is an unsupervised model that applies a statistical procedure that computes linearly uncorrelated variables (principal components) as new features to replace the existing features. The main idea of principal component analysis is to simplify a high-dimensional data set by computing and selecting the two principal components as new variables that retain maximum information from the dimension reduction. The principal components are a linear combination of all features in the data set with weight coefficients termed loadings, and are all orthogonal to each other. The principal components have directions that represent the spread of the data (variance) and have magnitudes that represent how much variance is captured by the principal component. Ideally, all variance is retained by the first two principal components to ensure no information is lost in the dimension reduction to two variables. The discriminants in LDA and QDA are similar in form, but while PCA focuses the principal components to capture maximum variance in the data set, LDA and QDA compute the discriminants to have maximum separability between classes.

After the dimension reduction is applied the ML models can be trained (3). The model performance is analyzed for all three classification models using scores for precision, recall and f1 for each class together with the amount of samples in the testing set of this class.

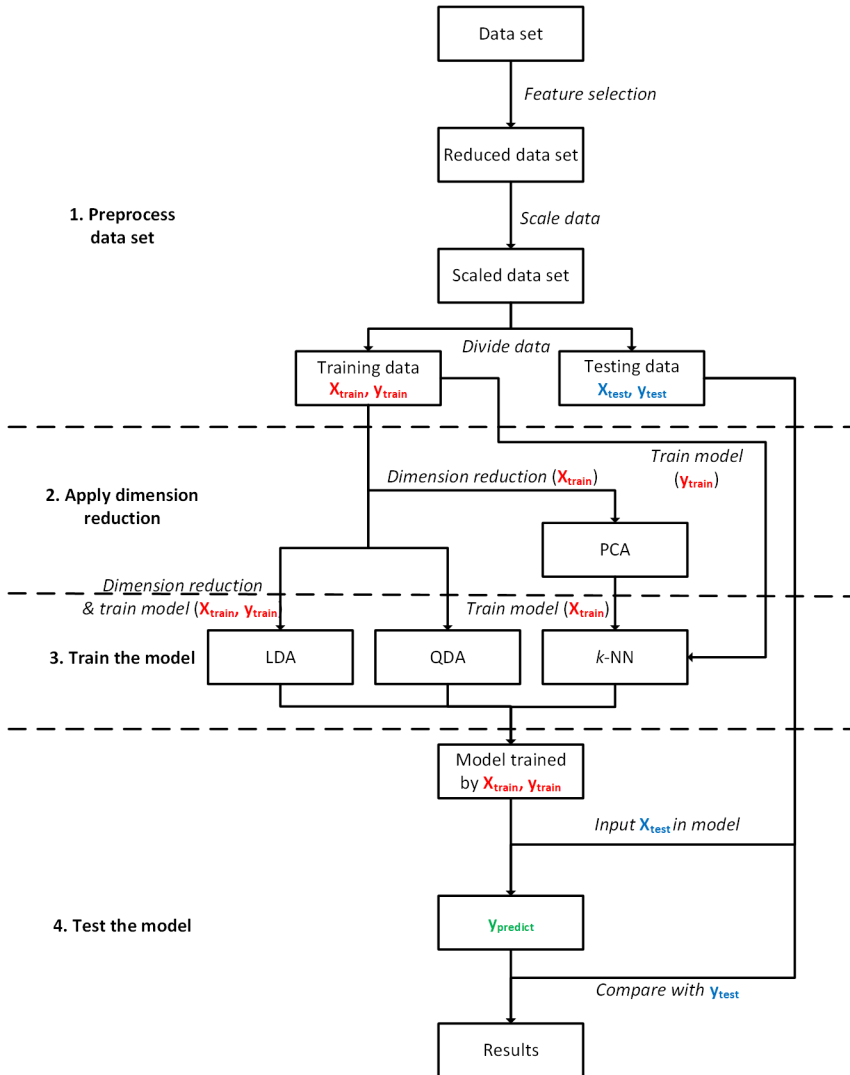


Figure 2.6: Visual flow diagram of the machine learning implementation procedure.

2.4 Results and discussion

2.4.1 Machine learning results

Before the models are used, feature selection was performed by inspection of Pearson and Spearman correlation matrices to reduce multicollinearity and improve predictive power. From the 79 logged variables 26 features were chosen to remain in the data set, which are shown in Table 7.1. In the models, the principal components (PC) and linear discriminants

(LD) are comprised of a linear combination of all these features.

After the feature selection the machine learning models are able to identify the key parameters for determining the condensation regimes. The main features are listed in Table 2.4. Three classification models were implemented and their performance is evaluated in this section. The parameters for k -NN and QDA were not further investigated for visualizing regime maps due to the poor performance of these models as will be explained in the following section. In addition a Buckingham Pi analysis was performed and the outcome of this methodology is also listed in Table 2.4.

Table 2.4: Overview of the identified defining features per origin. These features have received the largest coefficient from the ML models and therefore identified as most important.

Method	Identified features
k -NN with PCA	$\sigma_{out}, P_{G,in}, T_{out}$
LDA	$\mu_{out}, c_{p,out}, k_{out}, P_{G,in}, \Delta T_{subcooling}$
QDA	-
Buckingham-pi	$\frac{v_G}{v_L}$

The first step in evaluating the performance of the k -NN model is choosing the right method and the optimal value for k . There are two main methods applied in this work for classifying a new sample; by majority of neighbors or by also taking their distance into account. Generally, large k 's are less affected by noise and result in smoother class boundaries [54]. Figure 2.7 shows the total accuracy of the model based on the method used and the amount of neighbors selected. As can be observed, the unweighted method yields better accuracy, with an optimum at $k = 10$. Generally, the accuracy is largely unaffected by selecting a different k , as the variation in k only yields an improvement of a few percent for each method. The general trend and variations are very common and in line with existing works in literature [54, 55].

After optimizing the model, the k -NN algorithm preceded by PCA is still a mediocre model for predicting the regimes. Table 2.5 shows the confusion matrix for the model which indicates correct predictions for each class, leading to the accuracy report shown in Table 2.6. In this table the macro average per score is the regular average of each score. The weighted average takes into account the support of each class and averages the value attributed to each score for each class accordingly.

As can be seen in the diagonal of the confusion matrix, only 40 out of 50 testing samples were correctly predicted, resulting in an accuracy of 80.0%. Overall, the accuracy of predicting the bubbling regime is good, as 28 of 29 samples are correctly classified as shown with the recall score of 0.97.

While the bubbling regime can be predicted well with this model, the chugging and jetting samples, however, are often mislabeled, mostly as bubbling. One explanation for this specific mislabeling could be the slightly unbalanced training set, as half of the samples belong to the bubbling regime. This may lead to a bias towards the bubbling regime. For the three classification models, this bias is especially problematic for the k -NN model, as it

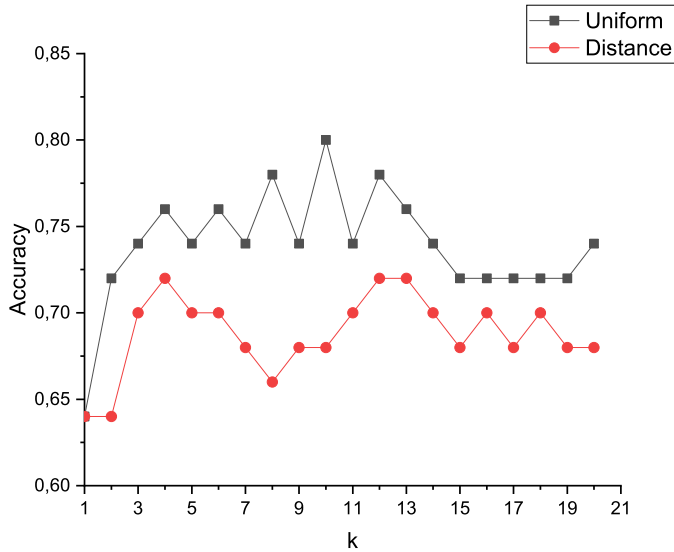


Figure 2.7: Accuracy of the k -NN model by method and amount of neighbors.

classifies a new sample based on the majority of votes. When one class is represented more than the others, it will become the majority more quickly. Introducing a more balanced data set could improve the performance of the k -NN model.

An explanation for the general mediocre performance of this model is the relatively low amount of variance captured by the principal components. PC1 accounts for 55.5% for the total variance, while PC2 captures 17.5% of variance. This means that 27% of the information from the variables is lost in the dimension reduction step of PCA.

Table 2.5: Confusion matrix for the k -NN model.

		Predicted		
		Bubbling	Chugging	Jetting
Actual	Bubbling	28	0	1
	Chugging	6	7	0
	Jetting	3	0	5

Table 2.6: Accuracy metrics scores for the k -NN model.

	Precision	Recall	F1-score	Support
Bubbling	0.76	0.97	0.85	29
Chugging	1.00	0.54	0.70	13
Jetting	0.83	0.62	0.71	8
Accuracy			0.80	50
Macro average	0.86	0.71	0.75	50
Weighted average	0.83	0.80	0.79	50

Linear Discriminant Analysis

Linear discriminant analysis performs very well as a classification model for the data set. The confusion matrix and accuracy scores can be observed in Table 2.7 and Table 2.8 respectively. As can be observed in the confusion matrix, only two samples are misclassified, leading to an accuracy of 96%. The jetting regime scores perfectly, as can also be seen in Table 2.8. The lowest score in this table is the recall of the chugging regime with 0.85, which is still a relatively good score. This implies that linear discriminant analysis is very well suited as a classification model. An explanation for the improved performance compared to the k -NN model can be found in the dimensionality reduction step. While PCA aims to achieve maximum variance between its axes, LDA tries to maximize separation between the classes. The explained variance of the linear discriminants can also be compared to the principal components. LD1 contains approximately 73.1% of total variance and LD2 captures 26.9%, compared to 55.5% and 17.5% of PC1 and PC2 respectively. Extremely little information is lost in the dimension reduction step of LDA compared to PCA, which contributes to the high accuracy of the LDA model. A visual of the high accuracy of the LDA model can be observed in Figure 2.8.

Table 2.7: Confusion matrix for the LDA model.

		Predicted		
		Bubbling	Chugging	Jetting
Actual	Bubbling	29	0	0
	Chugging	2	11	0
	Jetting	0	0	8

Table 2.8: Accuracy metrics scores for the LDA model.

	Precision	Recall	F1-score	Support
Bubbling	0.94	1.00	0.97	29
Chugging	1.00	0.85	0.92	13
Jetting	1.00	1.00	1.00	8
Accuracy			0.96	50
Macro average	0.98	0.95	0.96	50
Weighted average	0.96	0.96	0.96	50

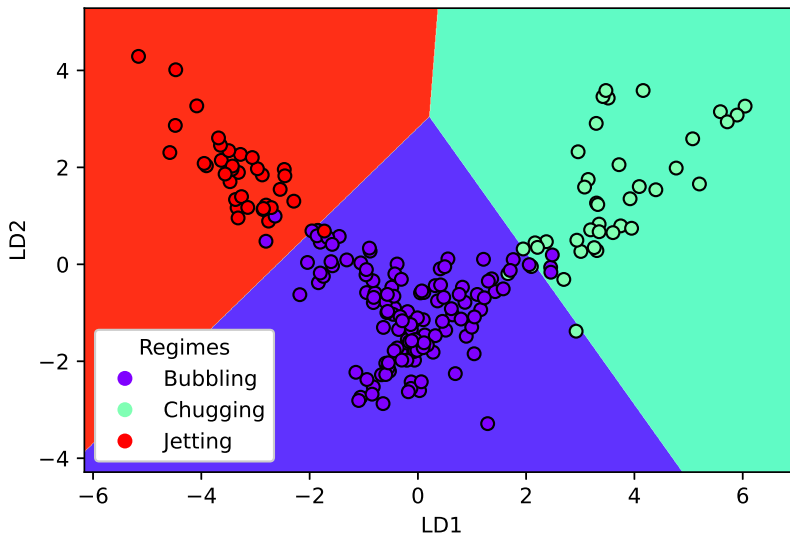


Figure 2.8: Linear discriminant analysis decision boundaries.

Quadratic Discriminant Analysis

The last model, quadratic discriminant analysis, was applied to the data set and yields average results. Table 2.9 and Table 2.10 respectively show the confusion matrix and the accuracy scores for the QDA model. As shown in the diagonal of the confusion matrix, the model is fairly good in predicting the classes of the testing set with 86% accuracy. The precision for predicting the bubbling regime is the lowest of the three with 82% (28 out of 34 correct predictions). This result is similar to LDA, but quite different from the relatively high precision score for bubbling in the k -NN model, which was reasonably good at predicting the bubbling regime compared to the others. Another surprising detail can be found in the recall of the chugging regime with a score of 0.69. This means that the model does not perform well in predicting the chugging regime.

QDA performs worse than LDA, which can be explained in several ways. One of the main differences between LDA and QDA is the way they treat covariance matrices. LDA assumes that all classes share a common covariance matrix due to the assumption of a

Table 2.9: Confusion matrix for the QDA model.

		Predicted		
		Bubbling	Chugging	Jetting
Actual	Bubbling	28	1	0
	Chugging	4	9	0
	Jetting	2	0	6

Table 2.10: Accuracy metrics scores for the QDA model.

	Precision	Recall	F1-score	Support
Bubbling	0.82	0.97	0.89	29
Chugging	0.90	0.69	0.78	13
Jetting	1.00	0.75	0.86	8
Accuracy			0.86	50
Macro average	0.91	0.80	0.84	50
Weighted average	0.87	0.86	0.86	50

multivariate Gaussian distribution [56]. QDA however assumes that each class has its own covariance matrix. This difference between the methods leads to a bias-variance trade-off. For QDA, a separate covariance matrix is calculated for every class, tripling the amount of parameter estimations in this work. The LDA model becomes linear in x (amount of measurements) by assuming every class shares the same covariance matrix. Therefore, LDA becomes a less flexible classifier and thus has considerably lower variance, which can lead to improved prediction performance [57]. The trade-off is that if the assumption of a shared covariance matrix is off, the LDA model may suffer from high bias as it is less flexible. LDA is typically better than QDA with small data sets and so reducing variance is critical [58].

2.4.2 Regime maps

The key outputs of the machine learning models, next to the predictive power, are the key process variables that influence these regimes. The added value of this approach is that it allows us to redefine the regime maps using objectively chosen process variables. The variables of interest are the steam pressure (P_s), subcooling ($T_{sc} = T_s - T_w$), the water Prandtl number (Equation 3.12) at the exit of the injector and the dimensionless velocity ratio between gas and liquid (Equation 2.2).

$$\text{Pr} = \frac{c_p \mu}{k} = \frac{\text{momentum diffusivity}}{\text{thermal diffusivity}} \quad (2.1)$$

$$\Pi_v = \frac{v_G}{v_L} \quad (2.2)$$

In this research it has been chosen to work as much as possible with dimensionless numbers to depict the regime maps as it makes it less dependent on our specific experimental set-up and operating conditions. The proposed regime map is a combination of the Prandtl number and the velocity ratio of gas and liquid. The Prandtl number was identified by the LDA analysis as a critical parameter for defining regimes. Figure 2.9 shows the regime map for two different back pressure settings and shows good separation between the regimes. In Figure 2.9a all three regimes can be discovered. For higher water inlet temperatures (and as a consequence, lower Prandtl numbers) the regime switched again from jetting to bubbling. When the back pressure was increased the jetting regime was no longer observed as shown in Figure 2.9b. At higher back pressure, the steam pressure also increased. There are then several combined physical effects that occur. Firstly at elevated channel pressure, the saturation temperature is increased. At the same time a higher steam pressure is required, resulting in a higher degree of subcooling. These effects, combined in Equation 2.3, increase the rate of condensation and as a consequence the steam cavity penetrates less into the channel. Finally, due to the elevated pressure the gas bubble size distribution decreases, resulting in a higher interfacial area as shown in Equation 2.4.

$$m_{g \rightarrow l} = a_{if} \frac{\alpha_l (T_{sat} - T_l) + \alpha_g (T_{sat} - T_g)}{h_{g,if} - h_{l,if}} \quad (2.3)$$

$$a_{if} = \frac{6\varepsilon_d}{d_{32}} \quad (2.4)$$

The influence of the channel pressure is also found in the interphase heat transfer coefficient (α_l). This quantity can be estimated using a Nusselt correlation as given by Equations 3.10 and 3.11. The impact of the channel pressure is found in the Reynolds number (Equation 4.10) of the dispersed gas phase. The Reynolds number is not only influenced by the gas bubble size (d_{32}) but also by the relative vapour velocity which is influenced by the density of steam.

$$\text{Nu}_l = \frac{\alpha_l \cdot d_b}{k} \quad (2.5)$$

$$\text{Nu}_l = 2 + 0.4 \text{Re}_g^{1/2} \text{Pr}_l^{1/3} \quad (2.6)$$

$$\text{Re}_g = \frac{\rho_l |v_g - v_l| d_{32}}{\mu_l} \quad (2.7)$$

The main drawback of working with the Prandtl number and dimensionless velocity is that these parameters are less intuitive for the use of regime maps. Another set of parameters identified by the machine learning are the steam pressure and degree of subcooling, Figure 2.10. The benefit of this regime map is that the variables used are intuitive for operational decision making as well as that it shows clear distinction between regimes.

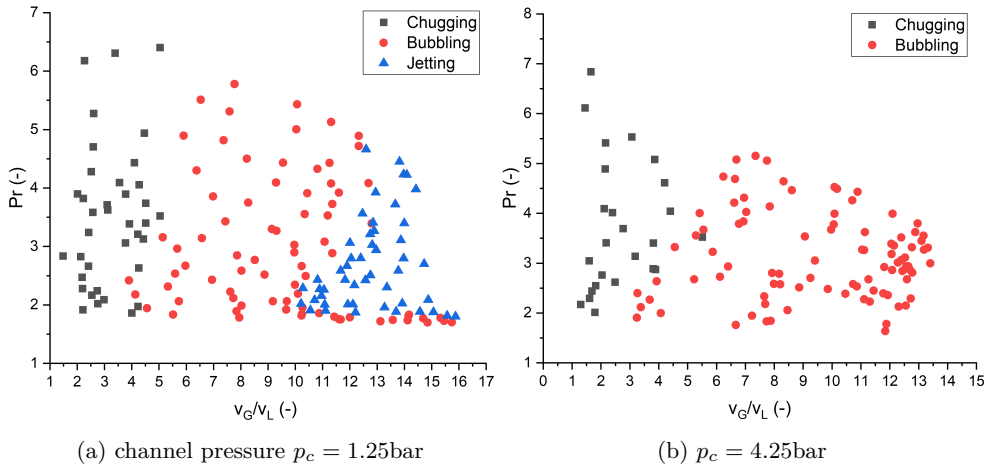


Figure 2.9: Regime map based on the Prandtl number and dimensionless velocity. $Re = 12500$ at different back pressures.

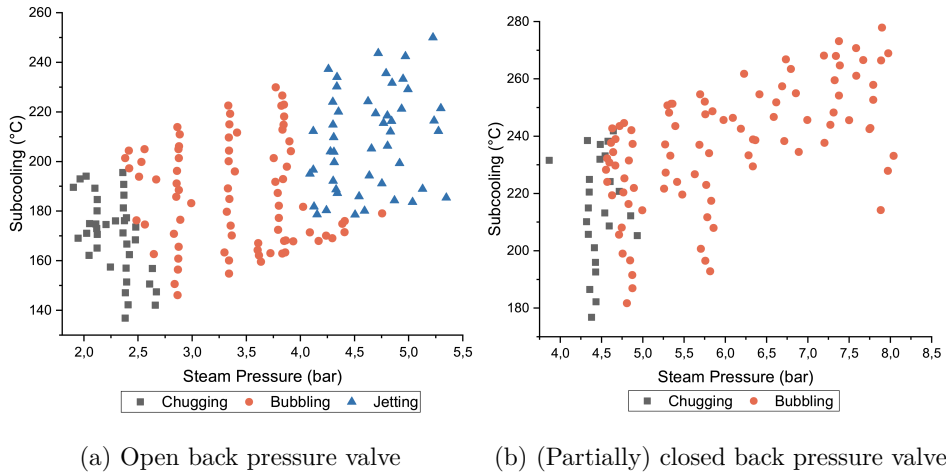


Figure 2.10: Regime map based on the steam pressure and degree of subcooling. $Re = 12500$ at different back pressures.

2.4.3 Impact of elevated liquid temperature

As discussed in the previous section, when the Prandtl number is decreased the jetting regime is no longer observed. This is a direct consequence of increasing the liquid inlet temperature. When the liquid temperature is increased, the driving force for condensation decreases. This allows the steam cavity to penetrate deeper into the channel and occupy a larger area, as shown in Figure 2.11. Both the penetration length (l_s) and the area (A_s) are normalized by dividing the values by the injector diameter (d_N) and its area respectively (A_N). As the steam cavity penetrates deeper and the surface area increases, more condensation can occur, in turn reducing the steam cavity size. This effect yields the bubbling regime instead of the jetting regime and is consistent with observations in literature [59].

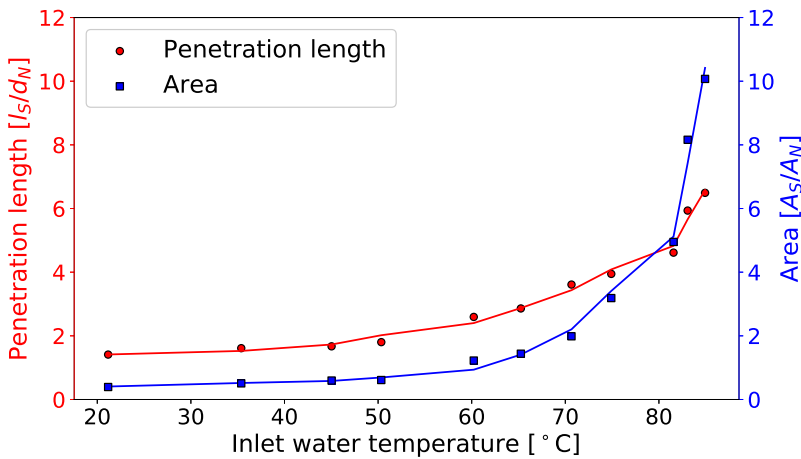


Figure 2.11: Penetration length and area as a function of liquid inlet temperature at a steam mass flux of $315 \text{ kg m}^{-2} \text{ s}^{-1}$, channel pressure = 1.7 bar, steam pressure = 4.2 bar, $\text{Re} = 12500$.

2.4.4 Impact of second injection point

The images in Figure 2.12 show dual injection experiments for different steam pressures at an inlet temperature of 17°C . For these experiments, the same classification can be applied as established for single point injection. With increasing liquid inlet temperature, this classification leads to problems at high steam mass fluxes. Figure 2.13 shows experiments for the same steam pressures but a liquid inlet temperature of 56°C . The chugging and the bubbling regime do not look very different, but for the jetting regime, the steam cavities have merged into one large steam plume. Once the steam plumes combine, no more jetting can be observed. Although the condensation potential has decreased due to the increased liquid inlet temperature, the area of the steam plumes also increases. The increased size of the steam plume gives more available area for cooling. As a result of this, the condensation potential increases again. This variation in condensation potential

results in an bubbling-like behavior of the steam plume.

Consequently, the bubble and jetting distinction can not be used anymore. Therefore, the same classification as in literature is assigned for this regime; Interfacial Oscillation. When the liquid inlet temperature increases to about 85°C , the temperature inside the channel reaches above 110°C . At this point, the condensation rate has decreased to such an extent that at higher steam mass fluxes, complete condensation within the measurement region is no longer possible. This regime is classified as partly non-condensing. Figure 2.14 shows images for the experiments performed under the same steam pressures as previous experiments. However, now with a liquid inlet temperature of 85°C . These images illustrate that steam cavities overlap even at low steam pressure. Moreover, for the highest steam pressures, almost the whole measurement area is filled with steam, indicating that almost no condensation occurs.

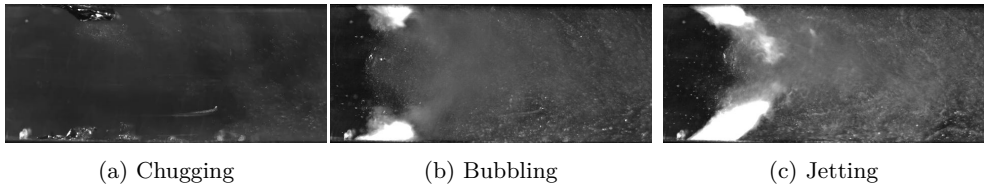


Figure 2.12: Dual steam injection experiments at a liquid inlet temperature of 17°C . Water flows from left to right.

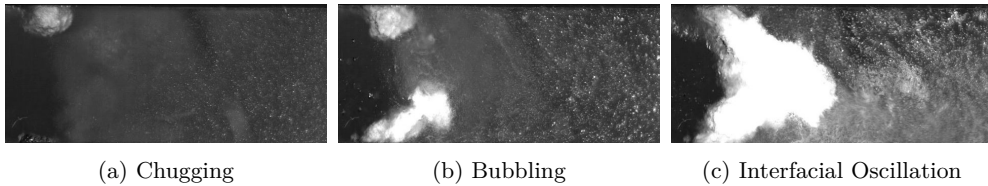


Figure 2.13: Dual steam injection experiments at a liquid inlet temperature of 56°C .

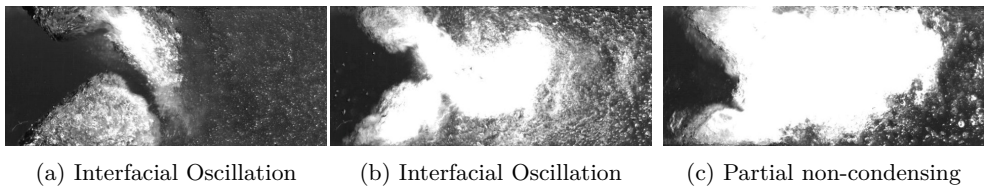


Figure 2.14: Dual steam injection experiments at a liquid inlet temperature of 85°C .

Figure 2.15 shows the regime map for two different back pressure settings and displays a reasonable separation between the regimes. For the experiments performed at low channel pressure it was found that at the lowest Prandtl values and a high gas velocity that the system switched from interfacial oscillation to non-condensing. When the back pressure was increased to 4.25 bar only the chugging and bubbling regime was observable. It can

be concluded that, even though there is a strong relationship between the two parameters, that it is a challenge to differentiate between various regimes.

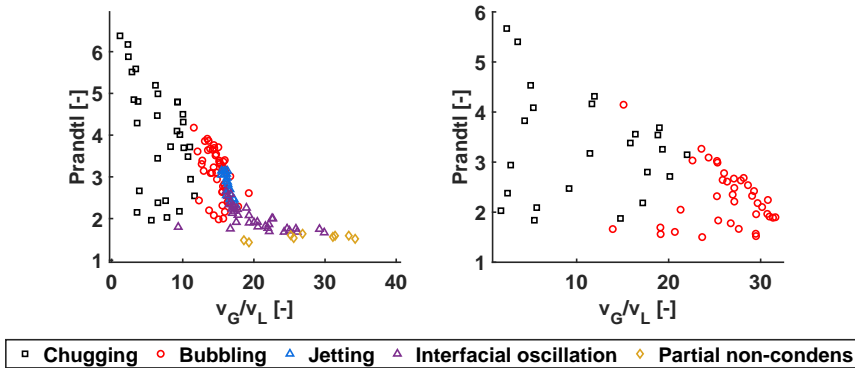


Figure 2.15: Regime map for dual steam injection, showing the Prandtl number for the water outlet versus the ratio of gas and liquid velocity at $Re=12500$. Left for a low channel pressure (1.25 bar) and on the right for a high channel pressure (4.25 bar).

The degree of subcooling ($T_S - T_W$) and steam pressure have also been identified (subsection 2.4.2) as important process parameters for regime classification. The benefit of these parameters is that they are easily controlled and more intuitive than the Prandtl number and velocity ratio. The results are shown in Figure 2.16, it can be observed that the differentiation between regimes is more distinct in comparison with the regime classification shown in Figure 2.15, especially for the transition from jetting to interfacial oscillation.

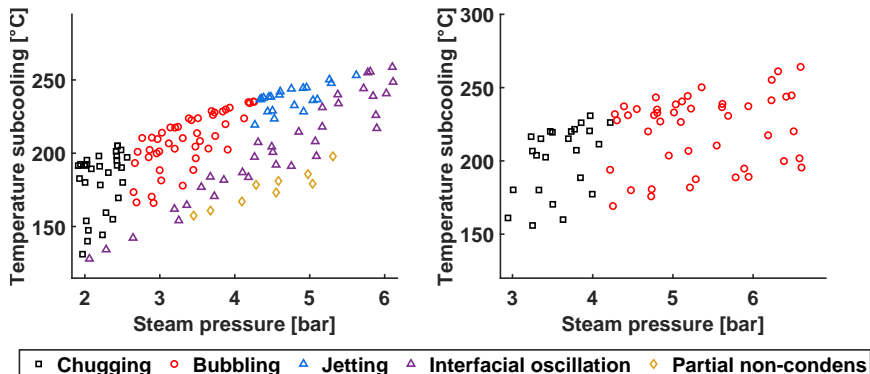


Figure 2.16: Regime map showing the degree of subcooling versus the steam pressure $Re=12500$ for dual steam injection. Left for low channel pressure and right for a high channel pressure.

2.5 Conclusion

The objective of this chapter was to experimentally investigate which parameters play a role in the direct steam condensation process. Pilot plant scale experiments were conducted for a wide range of steam mass fluxes and inlet temperatures at high and low channel pressures. The results were processed using an image analysis protocol to obtain relevant steam cavity properties and further processed with machine learning models to provide objective classification and regime prediction possibilities.

The experimental campaign yielded 299 experiments with 79 different logged variables and 2000 frames recorded per experiment that were used to generate the regime maps. This large amount of data has not been observed in previous research. It was also found that it is important to properly note, besides steam pressure, the channel pressure as it has a significant effect on the condensation regime boundaries. The inlet temperature effect on condensation regime is small, but it does have a large effect on the steam cavity penetration length.

Regarding machine learning, the k -NN and QDA classification models perform reasonably well. Moreover, it can be concluded that LDA is the superior classification model with 96% accuracy, being able to both classify regimes in an objective fashion and predict the regime for new samples. A parameter study was performed via the inspection of the linear discriminants, which led to the insight that the outlet Prandtl number is a good predictor for condensation regimes. Besides the Prandtl number, the steam pressure, channel pressure, subcooling, velocity ratio are better variables for regime maps than steam mass flux and inlet temperature respectively. It is recommended to use steam pressure and subcooling as key variables for regime maps and to report the channel pressure.

In addition it was demonstrated that this method is scalable to a dual injection setup leading to the introduction of new regimes. The second jet influences the temperature gradients to such an extent that the two jets show oscillating behaviour, which has been classified as *"Interfacial oscillation"*. When the degree of subcooling decreased the steam cavity occupies most of the visualization area classified as a partial non-condensing regime. Considering that the preferred condensation regime is the jetting regime it can be concluded that at low channel pressure the operational window for achieving jetting is very small. It is recommended to work with a large degree of subcooling at higher steam pressure when operating at a low channel pressure in order to avoid the partial non-condensation region. When the channel pressure was increased to 4 bar, the only regimes observed are the chugging and bubbling regime. This is in line with our previous observations. Under such conditions it is recommended to maintain a 1 bar pressure difference between the steam pressure and channel pressure to avoid the chugging regime.

For future work it is recommended to firstly increase the liquid viscosity to match the profile of high protein dairy products. It can be expected that the viscosity of the liquid influences the regime map via the Prandtl number. It is important to map the regimes using representative viscosity profiles which will be subject to further research.

Data package

The full set of experimental data as well as the scripts to analyse the data are available as an integral data package. The data package can be accessed via this DOI: <https://doi.org/10.4121/21541776.v1>

References

- [38] S.S. Safavi Nic, T.H.P. van Veen, K.A. Buist, R.E.M. Verdurmen, and J.A.M. Kuipers. “An objective classification of condensation regimes in Direct Contact Condensation”. *AIChE Journal* (Apr. 2023). DOI: <https://doi.org/10.1002/aic.18121>.
- [39] A. Petrovic de With, R.K. Calay, and G. de With. “Three-dimensional condensation regime diagram for direct contact condensation of steam injected into water”. *International Journal of Heat and Mass Transfer* 50.9-10 (May 2007), pp. 1762–1770. DOI: 10.1016/J.IJHEATMASSTRANSFER.2006.10.017.
- [40] K.-S. Liang. “Experimental and analytical study of direct contact condensation of steam in water”. PhD thesis. Massachusetts Institute of Technology, 1991.
- [41] Q. Zhao and T. Hibiki. “Review: Condensation regime maps of steam submerged jet condensation”. *Progress in Nuclear Energy* 107 (Aug. 2018), pp. 31–47. DOI: 10.1016/J.PNUCENE.2017.12.014.
- [42] Q. Xu and L. Guo. “Direct contact condensation of steam jet in crossflow of water in a vertical pipe. Experimental investigation on condensation regime diagram and jet penetration length”. *International Journal of Heat and Mass Transfer* 94 (2016), pp. 528–538. DOI: <https://doi.org/10.1016/j.ijheatmasstransfer.2015.02.036>.
- [43] X. Zong, J.P. Liu, X.P. Yang, and J.J. Yan. “Experimental study on the direct contact condensation of steam jet in subcooled water flow in a rectangular mix chamber”. *International Journal of Heat and Mass Transfer* 80 (Jan. 2015), pp. 448–457. DOI: 10.1016/J.IJHEATMASSTRANSFER.2014.09.050.
- [44] D. Heinze, T. Schulenberg, and L. Behnke. “A physically based, one-dimensional three-fluid model for direct contact condensation of steam jets in flowing water”. *International Journal of Heat and Mass Transfer* 106 (2017), pp. 1041–1051. DOI: 10.1016/j.ijheatmasstransfer.2016.10.076.
- [45] Q. Xu, L. Guo, S. Zou, J. Chen, and X. Zhang. “Experimental study on direct contact condensation of stable steam jet in water flow in a vertical pipe”. *International Journal of Heat and Mass Transfer* 66 (Nov. 2013), pp. 808–817. DOI: 10.1016/J.IJHEATMASSTRANSFER.2013.07.083.
- [46] K.S. Liang and P. Griffith. “Experimental and analytical study of direct contact condensation of steam in water”. *Nuclear Engineering and Design* 147.3 (Apr. 1994), pp. 425–435. DOI: 10.1016/0029-5493(94)90225-9.
- [47] N. Clerx. “Experimental study of direct contact condensation of steam in turbulent duct flow”. PhD thesis. Eindhoven University of Technology, 2010. DOI: 10.6100/IR691389.
- [48] C. Karaba, J. Verhoeven, N. RachelMiller, and C.C. Reyes-Aldasoro. “Texture Segmentation: An Objective Comparison between Five Traditional Algorithms and a Deep-Learning U-Net Architecture”. *Applied Sciences* 2019, Vol. 9, Page 3900 9.18 (Sept. 2019), p. 3900. DOI: 10.3390/APP9183900.
- [49] L. Van Der Maaten, E. Postma, and J. Van Den Herik. “Tilburg centre for Creative Computing Dimensionality Reduction: A Comparative Review Dimensionality Reduction: A Comparative Review”. *Tilburg centre for Creative Computing* (2009).

References

- [50] W. Wang and M.Á. Carreira-Perpiñán. “The role of dimensionality reduction in linear classification” (May 2014). DOI: 10.48550/arxiv.1405.6444.
- [51] A.V. Giessen. “Dimension Reduction Methods for Classification”. PhD thesis. Delft University of Technology, 2012.
- [52] C.X. Yin and Q.K. Peng. “A careful assessment of recommendation algorithms related to dimension reduction techniques”. *Knowledge-Based Systems* 27 (Mar. 2012), pp. 407–423. DOI: 10.1016/J.KNOSYS.2011.11.022.
- [53] S. Deegalla and H. Boström. “Classification of Microarrays with kNN: Comparison of Dimensionality Reduction Methods”. *Intelligent Data Engineering and Automated Learning - IDEAL 2007. IDEAL 2007. Lecture Notes in Computer Science*. Ed. by H. Yin, P. Tino, E. Corchado, W. Byrne, and X. Yao. Vol. 4881. Springer, Berlin, Heidelberg, 2007, pp. 800–809. DOI: 10.1007/978-3-540-77226-2_80.
- [54] A. Starzacher and B. Rinner. “Evaluating KNN, LDA and QDA classification for embedded online feature fusion”. *ISSNIP 2008 - Proceedings of the 2008 International Conference on Intelligent Sensors, Sensor Networks and Information Processing* (2008), pp. 85–90. DOI: 10.1109/ISSNIP.2008.4761967.
- [55] S.C. Gupta and N. Goel. “Performance enhancement of diabetes prediction by finding optimum K for KNN classifier with feature selection method”. *Proceedings of the 3rd International Conference on Smart Systems and Inventive Technology, ICSSIT 2020* (Aug. 2020), pp. 980–986. DOI: 10.1109/ICSSIT48917.2020.9214129.
- [56] W.K. Härdle and L. Simar. *Applied multivariate statistical analysis*. 3rd ed. Springer, 2013, pp. 1–516. DOI: 10.1007/978-3-642-17229-8.
- [57] P. Schmidt. *Linear vs. Quadratic Discriminant Analysis Comparison of Algorithms*. 2018.
- [58] G. James, D. Witten, T. Hastie, and R. Tibshirani. *An Introduction to Statistical Learning*. 2nd ed. Springer, 2021.
- [59] H.Y. Kim, Y.Y. Bae, C.H. Song, J.K. Park, and S.M. Choi. “Experimental study on stable steam condensation in a quenching tank”. *International Journal of Energy Research* 25.3 (Mar. 2001), pp. 239–252. DOI: 10.1002/ER.675.

Chapter 3

A transient mechanistic two-fluid model for Direct Contact Condensation

Abstract

Intensified heat treatment, using Direct Contact Condensation (DCC), is applied in the production of dairy products to ensure a high level of food safety. The key challenge with DCC are the protein reactions and fouling that limit operational efficiency and sustainability. The use of validated, transient models to predict temperature, phase fraction and velocity gradients is essential and can improve the operation of DCC. Pilot plant scale experiments were performed for a wide range of steam mass fluxes, inlet water temperatures, water Reynolds number and channel pressures to validate a transient 1D two-fluid model. The model was tested against steady-state experimental data and showed good agreement. In addition the model was tested against transient data in which either the water flow rate was step wise decreased or the pressure was adjusted throughout the experiment. In general the model followed the experimental trend well provided that the flow inside the channel is homogeneous.

List of symbols

Symbol	Description	Units
ε	Volume fraction	–
ρ	Density	kg/m^3
v	Velocity	m/s
a_{if}	Specific interfacial area	$1/m$
ϕ_{MT}''	Condensation mass flux	$kg/m^2 \cdot s$
q	Heat flux	W/m^2
h	Enthalpy	J/kg
a_c	Heat transfer coefficient continuous phase	$W/m^2 \cdot K$
T_{sat}	Saturation temperature	K
T	Temperature	K
$\phi_{V \rightarrow L}''$	Heat flux vapor to liquid	W/m^2
ϕ_{loss}''	Heat loss	W/m^3
Nu_c	Nusselt continuous phase	–
d_b	Bubble diameter	m
k	Thermal conductivity	$W/m \cdot K$
Pr_c	Prandtl continuous phase	–
μ_c	viscosity	$Pa \cdot s$
$F_{c \rightarrow d}^D$	Drag force	$kg \cdot m/s^2$
C_D	Drag Coefficient	–
E_o	Eötvös number	–
$F_{l \rightarrow w}^W$	Wall friction force	$kg \cdot m/s^2$
d_h	Hydraulic diameter	m
C_w	Wall friction coefficient	–
Re	Reynolds number	–
$F_{c \rightarrow d}^{VM}$	Virtual mass force	$kg \cdot m/s^2$
C_{VM}	Virtual mass coefficient	–

This chapter is based on S.S. Safavi Nic, T.E. Kuipers, K.B. Buist, R.E.M. Verdurmen, and J.A.M. Kuipers. A transient mechanistic two-fluid model for Direct Contact Condensation. *Chemical Engineering Science* (2023) [60].

3.1 Introduction

The previous chapters an experimental study was reported to generate regime maps utilizing a machine learning approach to predict the prevailing operating regime, ranging from chugging, bubbling and jetting. However, these regime maps do not predict a priori what the performance and temperature gradients of a DCC process will be.

To predict temperature gradients while using limited experimental data the best option would either be a Computational Fluid Dynamics (CFD) approach or reduced dimensionality models, such as 1D models. An overview of several reported studies on DCC modelling are given in Table 4.1. The benefit of the use of 1D phenomenological models is their low computational costs allowing the model to simulate time scales up to hours. However these models require strong assumptions which limits their applicability to specific flow regimes and operating conditions. CFD models provide the added value that the impact of geometry of the DCC design and nozzle position on the condensation rate and mixing behaviour can be investigated. CFD models are computationally expensive, limiting the time scales that can be covered to a few seconds. These time scales are enough to gather statistics on the hydrodynamic behavior, but unfortunately are not enough to study the formation of protein deposit layers as the time scales involved can approach to several hours [61]. A 1-Dimensional model that is less computationally expensive would be able to address phenomena prevailing at these time scales.

The available 1D models are typically steady-state, covering macroscopic features of the multiphase system. Zhang et al. [62] and Ma et al. [63] both employed a 1D two-fluid model for a steady state situation. In their model the complexity of the steam injector was treated with a compartment approach. Whilst this approach is sufficient for calculating the exhaust temperature and an overall temperature profile it is not suitable to obtain the temperature gradient that is required. Heinze et al. [44] developed a 1D model and numerically solved the governing equations to obtain detailed information of the temperature profile in DCC. Their steady-state model takes into account the dominant physical processes of condensation at the interface of the two-phase jet, droplet condensation and flowing water. Although their model accounts for all the important phenomena, unfortunately detailed experimental validation was not reported.

Table 3.1: Overview of key models for DCC

Authors	Method	Approach	Deliverable
Zhang et al. [62]	1D	Compartmentalized	Predicting pressure drop and temperature change over each compartment
Ma et al. [63]	1D	Compartmentalized	Predicting critical pressure at the nozzle exit
Heinze et al. [44]	1D	Three fluid model	Predicting steam plume length
Gulawani et al. [64]	CFD	RANS	Validating predicted heat transfer coefficient values
Pacenko et al. [65]	CFD	DIM-LES	Development of an improved CFD model for industrial applications
Dahikar et al. [66]	CFD	LES and RANS	Evaluation of predicted velocity against experimentally obtained velocity

The goal of this research is to present a 1D transient two-fluid model to predict the gradients inside a steam injector including the prediction of the exhaust temperature. Our model accounts for an interface at the jet as well as bubble condensation and is validated with experimental data. This study is therefore divided into three parts: (1) description of the experiments (2) model description and (3) model validation using both a steady state and transient 1D model.

3.2 Model description

Our model takes a classical two-fluid approach in which the vapour (V) and liquid (L) phase are modelled separately. The experimental set-up described in chapter 2 can be operated at a liquid Reynolds number in the range of $5646 < Re_L < 15000$. A schematic representation can be found in Figure 3.1. The use of saturated steam allows for the assumption that the condensation mode is heat transfer limited rather than mass transfer limited. The steam properties are derived from the steam thermodynamic table [67]. Steam is injected into the flowing liquid under a 30° angle over a distance of 6.97 mm. In the model steam is added over this length assuming no steam mass or velocity at the boundary condition.

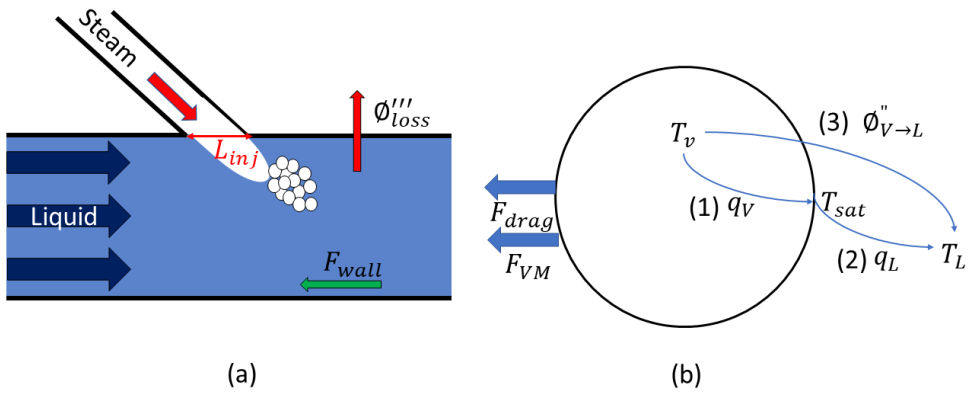


Figure 3.1: (a) Schematic overview of the 1D model illustrating the prevailing phases and their interactions. The water flows from left to right and steam is injected with an angle of 35° . For the bulk liquid the wall friction force (F_{wall}) and heat loss to the environment (ϕ'''_{loss}) are taken into account. (b) Schematic overview of the accounted phenomena for a bubble. For the thermal energy equations (1) the heat flux of vapor to bubble surface (2) heat flux from bubble surface to the liquid phase and (3) the heat flux directly from vapor to liquid are included.

The model is based on the assumption that there are three types of flow interactions based on the phase boundary; a bubbly regime in which gas is dispersed in the liquid, a dispersed droplet regime and an interface regime. The employed thresholds for the regime changes are listed in Table 3.2.

Table 3.2: Threshold values for regimes accounted for in the 1D model.

Bubbly	$0 < \varepsilon < 0.3$
Interface	$0.3 < \varepsilon < 0.7$
Droplet	$0.7 < \varepsilon < 1.0$

3.2.1 Continuity equations

Below, in Equation 5.13, the unsteady continuity equations are given where coefficient ξ_i determines the direction of the mass transfer, ε_i the volume fraction of phase i , ρ_i the density, v_i velocity and a_{if} the specific interfacial area.

$$\frac{\partial \varepsilon_i \rho_i}{\partial t} = -\frac{\partial \varepsilon_i \rho_i v_i}{\partial z} + a_{if} \xi_i \phi_{MT}'' \quad (3.1)$$

The latter quantity (a_{if}) is calculated assuming a spherical shape of the dispersed bubbles. It is assumed that the bubble diameter $d_{32} = 0.1$ mm and is taken uniform throughout the channel.

$$a_{if} = \frac{6\varepsilon_d}{d_{32}} \quad (3.2)$$

$$\xi_i = \begin{cases} +1, & i = \text{Liquid} \\ -1, & i = \text{Vapour} \end{cases} \quad (3.3)$$

The condensation mass flux (ϕ_{MT}'') is represented with a two-resistance model given by Equation 3.4, with the heat flux q_i and the enthalpy (h_i) difference between the phases.

$$\phi_{MT}'' = \frac{\Sigma q_i}{h_V - h_L} \quad (3.4)$$

The heat flux is defined in Equation 3.5 in which the heat transfer coefficient (α_i) of the specific phase is required as well as the temperature difference between the saturation temperature (T_{sat}) and the phase temperature (T_i).

$$q_i = \alpha_i (T_{sat} - T_i) \quad (3.5)$$

3.2.2 Thermal energy equations

For the thermal energy equations the heat flux associated with condensation (ϕ_{MT}''), the interphase heat flux ($\phi_{V \rightarrow L}''$) and the thermal energy loss across the solid wall (ϕ_{loss}''') are required for a complete model.

$$\frac{\partial \varepsilon_i \rho_i h_i}{\partial t} = -\frac{\partial \rho_i v_i \varepsilon_i h_i}{\partial z} + a_{if} \xi_i (\Phi_{MT}'' + \phi_{V \rightarrow L}'') - \phi_{loss}''' \quad (3.6)$$

The energy released from condensation is calculated using the enthalpy of steam. Thermal equilibrium inside bubbles is assumed hence the heat transferred from steam to the liquid phase can be calculated with Equation 3.8. The energy loss is finally calculated using an overall heat transfer coefficient (U_w) and the local driving force ($T_i - T_\infty$)

$$\Phi_{MT}'' = h_V \phi_{MT}'' \quad (3.7)$$

$$\phi_{V \rightarrow L}'' = \alpha_c (T_V - T_L) \quad (3.8)$$

$$\phi'''_{loss} = \frac{\delta_w}{H_c B_c} U_w (T_i - T_\infty) \quad (3.9)$$

Both for the interphase heat flux as well as for the condensation rate it is required to calculate the regime heat transfer coefficient (α_i). For the dispersed phase the heat transfer coefficient is taken as $\alpha_d = 10^4$ [44]. The heat transfer coefficient for the continuous phase can be calculated using a Nusselt relation in Equations 3.10, 3.11, 3.12.

$$Nu_c = \frac{\alpha_c \cdot d_b}{k} \quad (3.10)$$

$$Nu_c = 2 + 0.4 Re_d^{1/2} Pr_c^{1/3} \quad (3.11)$$

$$Pr_c = \frac{\mu_c \cdot c_{p,c}}{k_c} \quad (3.12)$$

3.2.3 Momentum equations

Below the momentum equations (Equation 3.13) are given from which the velocity of phase i can be obtained.

$$\frac{\partial \varepsilon_i \rho_i v_i}{\partial t} = -\frac{\partial \varepsilon_i \rho_i v_i^2}{\partial z} - \varepsilon_i \frac{\partial p}{\partial z} + \Sigma F + v_g a_{if} \xi_i \Phi_{V \rightarrow L}'' \quad (3.13)$$

In Equation 3.13 the total sum of the forces takes into account the interphase drag force ($F_{c \rightarrow d}$, wall friction force ($F_{l \rightarrow wall}$) and the virtual mass force ($F_{c \rightarrow d}^{VM}$). Gravitational forces are neglected due to the horizontal positioning of the channel.

$$\Sigma F = F_{c \rightarrow d}^D - F_{l \rightarrow wall}^W + F_{c \rightarrow d}^{VM} \quad (3.14)$$

Drag force

The drag force acting on the dispersed phase is given by Equation 3.15 and takes into account the relative velocity difference. The drag force on the continuous phase is given by: $F_{d \rightarrow c}^D = -F_{c \rightarrow d}^D$

$$F_{c \rightarrow d}^D = C_D \frac{1}{4} a_{if} \frac{1}{2} \rho_c |v_c - v_d| (v_c - v_d) \quad (3.15)$$

The drag coefficient (C_D) is valid for dilute flow conditions and corrects the drag coefficient for isolated bubbles (C_{D0}) by including the bubble swarm effect ($f(\varepsilon_V)$).

$$C_D = f(\varepsilon_V) C_{D0} \quad (3.16)$$

The correction function ($f(\varepsilon_V)$) is given by the power-law correction in Equation 4.8 [68]. This power law function has a discontinuity at which for volume fractions larger than this threshold the vapour phase is no longer dispersed. The empirical parameter (C_A) is usually in the range $-3 < C_A < -1$. Buffo et al[68] found, after performing a sensitivity analysis,

that this value is $C_A = -1.3$.

$$f(\varepsilon_V) = \begin{cases} (1 - \varepsilon_V)^{C_A} & \varepsilon_V \leq 0.5 \\ 1 & \varepsilon_V > 0.8 \end{cases} \quad (3.17)$$

The single bubble drag coefficient (C_{D0}) is calculated the well-known Tomiyama correlation [69] obtained from experiments in fully contaminated air-water systems.

$$C_{D0} = \max \left[\frac{24}{Re_d} (1 + 0.15 Re_d^{0.687}), \frac{8}{3} \frac{Eo}{Eo + 4} \right] \quad (3.18)$$

Here the dispersed phase Reynolds number and the Eotvos number are defined by Equation 4.10 and Equation 4.11. The relative velocity is $|v_g - v_l|$, g the gravitational acceleration and ρ_c , σ and μ_c respectively the density, surface tension and the dynamic viscosity (μ_c) of the continuous phase.

$$Re_d = \frac{\rho_c |v_g - v_l| d_b}{\mu_c} \quad (3.19)$$

Wall friction

The wall friction (Equation 3.20) is calculated only for the liquid phase and uses the ratio between the perimeter and channel area as hydrodynamic diameter (d_h), as given by Equation 3.21.

$$F_{l \rightarrow w}^W = C_W \frac{1}{2} \rho_l v_l^2 d_h \quad (3.20)$$

$$d_h = \frac{2H_p + 2W_p}{H_p \cdot W_p} \quad (3.21)$$

The wall friction coefficient was determined using the Kowalski equation (Equation 3.22) [70].

$$C_W = 0.079 \cdot (Re_L)^{-1/4} \quad (3.22)$$

The liquid phase Reynolds number can be computed using Equation 3.23.

$$Re_L = \frac{\rho_l v_l d_h}{\mu_l} \quad (3.23)$$

Virtual mass force

The general definition of the virtual mass force (Equation 3.24) takes into account the relative acceleration or deceleration for a particle (or in this case a bubble) moving in a liquid. The virtual mass force is, together with the drag force, an important component of the interfacial momentum transfer. The virtual mass force in Equation 3.24 acts on the dispersed phase. When acting on the dispersed phase the virtual mass force has the opposite sign, similar as with the drag force.

$$F_{c \rightarrow d}^{VM} = C_{VM} \rho_c \varepsilon_d \left(v_c \frac{\partial v_c}{\partial z} - v_d \frac{\partial v_d}{\partial z} \right) \quad (3.24)$$

The virtual mass coefficient C_{VM} is calculated with Equation 3.25 and is composed of the virtual mass coefficient of a single isolated bubble ($C_{VM0} = 0.5$) and the bubble swarm effect. The coefficients for this equation are found in Table 3.3[71].

$$C_{VM} = C_{VM0} + \sum_{k=1}^3 \left\{ \left[a_{k,0} + a_{k,1} \ln \left(\frac{\rho_{d,i}}{\rho_c} \right) \right] \cdot (1 - \varepsilon_c)^k \right\} \quad (3.25)$$

Table 3.3: Coefficients for the Virtual Mass Coefficient in Equation 3.25 [71]

k	$a_{k,0}$	$a_{k,1}$
1	0.130 ± 0.007	0.047 ± 0.002
2	-0.58 ± 0.04	-0.066 ± 0.005
3	1.42 ± 0.06	

3.2.4 Initial Conditions and Boundary Conditions

The detailed design of the steam injector (??) and the schematic overview of the injection nozzle in Figure 2.2 show that steam is injected into the liquid under an angle of 35° . Therefore, the boundary conditions are slightly modified to incorporate the axial injection of steam.

At the boundary ($z = 0$) the volume of steam is set to $\varepsilon_V = 10^{-6}$. The added mass, energy and momentum are then added to Equations 5.13, 3.6 and 3.13. The added mass is calculated within the region $z < 6.97$ mm and is represented by Equation 3.26. In which the ratio of the steam mass flux (ϕ_V'') at the nozzle over the length of the nozzle (L_{inj}).

$$\Gamma_m = \frac{\phi_V''}{L_{inj}} \quad (3.26)$$

The enthalpy of vapour is calculated using an empirical correlation derived from the steam tables [67] in which P_{steam} is the steam pressure in bar.

$$h_V(z = 0) = 253.6P_{steam}^3 - 4762.3P_{steam}^2 + 37124P_{steam} + 2649.3 \times 10^3; \quad (3.27)$$

The velocity profile of steam is assumed to be fully developed at the highly turbulent conditions. The system is initialized assuming a steady state defined by equations 5.13, 3.6 and 3.13.

The thermodynamic properties of vapor are derived using empirical equations from the steam tables [67]. The saturation temperature (T_{sat}) and the vapor phase temperature at the boundary ($T_V(z = 0)$) are calculated using Equation 3.28. The saturation temperature is calculated using the channel pressure whereas the vapor temperature at the boundary is calculated using the steam pressure (again in bar).

$$T_V(z = 0) = -0.9392(P_{steam})^2 + 17.036P_{steam} + 363.662 \quad (3.28)$$

The saturation temperature is calculated via Equation 3.28, however the channel pressure is used rather than the steam pressure.

The numerical details of the model are listed in Table 3.4. It should be mentioned here that the numerical domain is significantly smaller than the actual channel. An important detail is that the discretisation grid has had a logarithmic transformation. This means that the spacing between grid points is not homogeneous. Due to the large gradients that are expected early in the channel it was chosen to have a narrow grid spacing and increase it downstream.

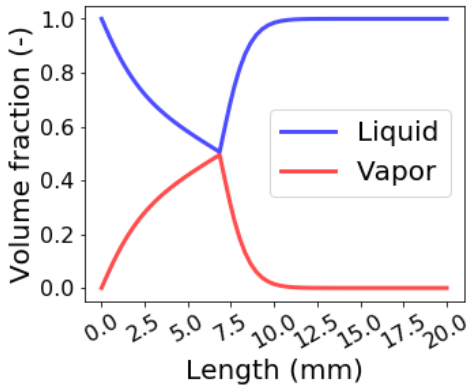
Table 3.4: Numerical details of the model.

Configuration	Value
Lenght	30 mm
Discretisation method	Backward Difference
Order	1 st order
Steps	50
Grid spacing	Logarithmic

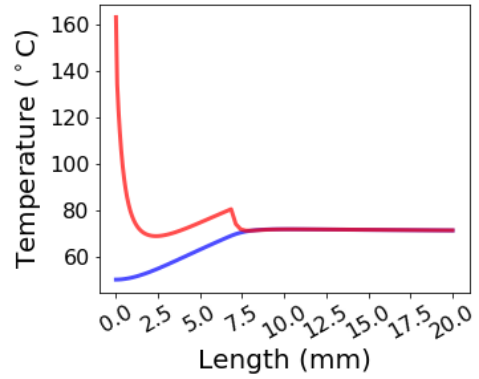
3.2.5 Model results

In Figure 3.2 the volume fraction, temperature, velocity and pressure are shown as function of the axial coordinate. The volume fraction of the vapour phase first increases till the end of the injection zone, after which it decreases. The steam is added linearly over the injection zone. However, since mass transfer to the liquid phase due to condensation occurs along this zone, the volume fraction of gas does not increase linearly along the injection zone. After the injection length the volume fraction of gas continuously decreases due to condensation, until the gas volume fraction 0.001 is reached. From here on, the condensation and heat transfer are neglected and the volume fraction of gas stabilizes around 0.001.

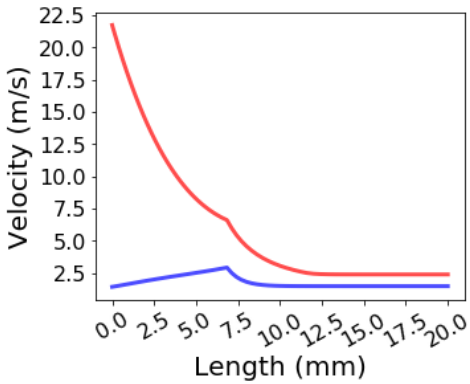
The inlet velocity of the phases equal the superficial velocities at the boundary. In the injection zone the liquid phase velocity increases but beyond this zone it decreases due to friction forces. The kinetic energy of the gas phase transferred to the liquid phase is relatively small, as reported by Qiu et al. [72]. The temperature of the phases also equalize as they are driven by the heat transfer Equation 3.8. From the results shown in Figure 3.2 it can be concluded that the model performs as expected and will subsequently be compared with experimental data.



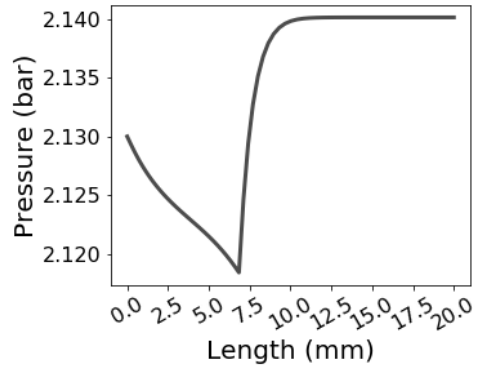
(a) Volume fraction of the phases



(b) Phase temperature



(c) Phase velocity



(d) Channel pressure

Figure 3.2: Results of steady state hydrodynamic model to describe direct contact condensation (liquid flow rate: 12.05 L min^{-1} , steam mass flow rate: 7.6 g s^{-1} , channel pressure: 2.13 bar, steam pressure 5.47 barg).

3.3 Materials and methods

In our experimental set-up (as explained in subsection 2.2.1) several types of sensors are incorporated for pressure and temperature measurements at various locations. A schematic overview of the sensor lay out for these measurements is shown in Figure 2.1 and Figure 2.2. Before and after the injector a magnetic-inductive flow meter (accuracy: 0.8 % of measured value) is installed. The steam mass flow rate is measured indirectly by calculating the difference between the outlet and inlet mass flow rate. The pressure of the injected steam is measured with a pressure transmitter (accuracy: 0.5 %) at the two inlet lines. Calibrated pressure sensors from Kulite (accuracy: 1.1 %) are placed at several locations on the injector. To measure the temperature of the steam boiler, a thermocouple is placed after the opening valve of the steam boiler. The other thermocouples (T-class 1) are placed in the two injection lines and at several locations on the injector. The accuracy is $\pm 0.5^\circ\text{C}$ for the range -40 to $+125^\circ\text{C}$ and $\pm 0.4^\circ\text{C}$ for the range between $+125$ to $+350^\circ\text{C}$. The measured temperature at the entrance of the injector is used to determine the liquid temperature. In Figure 2.2 the numbering system of the sensor locations is shown, Table 3.5 indicates the pressure (P) and temperature (T) sensors connected on the different sensor locations. The pressure and temperature sensors are connected alternately.

Table 3.5: Connected pressure (P) and temperature (T) sensors on different sensor locations of the injector.

Sensor location	1	2	3	4	5	8
A	P	T	P	T	P	T
B	T	P	T	P	T	P

The sensors are connected to a CompactDAQ system of National instruments and the data is collected using LabVIEW software of the same supplier. The CompactDAQ, type 9185, consist of two different modules. The pressure and flow rate meters are connected to a NI-9220 which records the voltage values. The temperature sensors are connected to a NI-9213 which directly converts the voltage from the thermocouples to a digital temperature.

3.3.1 Experimental conditions

For the validation of the model both steady-state performance as dynamic response tests are performed. The experimental conditions used for the steady-state test are listed in Table 3.6. The experiments cover a broad range of water Reynolds numbers with varying water temperature, channel pressure, steam mass flux and steam pressure.

Table 3.6: Experimental conditions that have been applied for steady-state model validation. The experiments are clustered by the water Reynolds number and the water temperature, channel pressure, steam mass flux and steam pressure were varied.

Experiment	Re_L [-]	Water temperature [°C]	Channel pressure [bar]	Steam flux [$kg/(m^2 \cdot s)$]	Steam Pressure [bar]
1	5699	34.9	1.04	503	3.86
2		35.1	1.01	661	4.85
3		48.0	1.03	688	4.52
4		58.0	1.05	700	4.02
5	7028	16.5	3.12	315	4.96
6		16.7	1.20	238	3.31
7		16.4	1.15	490	4.40
8		16.9	3.88	233	4.87
9		17.3	3.87	533	5.54
10		17.4	3.93	287	4.48
11		17.4	3.93	287	4.48
12		17.7	3.95	422	5.02
13		17.7	3.95	605	5.79
14		17.8	3.92	817	7.30
15		36.4	1.24	754	6.10
16		50.7	1.24	727	5.55
17		63.5	1.28	728	4.76
18	14811	34.6	1.24	754	5.55
19		50.1	2.13	754	6.47
20		64.8	2.11	767	6.48

For the dynamic tests either the steam pressure or the liquid mass flow rate was adjusted. For the first test the steam pressure was increased from value A to value B and returned to A after a while. This was performed under three different Reynolds conditions. The second test was by step wise adjusting the mass flow rate of the liquid from high to low.

3.4 Results and discussion

In Figure 3.3 the temperature profile across the injector channel is plotted for various Reynolds numbers using a constant steam mass flux and pressure. It can be observed that for large Reynolds numbers that the top sensors registers a higher temperature than the bottom sensors and that the difference decreases along the length of the injector. This is a result of a small steam penetration into the liquid causing reduced mixing and therefore development temperature gradients. To enable a meaningful comparison the model results are compared against the averaged data of sensors 4, 5 and 8 and are given by Figure 3.4. The model predictions are plotted against the experimental data, averaged over time. The

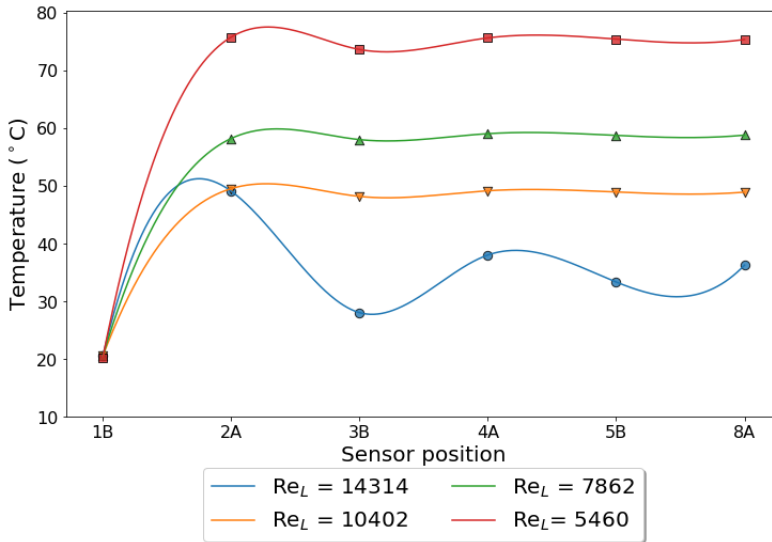


Figure 3.3: Temperature profile across the length of the injector. It can be observed that the depending on the Reynolds number (Re_w) there is a difference between the various sensors. SMF = 204 kg/m²s, Steam pressure = 4.45 bar

experiments are performed using three different Reynold values and color coded for the steam mass flux that was applied. The predicted values are well aligned with the observed experimental values. This shows that the model performance for steady state conditions is good regarding the exhaust temperature of the DCC. This finding indicates that the overall heat balance, heat and mass transfer rates and condensation characteristics are well represented. The results, presented in Figure 3.4, helps to predict the expected exhaust temperature of a steam injector. However, the added value of the developed model is its ability to study the transient response of DCC units with respect to disturbances in key process conditions. Consequently dynamic tests have also been performed.

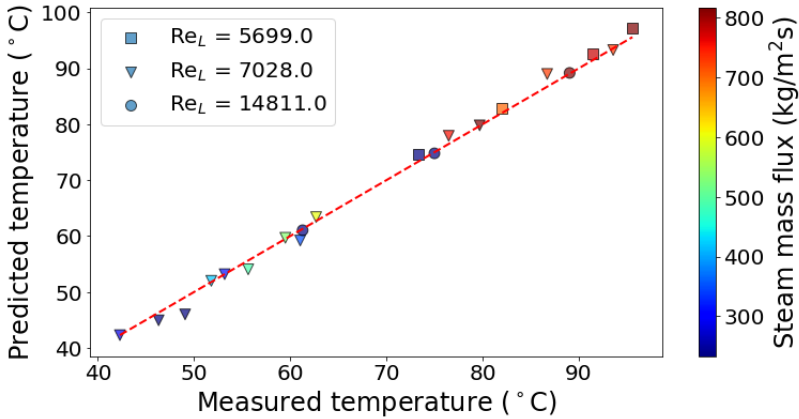


Figure 3.4: Steady-state model results. Model predictions are plotted against measured temperature at the exit of the steam injector. Model shows good agreement with the performed experiments.

3.4.1 Dynamic test

The first dynamic test is performed by increasing the water flow rate whilst keeping the rest of the conditions constant. For the second test the water flow rate is set at the three Reynolds numbers used in Figure 3.4 and during the run the steam pressure is increased and then decreased to the starting value.

For the first dynamic test the water Reynolds number was set to the highest value and then step-wise decreased, as shown in Figure 3.5. The steam pressure was kept constant throughout the experiment. The model itself features more fluctuations than the experimental data. The response to small fluctuations in the steam mass flow measurements have a stronger effect in the model than in the experiments. This is mostly because the model assumes plug flow. In reality recirculation zones exist due to the transient condensation phenomena. Furthermore, the penetration of the steam plume is highly dependent on the Reynolds number. For larger Reynolds numbers the plume penetrates less into the channel and that causes the sensors at the top of the channel to record a higher temperature than the sensors at the bottom. This is noticeable for the first part of the experiment. The variation between the sensors is largest for the highest Reynolds number. The model predictions fall within the error range of values recorded by the sensors. Upon decreasing the Reynolds number the model follows the experimental results well. The fluctuations are still there but the model oscillates around the measured values within an acceptable tolerance.

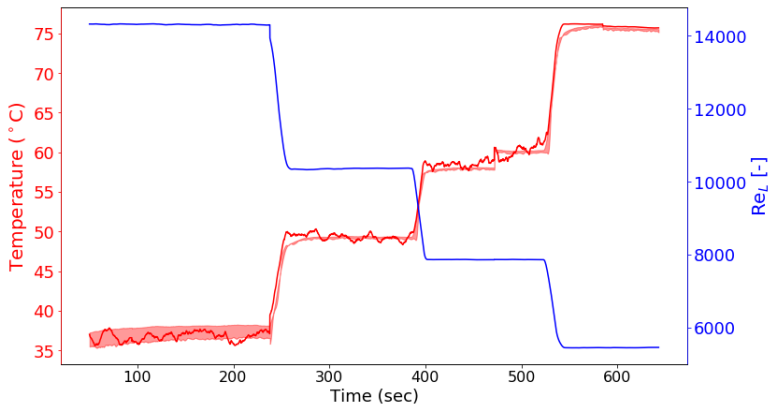


Figure 3.5: [Left axis] The measured water outlet temperature is plotted against the predicted values as a function of time. The experimental data shows a large variation for low high Reynolds numbers. [Right axis] The water Reynolds number (Re_L) is step-wise decreased throughout the experiment. SMF = 204 kg/m²s, Steam pressure = 4.45bar.

In the second test the steam pressure was increased and subsequently decreased, the results are shown in Figure 3.6 for three different Reynolds numbers. Similar to the results in Figure 3.5 the experiment with the largest Reynolds number exhibits the largest variation between the sensors. This is again due to the small penetration depth of steam into the liquid. These experiments have been time-averaged over a longer period because the increase in steam pressure causes the steam mass flow rate sensor to fluctuate stronger. While this fluctuation has a minor effect on the measurement it has a substantial effect on the model outcome.

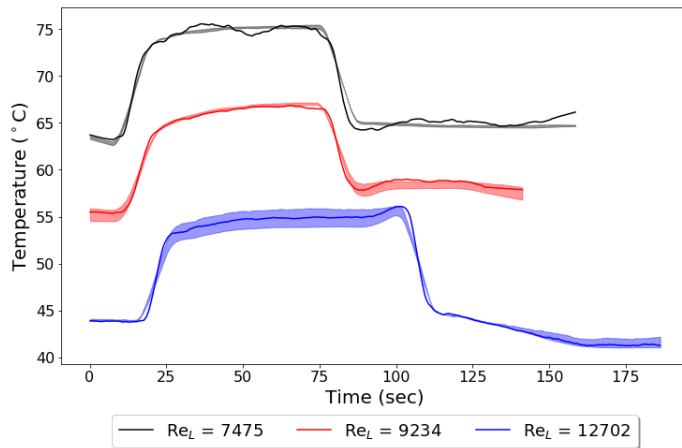


Figure 3.6: The measured water outlet temperature is plotted against the predicted values as a function of time. The steam pressure and as a consequence the steam mass flux (SMF) were increased and returned to the original value. Applied conditions were: $SMF = 620-850 \text{ kg/m}^2\text{s}$, Steam pressure = 4-5 bar

3.5 Conclusion and future work

In this chapter a model was presented to predict the performance of a steam injector using a one-dimensional transient approach. The model was validated against experimental data reported in this study. It was found that the simulated velocity, volume fraction and temperature profiles are in accordance with the expectations. The validation of the model was carried out using steady-state conditions as well as transient conditions. In all conditions the average of the last three sensors was taken in order to obtain a proper basis for comparison. The steady state validation showed that the model is accurate in its predictions. For the dynamic tests the water Reynolds number was step-wise decreased whilst keeping the steam mass flux and pressure constant. For the highest Reynolds number the sensors show the largest variation. This is attributed to a smaller steam penetration depth into the liquid causing in-homogeneous flow. With decreasing Reynolds number the penetration depth increases and as a consequence the mixing improves. Similar behaviour was observed for the second dynamic test in which the steam pressure was increased at various Reynolds numbers. This shows that the model is well-suited for steam injector design and operation in which the fluids are well mixed and feature plug flow behaviour. In future work we will present a more detailed CFD model for more detailed and refined predictions.

References

- [44] D. Heinze, T. Schulenberg, and L. Behnke. “A physically based, one-dimensional three-fluid model for direct contact condensation of steam jets in flowing water”. *International Journal of Heat and Mass Transfer* 106 (2017), pp. 1041–1051. DOI: 10.1016/j.ijheatmasstransfer.2016.10.076.
- [60] S.S. Safavi Nic, T.E. Kuipers, K.B. Buist, R.E.M. Verdurmen, and J.A.M. Kuipers. “A transient mechanistic two-fluid model for Direct Contact Condensation”. *Chemical Engineering Science* (2023).
- [61] S.S. Safavi Nic, K.B. Buist, R.E.M. Verdurmen, and J.A.M. Kuipers. “Dynamic model to predict heat-induced protein denaturation and fouling in a Direct Contact Steam Condensation process”. *Chemical Engineering Science X* 8 (2020), pp. 841–855.
- [62] Z. Zhang, D. Chong, and J. Yan. “Modeling and experimental investigation on water-driven steam injector for waste heat recovery”. *Applied Thermal Engineering* 40 (2012), pp. 189–197. DOI: 10.1016/j.applthermaleng.2012.02.006.
- [63] H. Ma, H. Zhao, L. Wang, Z. Yu, and X. Mao. “Modeling and investigation of a steam-water injector”. *Energy Conversion and Management* 151.May (2017), pp. 170–178. DOI: 10.1016/j.enconman.2017.08.068.
- [64] S.S. Gulawani, S.K. Dahikar, C.S. Mathpati, *et al.* “Analysis of flow pattern and heat transfer in direct contact condensation”. *Chemical Engineering Science* 64.8 (Apr. 2009), pp. 1719–1738. DOI: 10.1016/j.ces.2008.12.020.
- [65] A. Pecenko. “Numerical Simulation Methods for Phase-Transitional Flow”. PhD thesis. Eindhoven University of Technology, 2010. DOI: 10.6100/IR691427.
- [66] S.K. Dahikar, M.J. Sathe, and J.B. Joshi. “Investigation of flow and temperature patterns in direct contact condensation using PIV, PLIF and CFD”. *Chemical Engineering Science* 65.16 (Aug. 2010), pp. 4606–4620. DOI: 10.1016/j.ces.2010.05.004.
- [67] M.D. Koretksky. *Engineering and Chemical Thermodynamics*. Ed. by M.D. Koretksky. John Wiley and Sons, 2012, pp. 648–652.
- [68] A. Buffo, M. Vanni, P. Renze, and D.L. Marchisio. “Empirical drag closure for polydisperse gasliquid systems in bubbly flow regime: Bubble swarm and micro-scale turbulence”. *Chemical Engineering Research and Design* 113 (Sept. 2016), pp. 284–303. DOI: 10.1016/j.cherd.2016.08.004.
- [69] A. Tomiyama, I. Kataoka, I. Zun, and T. Sakaguchi. “Drag Coefficients of Single Bubbles under Normal and Micro Gravity Conditions”. *JSME International Journal Series B* 41 (Feb. 1998), p. 472. DOI: 10.1299/jsmeb.41.472.
- [70] J.E. Kowalski. “Wall and interfacial shear stress in stratified flow in a horizontal pipe”. *AIChE Journal* 33.2 (1987), pp. 274–281. DOI: 10.1002/AIC.690330214.
- [71] T.M. Nijssen, H.A. Kuipers, J. van der Stel, A.T. Adema, and K.A. Buist. “Complete liquid-solid momentum coupling for unresolved CFD-DEM simulations”. *International Journal of Multiphase Flow* 132 (Nov. 2020). DOI: 10.1016/j.ijmultiphaseflow.2020.103425.

References

- [72] B. Qiu, J. Liu, J. Yan, D. Chong, and X. Wu. “Experimental investigation on the driving force and energy conversion in direct contact condensation for steam jet”. *International Journal of Heat and Mass Transfer* 115 (Dec. 2017), pp. 35–42. DOI: 10.1016/j.ijheatmasstransfer.2017.06.126.

Chapter 4

A Computational Fluid Dynamics model to analyze the mechanics inside a Steam Injector

Abstract

The use of a Computational Fluid Dynamics (CFD) model is used for a DCC process to investigate flow directionality, temperature gradients and to optimize the injector design. The CFD model presented in this chapter uses an Eulerian Multiphase model (EMP) with a RANS $k-\omega$ turbulence model. The model was qualitatively validated against experimental data. The experimental data was obtained using a high-speed camera and PIVlab to obtain velocity fields. The obtained data is only suitable as qualitative data due to formation of a large steam cavity and bubbles which in combination with volume-based lighting leads to difficulties in obtaining a complete vector field. The model however does produce a similar flow structure, and velocity gradients. In addition from the CFD simulations it is apparent that the "jetting" regime leads to the formation of a local hot-spot whilst the radial temperature distribution is homogeneous. Finally it is also found that the "bubbling" region features a larger radial temperature gradient.

4.1 Introduction

In our previous research [38] an experimental study was reported to generate regime maps utilizing a machine learning approach to predict the prevailing operating regime, ranging from chugging, bubbling and jetting. However, these regime maps do not predict a priori what the performance and temperature gradients of a DCC process will be. In the previous chapter a 1D model was used to predict the temperature profiles. Whilst the model results were in good agreement with experimental data limitations were encountered in the heterogeneous flow regime.

To obtain data on temperature gradients with limited access to experimental data a viable option would be a Computational Fluid Dynamics (CFD) approach. An overview of several reported studies on DCC modelling are given in Table 4.1. CFD models provide the added value to model and study the impact of geometry of the DCC design and nozzle position on the condensation rate and mixing behaviour. CFD models are computationally expensive, limiting the time scales for simulations to a few seconds. These time scales are however sufficient to gather statistics on the hydrodynamic behavior, but unfortunately are not suited to study the formation of protein deposit layers as these time scales can approach to several hours [61]. The assumption of well-defined 1D homogeneous flow as in the 1D models however does not always hold as, depending on the flow regime, steam can either penetrate marginally into the flowing liquid causing a radial temperature gradient or can penetrate significantly causing flow recirculation as described in chapter 3. The application of a CFD model is beneficial to study the flow behaviour, condensation dynamics and temperature gradients in more detail. From an industrial perspective this has the benefit to provide either understanding of the systems performance during operation or to evaluate system performance prior to purchasing.

The work published in literature using the computational approach consists out of CFD-studies and simplified models. For CFD modelling Pecenko et al. (2010) [65] adopted a diffuse-interface model coupled with Large Eddy Simulations (LES) for turbulent multiphase flow. Dahikar [66] performed CFD-simulations using both LES and $k-\epsilon$ RANS (Reynolds-Averaged Navier-Stokes) models and compared the results with PIV measurements of steam injection in a pool of water. Gulawani et al. (2009) [73] executed both experiments and CFD-simulations. These simulations, showed to be in good agreement with the experiments. However their model was specifically designed and fine-tuned for this experimental setup and therefore the general applicability of this model is questionable.

Table 4.1: Overview of key CFD models for DCC.

Authors	Method	Approach	Deliverable
Gulawani et al.[64]	CFD	RANS	Validating predicted heat transfer coefficient values
Pacenko et al.[65]	CFD	DIM-LES	Development of an improved CFD model for industrial applications
Dahikar et al.[66]	CFD	LES and RANS	Evaluation of predicted velocity against experimentally obtained velocity

The goal of this research is to present a transient CFD two-fluid model to predict the gradients inside a steam injector including the prediction of the exhaust temperature. Our model accounts for an interface at the jet as well as bubble condensation and is validated with experimental data. This study is therefore divided into three parts: (1) description of the experiments (2) model description and (3) model validation.

4.2 Model description

Our model takes a classical two-fluid approach in which the vapour (V) and liquid (L) phase are modelled separately. The experimental set-up described in chapter 2 can be operated at a liquid Reynolds number in the range of $5646 < \text{Re}_L < 15000$. The system is modelled using a Reynolds-Averaged Navier Stokes (RANS) turbulence model. The choice of this model over a scale-resolving model is that it is less computationally expensive. The RANS turbulence model that is employed is the $k-\omega$ model [74] adaptation of Menter [75]. The phases are modelled as interpenetrating continua. The schematic representation is similar as presented in Figure 2.2, however in this work the Virtual Mass force (VMF) is not included. The use of saturated steam allows for the assumption that the condensation mode is heat transfer limited rather than mass transfer limited. The steam properties are derived from the steam thermodynamic table [67].

The model is based on the assumption of three types of flow interactions based on the nature of the phase boundary; a bubbly regime in which gas is dispersed in the liquid, a dispersed droplet regime and an interface regime. The employed thresholds for the regime changes are listed in Table 3.2.

4.3 Eulerian Multiphase Flow

The DCC-system used in the experimental setup contains only one component, water. However, the water can be either in the gas phase or the liquid phase. The DCC system can behave as two separate continuous phases and or as a continuous-dispersed system. Therefore, the Eulerian multiphase flow modelling approach has been adopted, since it is specifically designed to describe more than one phase and is not limited to a continuous and dispersed phase. Furthermore, a choice was made for the Eulerian multiphase segregated flow instead of using a Eulerian multiphase mixture approach, which is often applied to purely bubbly or droplet flow where the phases are miscible. For the Eulerian multiphase mixture approach, the transport equations of mass, momentum and energy are solved together for the mixture. While for the first case, Eulerian multiphase segregated flow, for each phase the transport equations where solved, but the phases share a common pressure field.

The shared flow domain is occupied by the two phases, where the presence of each phase is represented through its volume fraction ε .

$$V_i = \int_V \varepsilon_i dV \quad (4.1)$$

The volume fraction of the liquid (product) and the gas (steam) phase is defined according to Equation 4.2.

$$\varepsilon_l + \varepsilon_g = 1 \quad (4.2)$$

The conservation equation of mass, momentum and energy for phase i are respectively given by Equation 4.3, 4.4 and 4.5. The i and j subscripts represent the phase indices. The DCC system consists out of two phases, either steam or liquid water as given by

Equation 4.2.

$$\frac{\partial}{\partial t} \int_V \varepsilon_i \rho_i dV + \oint_A \varepsilon_i \rho_i \mathbf{v}_i \cdot d\mathbf{A} = \int_V \sum_{j \neq i} (\Gamma_{j \rightarrow i} - \Gamma_{i \rightarrow j}) dV + \int_V S_i^\varepsilon dV \quad (4.3)$$

The continuity equation is dependent on the volume fraction ε , the density ρ , volume V , velocity \mathbf{v} , the mass transfer rate to phase i from phase j $\Gamma_{j \rightarrow i}$, the mass transfer to phase j from phase i $\Gamma_{i \rightarrow j}$ and the user-defined phase mass source term S^ε . This last term is currently excluded in our model.

The momentum equation is given by Equation 4.4. The left-hand side contain the material derivative of momentum. Whereas the right-hand side the equation accounts for the effect of hydrostatic forces, the gravitational forces, the viscous and interaction forces. The last term on the right is the momentum exchange due to mass transfer.

$$\begin{aligned} \frac{\partial}{\partial t} \int_V \varepsilon_i \rho_i \mathbf{v}_i dV + \oint_A \varepsilon_i \rho_i \mathbf{v}_i \otimes \mathbf{v}_i \cdot d\mathbf{A} = & - \int_V \varepsilon_i \nabla p dV + \int_V \varepsilon_i \rho_i \mathbf{g} dV \\ & + \oint_A [\varepsilon_i (\boldsymbol{\tau}_i + \boldsymbol{\tau}_i^t)] \cdot d\mathbf{a} + \int_V \mathbf{M}_i dV + \int_V (\mathbf{F}_{int})_i dV + \int_V \mathbf{S}_i^\varepsilon dV + \\ & \int_V \sum_{j \neq i} (\Gamma_{j \rightarrow i} \mathbf{v}_j - \Gamma_{i \rightarrow j} \mathbf{v}_i) dV \end{aligned} \quad (4.4)$$

Here, p is the pressure, \mathbf{g} the gravity vector, $\boldsymbol{\tau}$ and $\boldsymbol{\tau}^t$ are respectively the molecular and turbulent stresses, \mathbf{M} the inter-phase momentum transfer (virtual mass and drag forces), (\mathbf{F}_{int}) the internal forces and the \mathbf{S}^ε is in this case the phase *momentum* source term, which also is excluded in our model.

Lastly, the third governing equation, the conservation of internal energy is given by Equation 4.5.

$$\begin{aligned} \frac{\partial}{\partial t} \int_V \varepsilon_i \rho_i E_i dV + \oint_A \varepsilon_i \rho_i H_i \mathbf{v}_i \cdot d\mathbf{A} = & \oint_A \varepsilon_i \lambda_{eff,i} \nabla T_i d\mathbf{A} + \\ & \oint_A \boldsymbol{\tau}_i \cdot \mathbf{v}_i d\mathbf{A} + \int_V \mathbf{f}_i \cdot \mathbf{v}_i dV + \\ & \int_V \sum_{j \neq i} Q_{ij} dV + \int_V \sum_{(ij)} Q_i^{ij} dV + \int_V S_{u,i} dV + \\ & \int_V \sum_{j \neq i} (\Gamma_{ij} - \Gamma_{ji}) h_i(T_{ij}) dV \end{aligned} \quad (4.5)$$

E is the total phase energy, H the total phase enthalpy, λ_{eff} the effective thermal conductivity, T the temperature, \mathbf{f}_i the body force vector, Q_{ij} and $Q_i^{(ij)}$ respectively the heat transfer rate from phase j to phase i and the heat transfer rate from phase pair interface (ij) to phase i . The first term accounts for transfer due to a temperature difference between phases, the second account for phenomena such as condensation. \mathbf{S}_u represents the energy source and is set to zero and $h(T_{ij})$ the phase enthalpy that is evaluated at the interface temperature T_{ij} .

4.3.1 Closures

To be able to solve the system a few closures are introduced and have been listed in Table 4.2. First of all, the inter-phase momentum transfer between the phases needs to be specified taking into account Newton's third law. The momentum transfer contains several forces such as the drag force. The drag-force between the dispersed phases is given by Equation 4.6. Here, W_t is the weight function added to take into account the different

drag forces in the different regimes, C_D is the drag coefficient and \mathbf{v}_r the relative velocity between the dispersed phase d and the continuous phase c ($v_d - v_c$), a_{cd} is the interface area between the continuous and dispersed phase. The drag coefficient (C_D) is valid for dilute flow conditions and corrects the drag coefficient for isolated bubbles (C_{D0}) by including the bubble swarm effect ($f(\varepsilon_V)$). The correction function ($f(\varepsilon_V)$) is given by the power-law correction in Equation 4.8 [68]. This power law function has a discontinuity at which for volume fractions larger than this threshold the vapour phase is no longer dispersed. The empirical parameter (C_A) is usually in the range $-3 < C_A < -1$. Buffo et al[68] found, after performing a sensitivity analysis, that this value is $C_A = -1.3$. The single bubble drag coefficient (C_{D0}) is calculated with the well-known Tomiyama correlation [69] obtained from experiments in fully contaminated air-water systems. This is applied for the Bubbly and Droplet regimes. Here the dispersed phase Reynolds number and the Eotvos number are defined by Equation 4.10 and Equation 4.11. The relative velocity is $|v_g - v_l|$, g the gravitational acceleration and ρ_c , σ and μ_c respectively the density, surface tension and the dynamic viscosity (μ_c) of the continuous phase.

The Strubelj-Tiselj correlation, given by Equation 4.12, is chosen for the Interface regime. It accounts for a large interface. Also a relaxation time is required. Low relaxation time scale t_{SC} helps instantaneous equalizing of velocities of both of the phases and reduces the slip in that region. t_{SC} is taken at 0.01 s. Here, ε_p and ε_s are respectively the volume fraction of the continuous phase and the volume fraction of the dispersed phase. ρ_p and ρ_s are the densities of the primary and secondary phase [76].

The turbulent dispersion force takes into account the natural redistribution of mass due to non-uniformities of phase concentration and is implemented in the CFD model with Equation 4.13 where W the weight function values are from the regime onsets, C_D is the drag coefficients per regime earlier defined. ν is the turbulent kinetic viscosity and Pr the Prandtl number. Both have specific values for either the primary or secondary phase, or even the intermediate regime.

The energy E_i is related to the total enthalpy H_i by Equation 4.15. In addition the total enthalpy is calculated with the phase enthalpy h_i , Equation 4.16. Here, h_i^{REF} and T_i^{REF} are respectively the heat of formation and the temperature of phase i at a reference temperature. It is assumed that the mass transfer happens through phase change only, in this case the steam is condensed into the product phase water. The heat transfer rates have to satisfy the heat balance in Equation 4.18 with Δh_{ij} as the heat of evaporation, the heat required to produce phase i from phase j. It can be calculated from the phase enthalpy at the inter-phase temperature (T_{ij}).

The mass transfer from the gas to the liquid can be calculated with the Spalding evaporation and condensation model. The model is generally used for multi-component systems. The 1D-condensation model in this report is used to describe a one-component process (steam condenses into liquid water). Furthermore, the Spalding model is designed for systems with a liquid dispersed phase. The definition of the Spalding model can then be found in Equation 4.21-4.23 with g^* as the mass transfer conductance in $\text{kg m}^{-2} \text{s}^{-1}$, B is the Spalding transfer number, which is the definition for the driving force of condensation. The Spalding transfer number takes the ratio between the temperature difference between the phases and the latent heat of vaporization (h_V).

Table 4.2: Closure equations to calculate interphase momentum, energy and mass transfer.

$$F_{d \rightarrow c}^D = \sum_{t=FR,IR,SR} W_t C_D \frac{1}{2} \rho_c |\mathbf{v}_r| \left(\frac{a_{cd}}{4} \right) \mathbf{v}_r \quad (4.6)$$

$$C_D = f(\varepsilon_V) C_{D0} \quad (4.7)$$

$$f(\varepsilon_V) = \begin{cases} (1 - \varepsilon_V)^{C_A} & \varepsilon_V \leq 0.5 \\ 1 & \varepsilon_V > 0.8 \end{cases} \quad (4.8)$$

$$C_{D0} = \max \left[\frac{24}{\text{Re}_d} (1 + 0.15 \text{Re}_d^{0.687}), \frac{8}{3} \frac{\text{Eo}}{\text{Eo} + 4} \right] \quad (4.9)$$

$$\text{Re}_d = \frac{\rho_c |v_g - v_l| d_b}{\mu_c} \quad (4.10)$$

$$\text{Eo} = \frac{g(\rho_c - \rho_d) d_b^2}{\sigma} \quad (4.11)$$

$$F_{IR}^D = \frac{1}{t_{SC}} \varepsilon_p \varepsilon_s (\varepsilon_p \rho_p + \varepsilon_s \rho_s) \mathbf{v}_r \quad (4.12)$$

$$F_{d \rightarrow c}^{TD} = \left(W_{fr} \frac{C_D^{fr} \nu_p}{Pr_p} + W_{ir} \frac{C_D^{ir} \nu_{ir}}{Pr_{ir}} + W_{sr} \frac{C_D^{sr} \nu_s}{Pr_s} \right) \left\{ \frac{\nabla \varepsilon_s}{\varepsilon_s} - \frac{\nabla \varepsilon_p}{\varepsilon_p} \right\} \quad (4.13)$$

$$\lambda_{eff,i} = \lambda_i + \frac{\mu_{t,i} c_{p,i}}{Pr_{t,i}} \quad (4.14)$$

$$E_i = H_i - \frac{p}{\rho_i} \quad (4.15)$$

$$H_i = h_i + \frac{|\mathbf{v}_i|^2}{2} \quad (4.16)$$

$$h_i(T_i) = h_i^{REF} + \int_{T_i^{REF}}^{T_i} c_{p,i}(T') dT' \quad (4.17)$$

$$Q_i^{(ij)} + Q_j^{(ij)} + \Phi_{MT}^n = 0 \quad (4.18)$$

$$\Phi_{MT}^n = \Delta h_{ij} \Gamma_{g \rightarrow l} \quad (4.19)$$

$$\Delta h_{ij} = h_i(T_{ij}) - h_j(T_{ij}) \quad (4.20)$$

$$\Gamma_{g \rightarrow l} = g^* \cdot \ln(1 + B) \quad (4.21)$$

$$g^* = \frac{k_l \cdot \text{Nu}_d}{c_p \cdot d_b} \quad (4.22)$$

$$B = \frac{c_p (T_V - T_L)}{h_V} \quad (4.23)$$

4.4 Materials and methods

The CFD model was implemented in Siemens Star-CCM+ version 18.02.008-r8. Only the segment illustrated in red in Figure 4.1 has been meshed and resolved. This allows the use of the sensor values as boundary conditions and the simulation domain is taken until after the sapphire window.

Simcenter STAR-CCM+

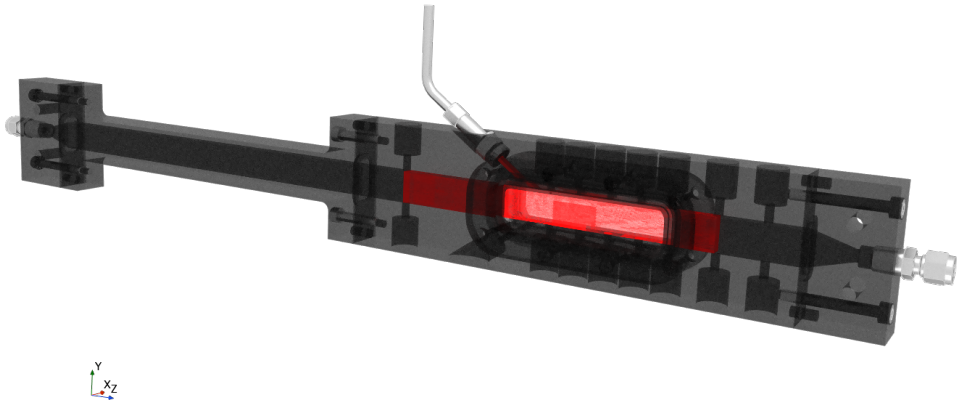


Figure 4.1: The simulation domain has been highlighted in red. The domain starts from the first sensors and extends to the first sensor after the glass window. The total length of the domain is 210 mm.

The mesh was generated using a polyhedral mesher with local refinement around the injection area and is shown in Figure 4.2. Local refinement is required for two reasons. The first is the large velocity difference between the liquid and vapour phase. The second is that due to condensation the boundary between vapour and liquid is dynamic and can collapse. To prevent numerical instability due to condensation a locally smaller mesh is required.

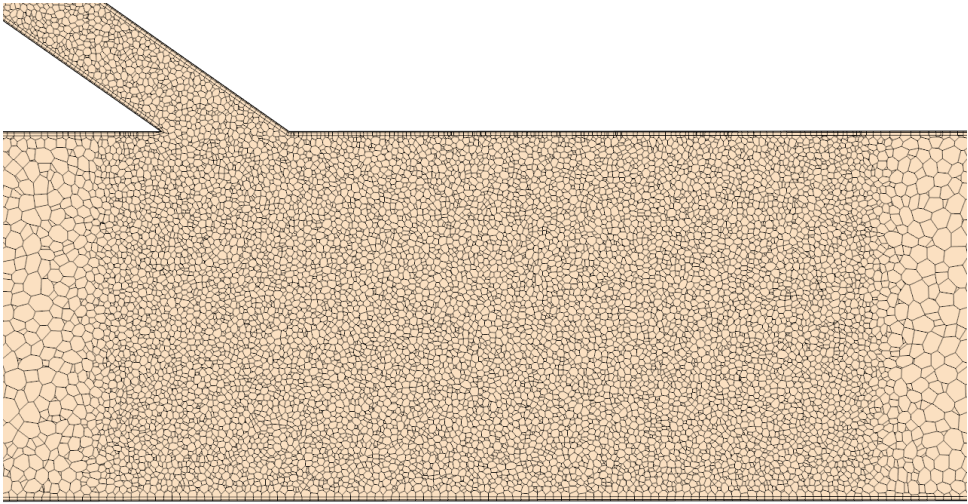


Figure 4.2: A 2D representation of the polyhedral mesh with local refinement around the injection area. In total 430k cells are generated.

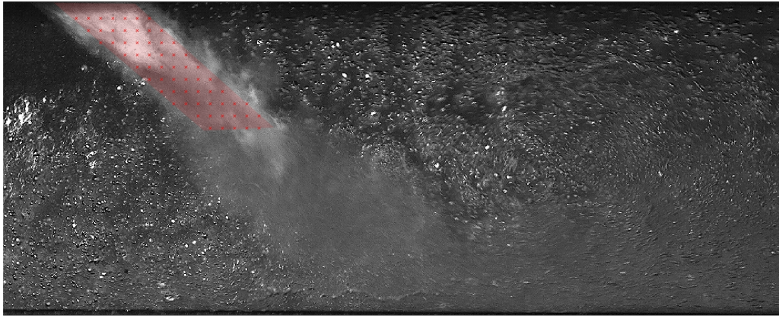
4.5 Experimental set-up

In our experimental set-up several types of sensors are incorporated for pressure and temperature measurements at various locations. A schematic overview of the sensor layout for these measurements is shown in Figure 2.1 and Figure 2.2. Before and after the injector a magnetic-inductive flow meter (accuracy: 0.8 % of measured value) is installed. The steam mass flow rate is measured indirectly by calculating the difference between the outlet and inlet mass flow rate. The pressure of the injected steam is measured with a pressure transmitter (accuracy: 0.5 %) at the two inlet lines. Calibrated pressure sensors from Kulite (accuracy: 1.1 %) are placed at several locations on the injector. To measure the temperature of the steam boiler, a thermocouple is placed after the opening valve of the steam boiler. The other thermocouples (T-class 1) are placed in the two injection lines and at several locations on the injector. The accuracy is $\pm 0.5^\circ \text{C}$ for the range -40 to $+125^\circ \text{C}$ and $\pm 0.4^\circ \text{C}$ for the range between $+125$ to $+350^\circ \text{C}$. The measured temperature at the entrance of the injector is used to determine the liquid temperature.

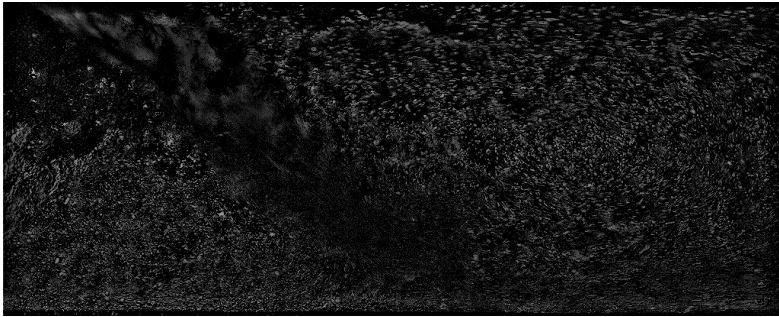
The sensors are connected to a CompactDAQ system of National instruments and the data is collected using LabVIEW software of the same supplier. The CompactDAQ, type 9185, consist of two different modules. The pressure and flow rate meters are connected to a NI-9220 which records the voltage values. The temperature sensors are connected to a NI-9213 which directly converts the voltage from the thermocouples to a digital temperature.

4.5.1 PIV measurements

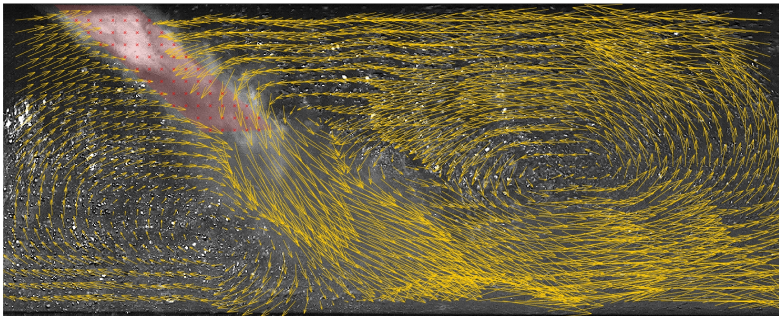
To gain insight into the flow behavior inside the injector channel during steam injection, PIVlab is used. PIVlab is a graphical user interface particle image velocimetry software package, which is programmed in Matlab and requires the image processing toolbox. PIV analysis consists of three main steps, image pre-processing, image evaluation, and post-processing [77]. The PIVlab environment facilitates these three steps. Figure 4.3b shows the result of the image after the first pre-processing step. A contrast limited adaptive histogram equalization (CLAHE) and an intensity high pass are applied during this step. CLAHE enhances the readability of the image data by amplifying contrast in an image. The high-intensity pass emphasizes the bubbles by removing the high-intensity light reflecting from the steam plume. For the CLAHE and the high pass kernel size, the recommended sizes of PIVlab are used, 64 and 15 pixels, respectively. The next step is the image evaluation step. This step applies the Fast Fourier Transform window deformation. Small interrogation areas of a pair of images are combined to derive the most probable particle, or in this case, bubble displacement. A multi-pass method is applied where an interrogation area of 64 pixels is first analyzed, and a smaller area of 32 pixels afterwards. Finally, image post-processing is applied. This step involves velocity and image-based validation. Velocity validation is applied manually by choosing acceptable velocity limits. The image validation allows the user to choose low and high-contrast filters. PIVlab also suggests values for both filters. For the low contrast filter, a value of 0.0073 was suggested, which gave satisfying results. The suggested high contrast filter removed all the vectors, so a value of 0.7 was manually determined. Figure 4.3c shows the final PIV after all the processing steps. In the final step also, the appearance of the arrows can be altered. Moreover, the software can create velocity and vorticity images based on vector data. It should be noted that there are no tracer particles used, so only the movement of the bubbles can be used by PIVlab to establish the flow patterns. In contrast to tracer particles, these bubbles differ in size and shape, resulting in a less accurate prediction of the movement inside the channel. Nevertheless, this method still can provide a general idea of the main flow directions, but should not be used as a quantitative measurement of velocity.



(a) Original Image.



(b) Pre-processing step.



(c) Final PIV image after image validation.

Figure 4.3: For the PIV analysis the original image (Figure 4.3a) is first pre-processed (Figure 4.3b) prior to the PIV analysis. After the PIV analysis outliers are removed and velocity magnitude is calculated Figure 4.3c.

4.6 Results and discussion

4.6.1 Open back pressure valve

For the simulation at low channel pressure an experiment with a channel pressure of 1.6 bar is used with a water inlet flow rate of 88.6 g s^{-1} and a steam mass flow rate of 7.7 g s^{-1} . For this experiment we can clearly observe a jetting behaviour. The original image, as well as the PIV results are given in Figure 4.3. Due to the low channel pressure the steam plume penetrates the channel and causes large, deformable bubbles that are not ideal for PIV analysis.

The PIV image corresponding to this experiment is shown in Figure 4.3c. The segment in which the steam plume is dominant has been excluded from the image analysis as it generates unreliable data. The liquid velocity profile shows two major recirculation areas. One directly at the beginning of the image and one after the steam plume. The steam plume pushes the fluid to the bottom of the injector forcing the two recirculation areas.

In Figure 4.4, the simulated velocity profile of a steam injection process with a low channel pressure is shown. The simulated recirculating flow before injection extends all the way to the bottom of the channel, similarly to the PIV image shown in Figure 4.3c. The simulated recirculating pattern after injection is also discernible in Figure 4.3c. This circulating flow profile is located more in the center of the channel. Additionally, after injection a strong forward moving flow is seen, in the simulation, at the bottom of the channel and a backward moving flow at the top. Even the expected magnitude of the velocity is approximately the same. Although, in Figure 4.3c, the movement of the bubbles is tracked and one should be cautious with assuming that the liquid has exactly the same velocity. Altogether, the simulation is capable of predicting the main important features of the flow.

Figure 4.5 shows the temperature profile and similarly to Figure 4.8, the temperature profile is largely determined by the flow profile. The temperature is distributed due to the flow patterns given in Figure 4.4. The circulating pattern before injection increases the temperature already slightly. After injection, in the middle of the recirculation pattern, a local minimum of temperature can be found. But most interesting is the local hotspot, it is not formed at the location of the steam jet, but more on the right side of the steam jet. An explanation can be provided with the recirculating pattern. The heat, due to the recirculating pattern, is transferred from the bottom to the top. From the top the liquid flows directly into the jet again. This results in a pre-heated fluid being heated even more, which creates a local hotspot.

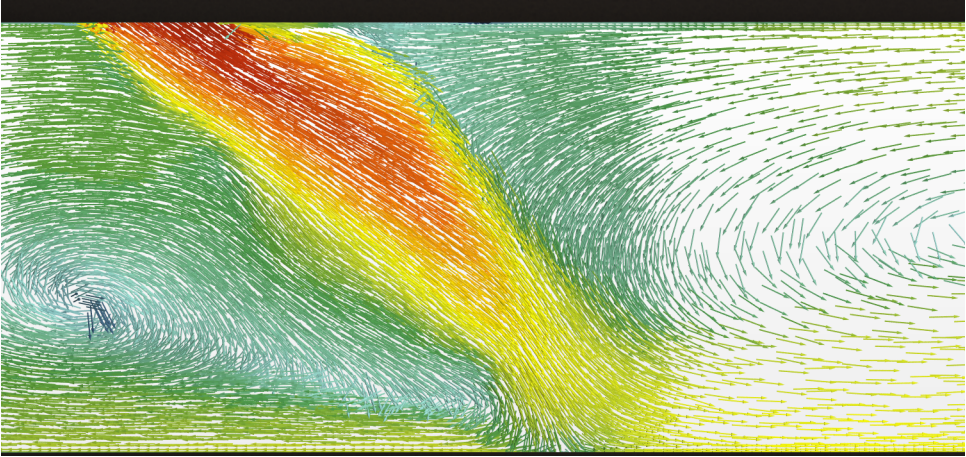


Figure 4.4: Velocity map obtained from the CFD model. The vectors show the same directionality and location of vortices as the experiment does. The timestep on average was 5×10^{-6} seconds with 15 implicit iterations. Liquid flow rate: 88.6 g s^{-1} , steam mass flow rate: 5 g s^{-1} , open back pressure valve (channel pressure: 1.3 bar)

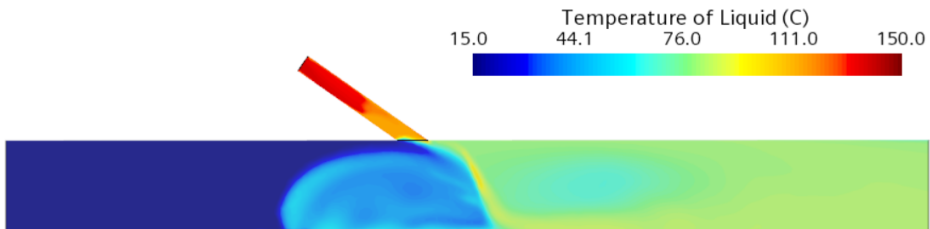


Figure 4.5: Simulated temperature profile for steam injection with low channel pressure

4.6.2 Partially closed back pressure valve

An experiment with a channel pressure of 4 bar was simulated as well using a water inlet flow rate of 240 g s^{-1} and a steam mass flow rate of 5 g s^{-1} . These conditions resulted in an outlet temperature of $33.1 \text{ }^\circ\text{C}$. The PIV image taken from this experiment is shown in Figure 4.6.

Figure 4.7 can be compared to the flow direction given in Figure 4.6. The simulated velocity is mostly increased in the upper part in the channel. Furthermore, there is flow reversal in the lower region of the channel. Lastly, just below the exit of the steam nozzle the back flow from the lower region and the forward flow before injection joins the forward flow due to steam injection. The flow direction profile presented in Figure 4.6 features all three phenomena that were mentioned.

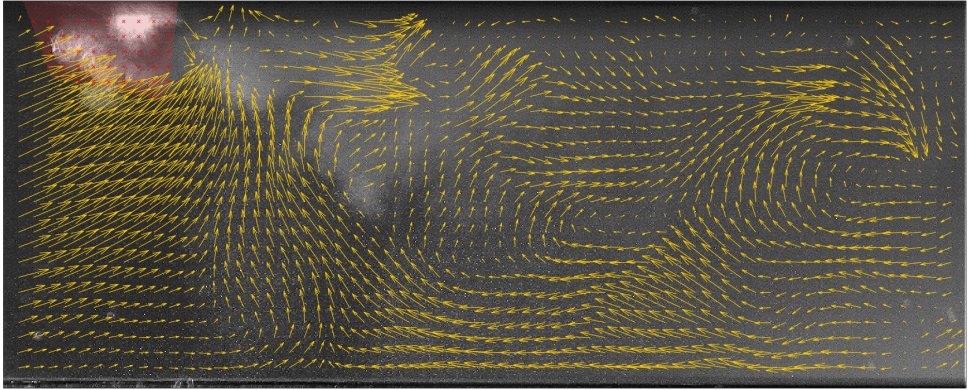


Figure 4.6: Velocity vectors generated by PIVLab. The experimental conditions caused the process to operate in the "bubbling" regime. The area in which the steam plume resides has been omitted from the analysis. $\phi_m^w = 240 \text{ g s}^{-1}$, $\phi_m^s = 5 \text{ g s}^{-1}$, $P_{BPV} = 4 \text{ bar}$, $T_{in}^w = 15^\circ\text{C}$.

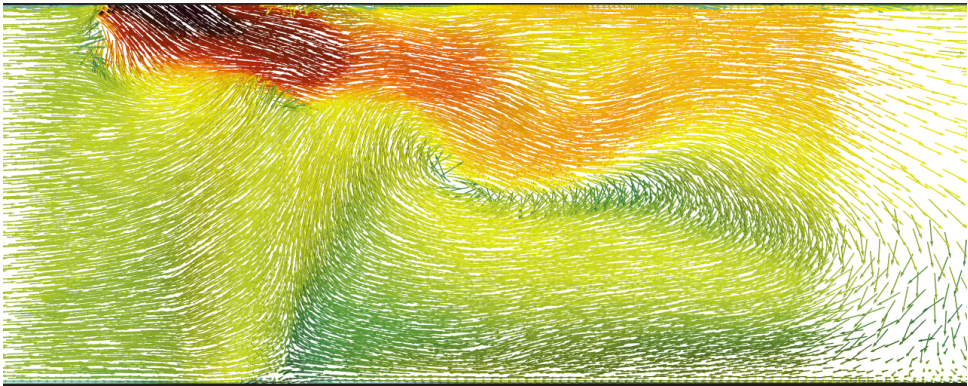


Figure 4.7: Velocity map obtained from the CFD model. The vectors show the same directionality and location of vortices as the experiment does. The time step on average was 3×10^{-5} seconds with 15 implicit iterations.

Figure 4.8 shows the temperature profile in the channel. Interesting to observe is a temperature front that is formed under the steam jet. This can be explained by the flow behavior visualized in Figure 4.7. The recirculation pattern leading to flow reversal moves the heat also to the lower regions of the channel. However, the back flow "collides" with the cold forward moving stream, which produces an upward moving stream joining the hot liquid again. This temperature profile must be improved by a more homogeneous distribution of the injected heat, the liquid temperature close to injection location is more than 30 degrees higher than the outlet temperature. The outlet temperature for this simulation equals 34.3°C , which is in close agreement to the 33.1°C obtained experimentally.

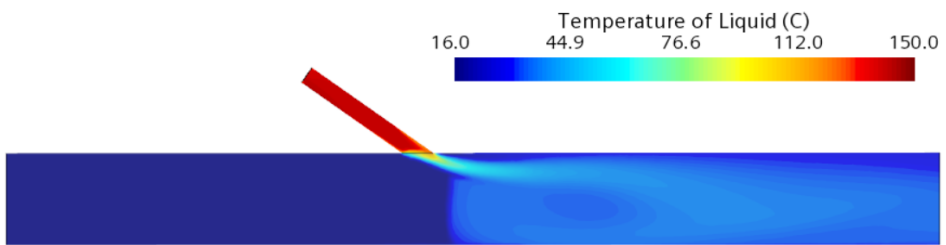


Figure 4.8: Simulated temperature profile for steam injection with high channel pressure.

4.7 Conclusion

In this chapter the use of a commercial CFD-package was reported to investigate the velocity and temperature distributions inside a rectangular channel with steam injection. The Eulerian/Eulerian multiphase approach with a multiple-flow regime topology was adopted for this purpose. The turbulence was modelled using $k-\omega$ RANS-model. The experimental data was generated using a high-speed camera and PIVlab to obtain velocity maps. The experimental method required the use of LED-front lighting due to the positioning of a bottom injection point and sensor placement. These two factors combined made it not feasible to use a laser to illuminate the PIV field of interest. Small dispersed gas bubbles proved to be useful as PIV particle trackers, however, at low back-pressure the size of these bubbles is too large to be used as proper tracer particles. In addition the LED front lighting resulted in a volume-averaged velocity profile data which can not be directly compared to the CFD results. The obtained data was therefore used to qualitatively validate the CFD model predictions featuring a transition due to the altered channel pressure. For the jetting regime the steam plume penetrates the channel and produces two re-circulation zones which are both captured by the model. The simulations also revealed that the re-circulation causes a local zone with elevated temperature. The experiment with the bubbling regime used a partially closed back-pressure valve. Here the re-circulation zone was also captured. In comparison to the experiment with the jetting regime, this experiment did not show a large over-heated region. The predicted temperature field featured a strong radial gradient rather than an axial gradient.

4.7.1 Recommendation

While the qualitative validation is useful as a first model validation, it is still not sufficient to claim that the model is properly validated. There are several improvements necessary that should be implemented in the model as well as the experimental setup.

Experimentally it would be recommended to simplify the steam injector design by removing the injection point and sensors at the bottom. This would enable the use of a laser to properly illuminate the channel for quantitative PIV data with fluorescent tracer particles. In addition it is recommended to invest in a fast high-resolution Infra Red (IR)-camera. This would provide insights into the temperature gradients and its dynamics.

The model improvements are mostly focussed on the multi-phase interaction. The applied method assumes a multiple-flow interaction profile. However, our experimental data reveal the existence of a clear steam cavity and dispersed gas. It would be interesting to develop a model that uses a Volume of Fluid (VOF) approach to simulate the steam cavity and combine it with a Continuous-Dispersed EMP model.

References

- [38] S.S. Safavi Nic, T.H.P. van Veen, K.A. Buist, R.E.M. Verdurmen, and J.A.M. Kuipers. “An objective classification of condensation regimes in Direct Contact Condensation”. *AIChE Journal* (Apr. 2023). DOI: <https://doi.org/10.1002/aic.18121>.
- [61] S.S. Safavi Nic, K.B. Buist, R.E.M. Verdurmen, and J.A.M. Kuipers. “Dynamic model to predict heat-induced protein denaturation and fouling in a Direct Contact Steam Condensation process”. *Chemical Engineering Science X* 8 (2020), pp. 841–855.
- [64] S.S. Gulawani, S.K. Dahikar, C.S. Mathpati, *et al.* “Analysis of flow pattern and heat transfer in direct contact condensation”. *Chemical Engineering Science* 64.8 (Apr. 2009), pp. 1719–1738. DOI: 10.1016/j.ces.2008.12.020.
- [65] A. Pecenko. “Numerical Simulation Methods for Phase-Transitional Flow”. PhD thesis. Eindhoven University of Technology, 2010. DOI: 10.6100/IR691427.
- [66] S.K. Dahikar, M.J. Sathe, and J.B. Joshi. “Investigation of flow and temperature patterns in direct contact condensation using PIV, PLIF and CFD”. *Chemical Engineering Science* 65.16 (Aug. 2010), pp. 4606–4620. DOI: 10.1016/j.ces.2010.05.004.
- [67] M.D. Koretksy. *Engineering and Chemical Thermodynamics*. Ed. by M.D. Koretksy. John Wiley and Sons, 2012, pp. 648–652.
- [68] A. Buffo, M. Vanni, P. Renze, and D.L. Marchisio. “Empirical drag closure for polydisperse gasliquid systems in bubbly flow regime: Bubble swarm and micro-scale turbulence”. *Chemical Engineering Research and Design* 113 (Sept. 2016), pp. 284–303. DOI: 10.1016/j.cherd.2016.08.004.
- [69] A. Tomiyama, I. Kataoka, I. Zun, and T. Sakaguchi. “Drag Coefficients of Single Bubbles under Normal and Micro Gravity Conditions”. *JSME International Journal Series B* 41 (Feb. 1998), p. 472. DOI: 10.1299/jsmeb.41.472.
- [73] S.S. Gulawani, S.K. Dahikar, C.S. Mathpati, *et al.* “Analysis of flow pattern and heat transfer in direct contact condensation”. *Chemical Engineering Science* 64.8 (Apr. 2009), pp. 1719–1738. DOI: 10.1016/j.ces.2008.12.020.
- [74] David C. Wilcox. *Turbulence Modelling CFD Wilcox*. 1994.
- [75] F.R. Menter. “Two-Equation Eddy-Viscosity Turbulence Models for Engineering Applications”. *AIAA JOURNAL* 32.8 (1994). DOI: 10.2514/3.12149.
- [76] L. trubelj and I. Tiselj. “Two-fluid model with interface sharpening”. *International Journal for Numerical Methods in Engineering* 85.5 (Feb. 2011), pp. 575–590. DOI: 10.1002/NME.2978.
- [77] W. Thielicke and E.J. Stamhuis. “PIVlab Towards User-friendly, Affordable and Accurate Digital Particle Image Velocimetry in MATLAB”. *Journal of Open Research Software* 2 (1 Oct. 2014). DOI: 10.5334/JORS.BL.

Chapter 5

Dynamic model to predict heat-induced protein denaturation and fouling in a Direct Contact Steam Condensation process

Abstract

High heat treatment, using Direct Contact Condensation (DCC), is applied in the production of dairy products to ensure a high level of food safety. During this process a protein rich deposit layer can be formed causing fouling of the system resulting in a loss of effective production time and an increase in cleaning cycles. The dynamics of the heat treatment process is modelled, including the description of the pre-heating step with two laminar flow tubular heat-exchangers followed by a DCC. In this system the bulk reactions for whey proteins are modelled using unfolding, re-folding and aggregation kinetics. The formation of the deposit layer is described in the segment after the DCC using a flow averaged model incorporating diffusion of species through the mass boundary layer as well as adsorption to the wall and desorption from the wall. The desorption kinetics are key as the protein deposit layer releases from the wall once the wall friction increases due to the decreasing area available for throughflow. The model shows good agreement with experimental data and is capable of capturing the process dynamics, both for the heat exchanger and the DCC. The deposit layer formation model is in agreement with the trend observed in the experimental data but is not fully capturing the process dynamics.

List of symbols

Symbol	Description	Units
v_z	Velocity axial direction	m/s
μ	Viscosity	Pa/s
P	Pressure	Pa
ρ	Density	kg/m^3
z	Axial coordinate	-
r	Radial coordinate	-
$\langle v \rangle$	Average velocity	m/s
D_h	Hydraulic diameter	m
$4f$	Fanning friction factor	-
λ	Thermal conductivity	$W/(K \cdot m)$
U	Heat transfer coefficient	$W/(K \cdot m^2)$
A_{shell}	Hydraulic area shell side	m^2
T^i	Temperature medium (M)/ product (P)	$^{\circ}C$
c_i	Concentration protein in state i	kg/m^3
k_i	Reaction rate	-
$\ln(k_{0i})$	pre-exponential factor	-
E_{ai}	Activation energy	J/mol
δ_h	Hydrodynamic boundary	m
d_h	Corrected hydrodynamic diameter	m
d_{h0}	Initial hydrodynamic diameter	m
c_F	Concentration deposited protein	kg/m^3
c_i^*	Concentration species i in the boundary layer	kg/m^3
a	Thermal diffusivity	m^2/s
ρ_f	Density deposit layer	kg/m^3
δ_f	Thickness deposit layer	m
k_m	Mass transfer coefficient	m/s
η	Dimensionless radius	-
ζ	Dimensionless length	-
c_{TP}	Total protein concentration	kg/m^3
$c_{pH4.6}$	Total protein after acidification	kg/m^3
c_{native}	Sum of the concentration native & unfolded protein	kg/m^3
β	Momentum correction factor	-
r_R	Rate of deposit release	m/s
β_R	Empirical release rate parameter	m/s

This chapter is based on S.S. Safavi Nic, K.B. Buist, R.E.M. Verdurmen, and J.A.M. Kuipers. Dynamic model to predict heat-induced protein denaturation and fouling in a Direct Contact Steam Condensation process. *Chemical Engineering Science X* 8 (2020), pp. 841855. [61].

5.1 Introduction

Heat treatment is applied in the food industry to ensure a certain level of food safety for the final product by inactivating micro-organisms and/or harm-full enzymes which naturally occur in the ingredients. The level of required food safety is strongly related to the target group of the product and is directly linked to the applied temperature and the duration at which this temperature is maintained. Fresh dairy products, for instance, require a minimum pasteurization time of 30 min at 69°C (or 30 seconds at 80°C). However, dairy products that need to remain stable on the shelf at ambient conditions require a more strict heat treatment in the temperature range of 135-150°C up to 5 seconds as to also destroy spore-forming bacteria [1–3]. The drawback of Ultra High Heat-Treatment (UHT) temperature regimes is the additional side reactions that may cause colour formation, loss of nutrients [5] and a reduced process efficiency [6–8]. The reduction in process efficiency is a result of the formation of a protein-rich deposit (fouling) layer, which increases the resistance for heat transfer. The consequences are a higher energy consumption to compensate for the loss in efficiency for energy transfer as well as an increase of the amount of cleaning cycles. Both of these have a significant impact on the sustainability of dairy processing as well as on the optimal utilization of processing equipment. To support the optimization of a dairy factory, we present a model based approach that properly describes the process of the heat induced denaturation as well as the mechanism and rate of formation of the deposit layer.

One of the main drivers for the deposit layer formation is the denaturation of whey proteins, in particular β -lactoglobulin. β -Lactoglobulin is a globular whey protein that, in its native form, is found in a tertiary structure. The tertiary structure is stabilized by several interactions such as; hydrogen bonds, hydrophobic interactions, electrostatic bond, disulfide bonds and Van der Waals forces. Upon heating the whey protein loses its native structure and unfolds to the secondary structure exposing the reactive thiol group thus enabling the aggregation of β -lactoglobulin, which can be referred to as denatured whey protein. The associated reaction pathway is schematically represented in equation 5.1. The prediction of the concentration profiles of native, unfolded and aggregated β -lactoglobulin is a key element in modelling protein fouling as the latter is correlated to the unfolded whey protein [10]. However, most reaction kinetic models either use a two-step reaction pathway without refolding [10, 78] or a one-step model lumping the native and unfolded protein together [79, 80]. The first method is limited as it predicts a lower concentration of native protein than measured [9] and the latter is not suited for use in fouling modelling as information on the unfolded, reactive protein is lost. An overview of the most relevant models, reported in literature, is provided in Table 5.1.



The protein fouling models [10, 79] focus mostly on the so-called type A deposit formation [34] which is mostly composed out of proteins, in particular whey proteins [81, 82]. It is commonly accepted that the type A deposit is formed in the temperature range of 75°C < T < 110°C [6, 10, 33, 34]. At higher temperatures a mineral rich deposit layer was observed, which is referred to as type B deposit [33, 34, 37]. Literature on protein induced fouling (type A) are mostly applicable in the temperature range of 75°C < T < 110°C. These models put emphasis on the thermal resistance build-up inside heat-exchangers for skimmed milk systems [10, 33, 35, 36] or pure whey protein systems [6, 83]. However,

in practice the operational limitations are not found in the heat exchangers where the increase of energy consumption is negligible. A more significant process limiting step is found in the steam injector where the unit is operated at constant outlet pressure. Due to the formation of the deposit layer the hydraulic diameter of the piping reduces, increasing the pressure drop and as a consequence increasing the steam pressure. The aim of this research paper is to present a reversible denaturation model combined with a fouling model that can predict the process performance as a function of steam pressure to the system.

Table 5.1: Overview of research on protein reaction modelling and protein fouling modelling.

Model purpose	Solution Method	Comments	Reference
Denaturation and fouling rates	Analytical	$70^{\circ}C < T < 90^{\circ}C$ 2 step reaction	[6, 10]
Denaturation and fouling rates	Analytical Empirical	$70^{\circ}C < T < 90^{\circ}C$ 1 step reaction Fouling empirical	[84]
Fouling UHT process	Empirical	Statistical, no reactions	[85]
Dynamic modelling	Numerical 1D transient	Fouling by aggregates	[35]
Dynamic modelling	Numerical 2D transient	Fouling by aggregates	[36]

5.2 Model description

To study the protein kinetics and fouling rates an OMVE-100 (Utrecht, The Netherlands) pilot scale UHT-process is used, as schematically represented in figure 5.1. The process consists of three tubular heaters, two for pre-heating and one for cooling. Each heat exchanger has its own supply of heating/cooling medium. After the second pre-heater the product enters the steam injector for sterilization and is maintained at the sterilization temperature for 5.6 seconds in a pipe. The flash-cooler is used to rapidly cool the product and as a consequence the added steam is extracted again. In this section the model for this process will be described. The model consist of three separate sections with an interconnected set of equations to allow for mass, momentum and heat transport. Firstly the governing equations for the heat exchanger will be described followed by the reaction mechanism and associated kinetics. Afterwards the numerical set-up of the DCC is described and finally the holding cell is modeled where the formation of the deposit layer is most critical, leading to an increase of the steam pressure which is of interest.

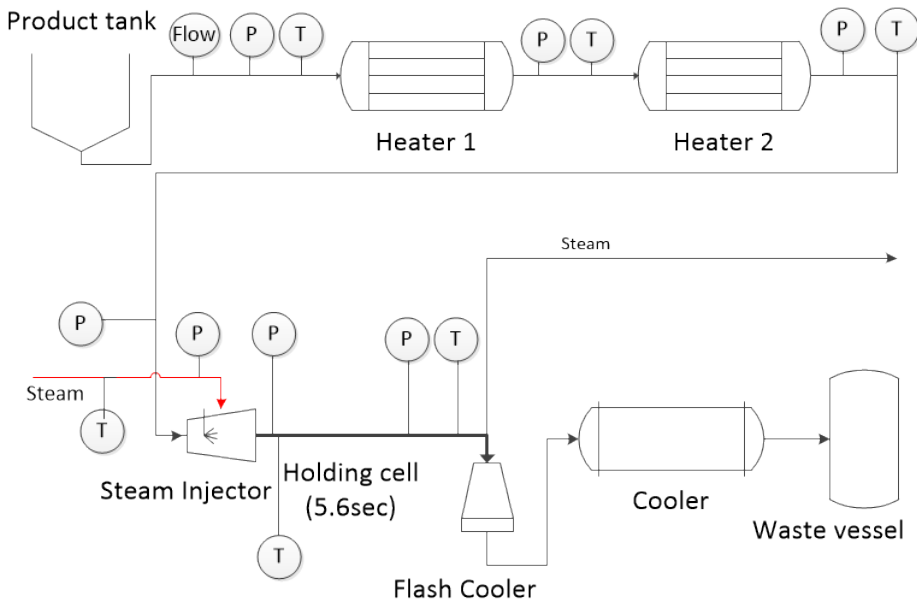


Figure 5.1: Schematic representation of the OMVE-100 pilot plant UHT-process

5.2.1 Heat exchanger

The pilot plant UHT line operates at laminar flow conditions with a maximum Reynolds number of $Re \sim 1900$ depending on the fluid temperature. A schematic description of the model in this section is represented in figure 5.2. For convenience a 2D flow model is used, assuming fully developed laminar flow in the domain $0 < r < R_1$. The heating medium is located in the domain $R_1 < r < R_2$ for which a 1D lumped model is sufficient.

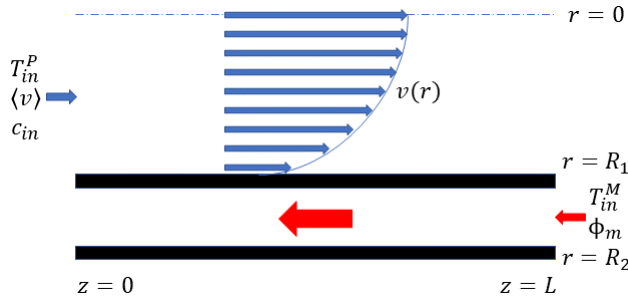


Figure 5.2: Schematic representation of the heat exchanger model. On the product side the velocity gradient is modelled assuming fully developed laminar flow in the domain $0 < r < R_1$. On the heating medium side a 1D model is applied assuming no gradients in radial direction.

Momentum balance

The simplified z -momentum balance is given by (5.2) which can be integrated once to obtain (5.3) for the domain $0 < r < R_1$.

$$0 = -\frac{\partial P}{\partial z} + \frac{1}{r} \frac{\partial}{\partial r} \left(r \mu \frac{\partial (v_z)}{\partial r} \right) \quad (5.2)$$

$$\frac{\partial (v_z)}{\partial r} = -\frac{r}{2\mu} \left(-\frac{\partial P}{\partial z} \right) \quad (5.3)$$

The velocity distribution depends on the pressure gradient which is given by the Fanning equation in differential form:

$$-\frac{\partial P}{\partial z} = 4f \frac{1}{D_h} \frac{1}{2} \rho \langle v^2 \rangle \quad (5.4)$$

Where the friction factor can be estimated from equation 5.5 for a Reynolds number $Re < 2100$.

$$4f = \frac{64}{Re} \quad (5.5)$$

$$Re = \frac{\rho \langle v \rangle D_h}{\mu} \quad (5.6)$$

Thermal energy balance

The transient thermal energy balance (equation 5.7) is applied on the domain $0 < r < R_1$ and accounts for convective as well as diffusive transport. With T^P representing the product temperature.

$$\frac{\partial T^P}{\partial t} = -v(r) \frac{\partial T^P}{\partial z} + a \left[\frac{1}{r} \frac{\partial}{\partial r} \left(r \frac{\partial T^P}{\partial r} \right) + \frac{\partial^2 T^P}{\partial z^2} \right] \quad (5.7)$$

On the product side three boundary conditions need to be specified. At the pipe entrance the temperature is equal to the inlet temperature.

$$[T^P]_{z=0} = T_{in}^P \quad 0 < r < R_1] \quad (5.8)$$

The boundary condition at the tube centre can be expressed using the symmetry assumption.

$$\left. \frac{\partial T^P}{\partial r} \right|_{r=0} = 0 \quad (5.9)$$

At the interface between the wall and the liquid the heat flux can be described using Newton's law of cooling. The heat flux at the wall requires as driving force the temperature difference between the heating medium (T^M) and the product temperature at the wall ($T^P(z, R_1)$).

$$\lambda \left. \frac{\partial T^P}{\partial r} \right|_{r=R_1} = U(z) [T^M(z) - T^P(z, R_1)] \quad (5.10)$$

The heating medium (usually water) has a flow rate around 500 l/hr and flows through a slot of roughly 5 mm. This will lead to a Reynolds number of approximately 22000 and consequently we use a simple lumped 1D model for the heating medium (5.11). With the mass flow rate (ϕ_m) and shell area (A_{shell}).

$$\rho A_{shell} c_p \frac{\partial T^M}{\partial t} = \phi_m c_p \frac{\partial T^M}{\partial z} - U \pi D (T^M(z) - T^P(z, R_1)) \quad (5.11)$$

With respect to the energy balance on the product side the convective energy transport term in equation 5.11 does not have the minus sign as the flow direction is in the opposite direction of the axial domain. As a result the boundary condition of the heating medium is located at the end of the axial domain.

$$T^M(z = L) = T_{in}^M \quad (5.12)$$

Analogous to the energy balance the mass balance of the product side can be formulated accounting for convective and diffusive transport. However for the species balance only diffusive transport in the radial direction is considered.

Mass balance and reaction kinetics

For the mass balance the adaptation of equation 5.7 leads to equation 5.13 in which the diffusion coefficient (D) is introduced, the concentration of component i (c_i) as well as the

reaction with the source/sink term (S_i). The boundary conditions are analogous to the temperature balance with the exception that there is no mass transfer at the wall.

$$\frac{\partial c_i}{\partial t} = -v(r) \frac{\partial c_i}{\partial z} + D \left[\frac{1}{r} \frac{\partial}{\partial r} \left(r \frac{\partial c_i}{\partial r} \right) \right] + S_i \quad (5.13)$$

The reaction mechanism assumes a first order reversible unfolding mechanism, the aggregation reaction is assumed to be pseudo-second order [10] with reaction only between unfolded whey proteins at an operation pH of 6.8 [30, 86].



This results in the following three step reaction model in which the reaction rates (r_i) can be substituted into the source/sink term of equation 5.13. It is important to note that the refolding reaction ($k_{-1}c_U$) is only applicable in temperature ranges up to 120°C[81].

$$\begin{bmatrix} r_N = -k_1 c_N + k_{-1} c_U \\ r_U = k_1 c_N - k_{-1} c_U - k_2 c_U^2 \\ r_A = k_2 c_U^2 \end{bmatrix} \quad (5.15)$$

The temperature dependence of the reaction rate can be estimated using the Arrhenius equations:

$$k_i = k_{0i} \exp \left(-\frac{E_{a_i}}{RT} \right) \quad (5.16)$$

The reaction rate constant for aggregation is classified to have a conditional switch for temperatures lower than $T < 90^\circ C$ (the unfolding limited regime) and for temperatures higher than $T > 90^\circ C$ (the aggregation limited regime) [13, 81, 87, 88].

5.2.2 Steam Injection

To reach sterilization temperatures an annular gap steam injector (figure 5.3) was used. The product enters the injector with a pipe diameter of 10 mm and is compressed to an injection nozzle with a diameter of 2 mm. The steam pipe (point 8) has a diameter of 14 mm and is compressed to an annular slit of 2 mm. The product and the steam are put in contact in the mixing chamber and the key assumption is that the steam is fully condensed at the end of the injector. To predict the pressure profile of this system, equation 5.4 is applied to calculate the pressure at each point. The losses in the Fanning equation were calculated by applying a momentum correction factor (β) between segments 4-5, the segment with the most sudden expansion [63].

5.2.3 Holding cell model

The purpose of the holding cell is to maintain a fixed temperature for a specific residence time. The deposit layer is most significantly formed in this segment of the process and causes the pressure in the system to increase. The process of the formation of the deposit layer consists of the following steps:

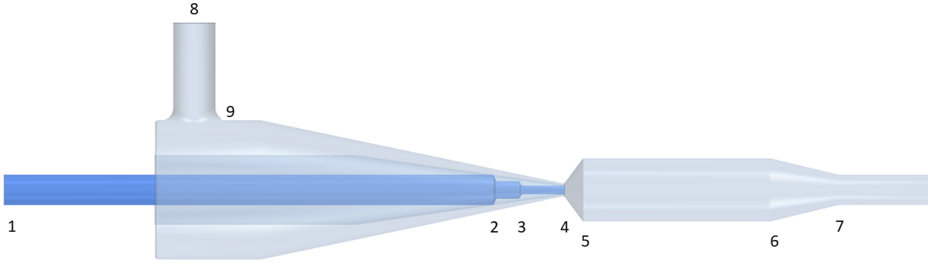


Figure 5.3: Schematic representation of the steam injector. The pressure drop between each segment is calculated using the steady-state Bernoulli equation. Segment 1-4: Initial product inlet to the injection nozzle. Segment 8-9-4: Inlet steam to the steam annulus. Segment 4-5: Inlet mixing chamber. Segment 5-6: Mixing/condensation chamber. Segment 6-7: Exit segment

- A bulk reaction for the unfolding, refolding and aggregation of the protein.
- Mass transfer through the hydrodynamic boundary (δ_h) [10, 35, 36].
- Deposit formation by the unfolded, reactive protein.
- Adjusted hydrodynamic diameter ($d_h = d_{h0} - \delta_f$).
- Increase in pressure drop.
- Increase in local velocity.

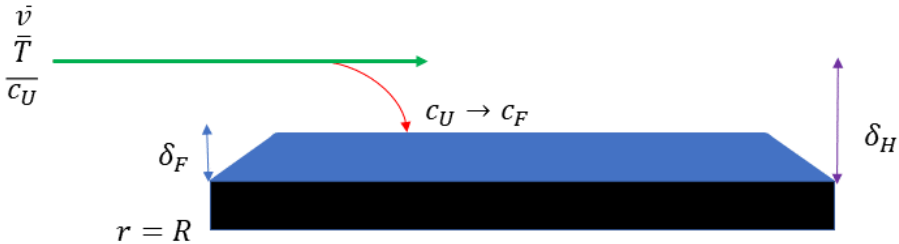


Figure 5.4: Schematic representation of the deposit layer formation process.

Due to the formation of the deposit layer it is not valid to assume a constant velocity profile. The average velocity ($\langle v \rangle$) is calculated locally using the adjusted hydraulic diameter from equation 5.17. It is assumed that steam is fully condensed, the temperature is fully developed and energy losses are neglected.

$$A_{h0} \langle v_0 \rangle = A_h \langle v \rangle \quad (5.17)$$

Due to the changes in hydrodynamic diameter it would not be appropriate to apply the Fanning equation to calculate the pressure profile. For this reason equation 5.18 is introduced assuming symmetry, transient behaviour and including the changes in kinetic

energy. Both the initial condition as well as the boundary condition follow the same approximation as equation 5.17.

$$\frac{1}{2}\rho \frac{\partial v^2}{\partial t} = -\frac{1}{2}\rho \left(\frac{\partial v^2 v}{\partial z} \right) - \frac{\partial pv}{\partial z} - 4f(z) \frac{\rho}{d_h} \frac{1}{2} v^2 v \quad (5.18)$$

The species balance (equation 5.13) is replaced by an equation (5.19) accounting for accumulation, convective transport and mass transport to the wall.

$$\frac{\partial c_i}{\partial t} = -v \frac{\partial c_i}{\partial z} - \frac{k_m}{m} (c_i - c_i^*) + S_i \quad (5.19)$$

The factor m represents the equilibrium concentration between the concentration of unfolded protein in the bulk and in the boundary layer with a value of 0.3 [10]. The adhesion to the surface is derived from previous work [10, 35, 36].

$$\rho_f \frac{\partial \delta_f}{\partial t} = k_f c_U^* \quad (5.20)$$

The mass transfer coefficient (k_m) can be approximated using the Sherwood correlation for laminar tube flow:

$$k_m = \frac{D}{\delta_H} \quad (5.21)$$

$$\text{Sh} = \frac{k_m d_H}{D} \quad (5.22)$$

Combining equation 5.21 and 5.22 results in the correlation for the thickness of the mass boundary layer.

The Sherwood number equation 5.23) for laminar flow has to be estimated taking into account the entrance length of the tube [89]. It is assumed that the flow doesn't fully develop due to the growth of the deposit layer.

$$\text{Sh} = 3.66 + \frac{0.065 \text{ReSc}}{1 + 0.04 \left(\text{ReSc} \frac{d_h}{\Delta x} \right)^{\frac{2}{3}}} \quad (5.23)$$

5.3 Model implementation and verification

5.3.1 Model implementation

The model has been implemented using gPROMS FormulatedProducts 1.4 using the flow-sheeting and custom model capabilities. The model has been implemented with the technical and numerical details listed in table 5.2. The physical properties are listed in table 5.4. The viscosity has been measured using an Anton Paar MCR102 (with a conical geometry CP50-1) and empirically correlated using equation 5.25 . The steam properties equations are derived from the steam thermodynamic table [90] (specified in table 5.4) and is valid up to a pressure of $p = 9$ bar. The density of the deposit layer was assumed to be the same as in previous publications [10]. The process conditions were used as set-points and listed in table 5.5 in which the injector entrainment ratio is defined as the mass ratio between the product and steam:

$$\omega = \frac{\phi_m^P}{\phi_m^S} \quad (5.24)$$

Table 5.2: Technical and numerical details of the tubular heat exchangers.

Length	
Heater 1	17m
Heater 2	21m
Cooler	21m
Holding cell	2.4m
Diameter	
Product tube diameter	10mm
Shell diameter	18mm
Holding cell	10mm
Discretization method Product side	
[Axial] Material, 1 st order	N=50
[Axial] Energy, 2 nd order	N=50
[Radial] Material & Energy, 2 nd order	M=50
Discretization method Shell side	
[Axial] Material & Energy, 1 st order	N=50

$$\mu = \sum_{i=0}^{N=5} b_i T^i \quad (5.25)$$

Table 5.3: Technical details of the steam injector. The length is specified for segments as specified in Figure 5.3. At the injection point (4) the steam side (S) and product side (P) are tagged respectively.

Segment	Length (mm)	D_{in} (mm)	D_{out} (mm)
1-2	147	10	10
2-3	8.5	10	6.5
3-4 _P	16	6.5	3
4 _P -5	5.9	3	22.5
5-6	64	22.5	22.5
6-7	23.1	22.5	10
8-9	49.2	14	14
9-4 _S	84.1	14	1

Table 5.4: Physical properties of the milk and steam.

Density	1030 kg/m^3
Viscosity	$b_0 = 0.00571 \text{ Pa} \cdot s$ $b_1 = -6.114 \times 10^{-6} \text{ Pa} \cdot s/^\circ C$ $b_2 = -3.83140 \times 10^{-6} \text{ Pa} \cdot s/^\circ C^2$ $b_3 = 1.24316 \times 10^{-7} \text{ Pa} \cdot s/^\circ C^3$ $b_4 = -1.39491 \times 10^{-9} \text{ Pa} \cdot s/^\circ C^4$ $b_5 = 5.56981 \times 10^{-12} \text{ Pa} \cdot s/^\circ C^5$
Steam temperature	$T_{steam} = 36.701 \ln(p) - 327.54 \text{ }^\circ C$
Steam enthalpy	$\Delta H = 43002 \ln(p) + 2181.8 \times 10^3 \text{ J/kg}$

Table 5.5: Process set-points. The actual values are logged and used as inputs for the simulation. The Injector entrainment ratio is a calculated value as a consequence of the DCC temperature set-point

Product flowrate	100 lt/hr
Heater 1 medium flowrate	415 lt/hr
Heater 1 Medium temperature in	63 $^\circ C$
Heater 2 medium flowrate	500 lt/hr
Heater 2 Medium temperature in	86 $^\circ C$
Back-pressure steam injector	3.8 barg
DCC temperature set-point	135 $^\circ C$
Injector entrainment ratio	22.5

5.3.2 Numerical verification

The implementation of the heat transfer model has been tested using firstly the classical transient thermal conduction case and secondly the steady-state case for convection-diffusion with a fixed wall temperature. The classical transient conduction case was obtained by assuming no flow in an infinite long cylinder with a fixed wall temperature (T_1) and a uniform temperature (T_0) across the radial domain.

5.3 Model implementation and verification

The analytical solution for this case (as represented by figure 5.5) introduces the dimensionless temperature (equation 5.26), time ($\tau = at/d^2$) and position ($\eta = r/R$) variables as well as Bessel functions (J_0 and J_1) of the first kind [91].

$$\Theta = \frac{T - T_0}{T_1 - T_0} \quad (5.26)$$

The verification results are shown in figure 5.5, showing a very good agreement between, the numerical model and the analytical model.

$$\Theta = 2 \sum_{n=1}^{\infty} \frac{1}{\beta_n J_1(\beta_n)} \exp(-\beta_n^2 \tau) J_0(\beta_n \eta) \quad (5.27)$$

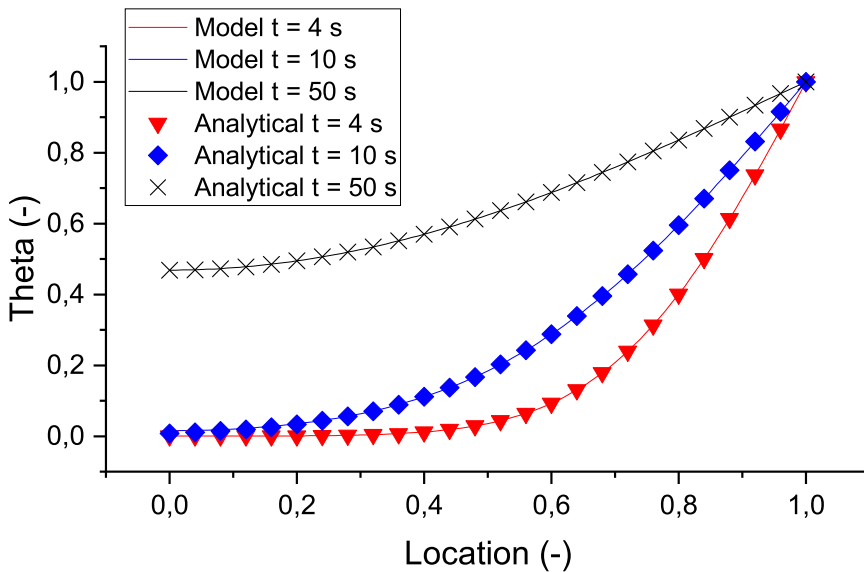


Figure 5.5: Evaluating numerical and analytical (x) results for the heat conduction test.

The second case for verification is the classical case of steady-state convection/diffusion in a tube with a fixed wall temperature. The aim is to calculate the (fully developed) Nusselt number and confirm for convergence to $Nu= 3.66$. The Nusselt value was estimated using equation 5.28 in which Θ_w represents the dimensionless wall temperature, Θ_b the dimensionless bulk fluid temperature and the dimensionless axial position ($\zeta = x/L$). The verification exercise clearly demonstrates (figure 5.6) that the numerical model has an asymptote for the Nusselt number at $Nu=3.66$.

$$Nu = \frac{2}{\Theta_1 - \Theta_b} \left. \frac{\partial \Theta}{\partial \zeta} \right|_{\zeta=1} \quad (5.28)$$

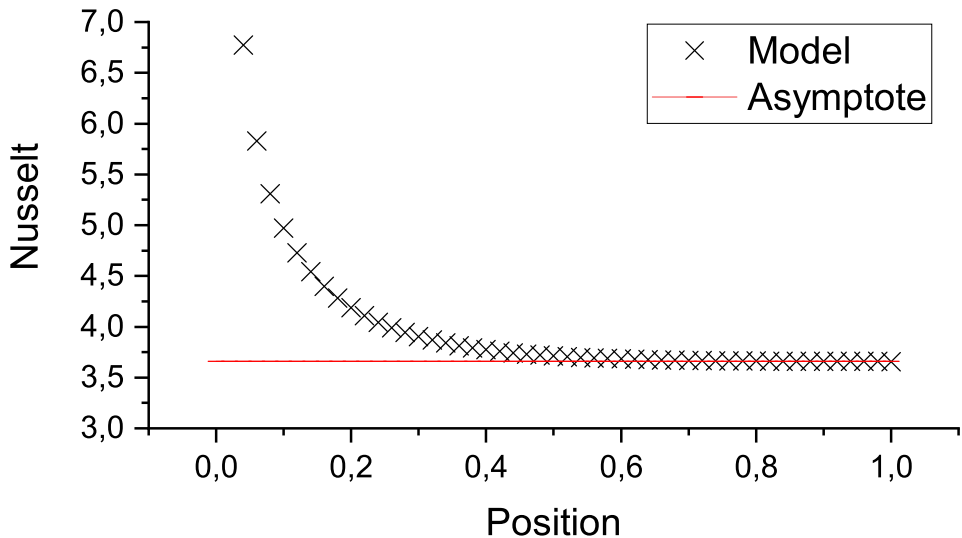


Figure 5.6: Nusselt number converges to an asymptote at $Nu= 3.66$.

5.4 Materials and methods

5.4.1 Materials

A model system for a dairy product at 30% total dry matter was made in demineralised water, the composition in listed in table 5.6. The pH of the formulation was adjusted to 6.8 using NaOH. For the acidification of the milk for the protein nativity analysis a 7M HCl solution was used. The pressure measurements in the UHT process were conducted with a Flush pressure sensor of IFM electronics (0.2% standard deviation) whereas the temperature was measured with a PT100 thermocouple (1%). Samples were drawn after each heating step in the process line using fully opened sample valves and drawing 50 mL. The experiments have been performed in duplo and per experiment three samples were drawn from the sample valve.

Table 5.6: Composition of the product matrix

Component	Composition (wt%)
Total Protein	5
Whey	3
Casein	2
Lactose	24
Minerals	1

5.4.2 Protein content measurement and degree of aggregation

The total protein concentration (c_{TP}) was measured using the method of Dumas using an Elementar Rapid Max N Exceed. The system was calibrated using Asparic acid and the reference sample was Infantrini, a commercially available product. The measurement requires a 300 mg sample contained in an aluminum sample holder and burned at 900°C. The gases were reduced and purified with activated carbon and the resulting nitrogen was analysed with a heat conductivity detector. The nitrogen concentration was converted to a protein concentration using a conversion factor of 6.25. The degree of aggregation/denaturation was determined by firstly acidifying the sample to pH 4.6 using 7M HCl solution, centrifuging at 20000 g for 30 min and then measuring the supernatant for total protein ($c_{pH4.6}$). The fraction native protein was then determined via equation 5.29 [Dumpler2016, 81, 87]. The protein fraction of the fouling layer was measured by firstly making a 15 wt% dry matter solution and then measuring the total protein. The deposit layer was collected by firstly opening the back pressure control valve followed by a pressurized rinse with cold demineralised water.

$$c_{native} = \frac{c_{pH4.6}}{c_{TP}} \quad (5.29)$$

5.5 Results and discussion

5.5.1 Heat transfer and reaction kinetics

First the simulation results for the heat transfer equipment will be presented, see Figure 5.7 where the temperatures of heaters 1 & 2 are shown. The calculation was initiated with steady-state solutions for both the energy and species balances. The input parameters for the simulations are the experimental flow rates and temperatures at the inlet on the product and the heating medium side. The experimental data was filtered with the Savitzky-Golay filter[92]. It can be observed that the model follows the dynamics of the inlet conditions and predicts accurately the outlet conditions.

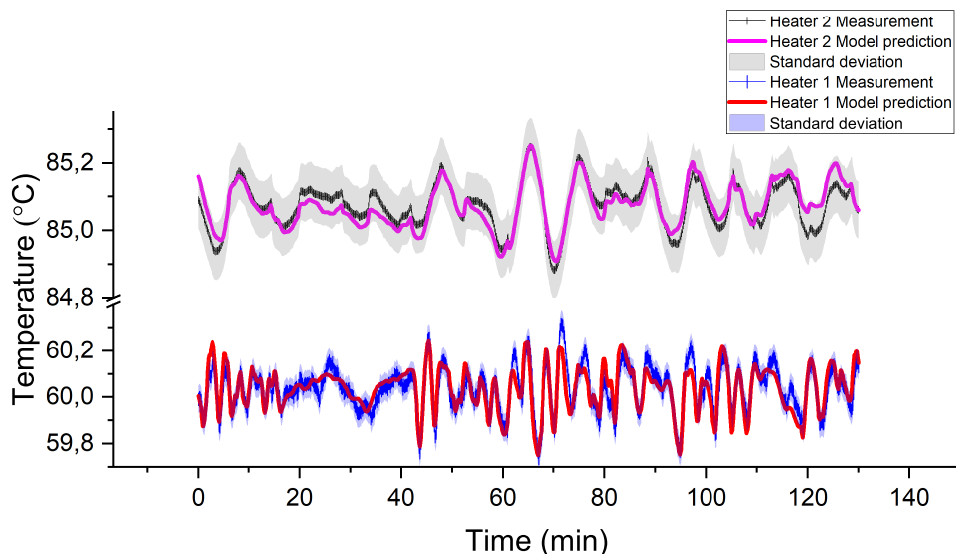


Figure 5.7: Model prediction (red) mapped against the temperature measurements (blue) as a function of time.

The results for the predicted protein nativity are shown together with the experimental data in Figure 5.8. The (small) initial difference between the predicted and measured protein nativity is due to variations in raw material. However, the relative standard deviation is smaller for these samples in comparison to the samples drawn later in the process (RSD=7%) which is an accumulative result of errors in the sampling and measurement. From the experimental data the kinetic parameters were estimated and given in Table 5.7. The obtained rate of aggregation is of a similar order of magnitude as found by other researchers [10, 78, 80, 81].

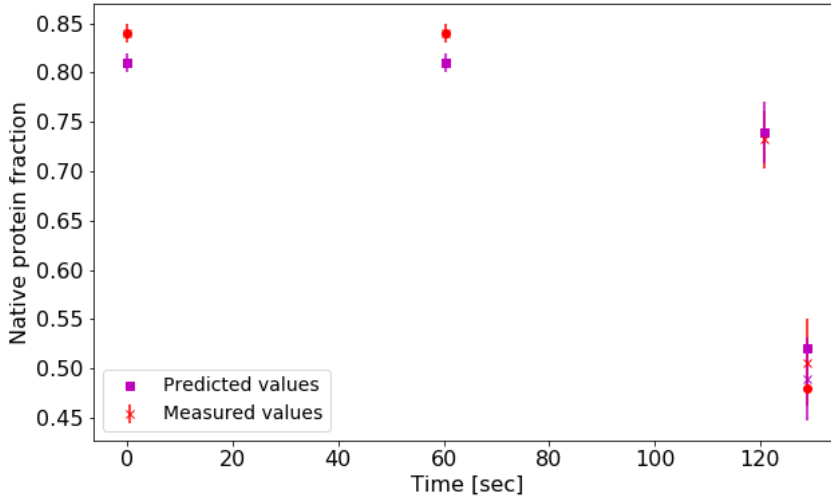


Figure 5.8: Predicted and measured native protein fractions as a function of the process residence time.

Table 5.7: Kinetic parameters fitted from the experimental data.

	Reaction type	E_{a_i} (kJ/mol)	$\ln(k_{0i})$
k_1	“Unfolding”	325.83	122.7
k_{-1}	“Re-folding”	177.4	70.96
k_2	“Aggregating” ($T < 90^\circ\text{C}$)	292.84	89.84
k_2	“Aggregating” ($T > 90^\circ\text{C}$)	51.17	9.82

The obtained reaction kinetics have been implemented into a flowsheet model of the overall process to predict the concentration profile of the whey protein throughout the process (Figure 5.9). It can be seen that the fraction native and unfolded cross around 70°C which is in line with previous research [93, 94]. The third reaction step, aggregation, is observed to start around 75°C which is also an acceptable temperature range [93, 95]. The refolding of the protein is most prominently observed during the cooling period, after the high heat-treatment, at which the fraction aggregated protein remains constant, fraction unfolded protein decreases and the fraction native (folded) protein increases. The sharp changes located at 125 seconds are a result of the rapid increase in temperature causing an accelerated reaction rate. The bends at the end of each heat-exchanger is a result of the boundary conditions. The outlet conditions are averaged and passed to the next model block.

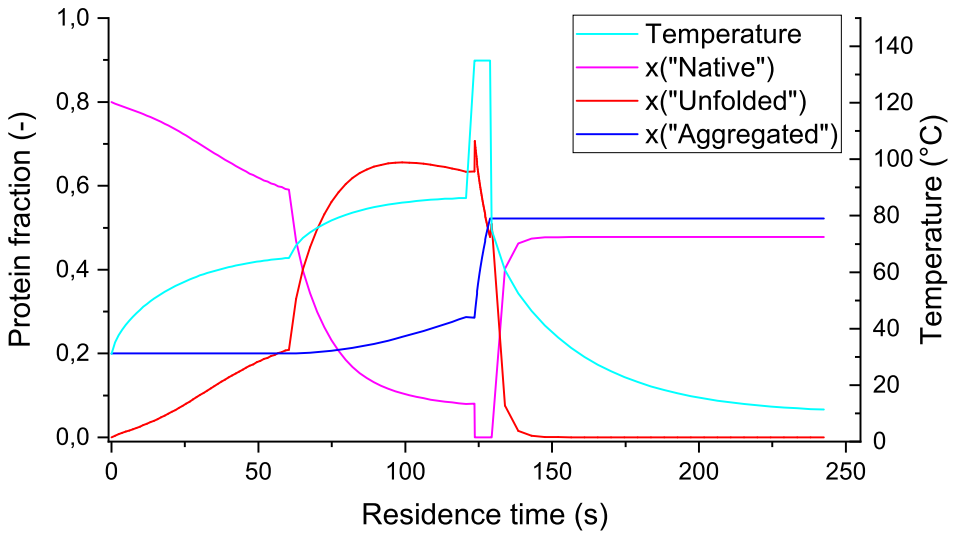


Figure 5.9: Prediction of the protein fractions as a function of temperature and the process residence time. The temperature profile and the fractions are averaged values. The sum of the protein fractions equals the total whey protein concentration.

5.5.2 Validation of steam injector and fouling model

The steam injector model was validated by comparing the predicted outlet pressure against the experimental data. The simulation was supplied with the pressure measurement on product and steam side before the injector and the outlet pressure of the steam injector was predicted and compared against experimental data, as shown in Figure 5.10. The simulation results are in good agreement with the experimental data and the momentum correction factor (β) is estimated to be 0.975.

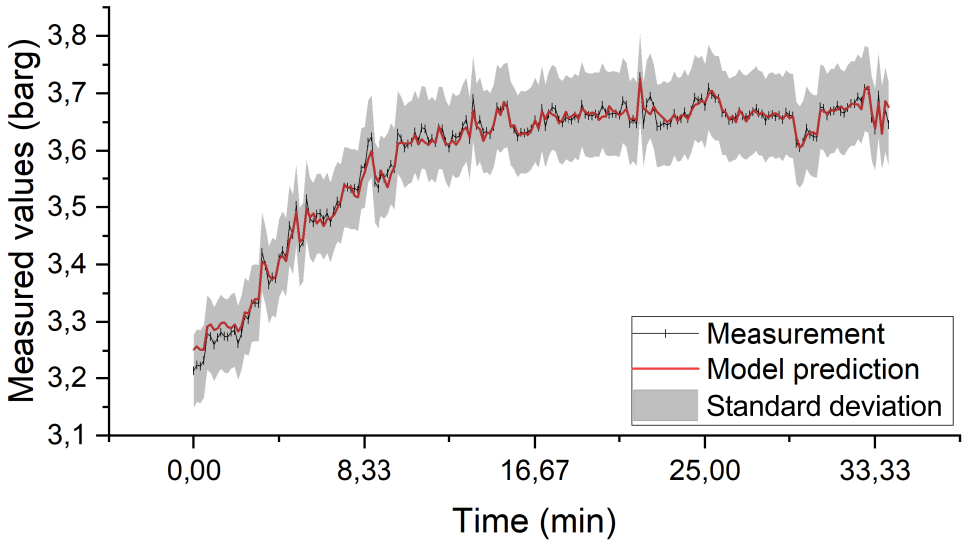


Figure 5.10: Predicted and measured outlet pressure of the steam injector as a function of the experimental run time. The model has been supplied with the inlet pressure, flow rate and temperature on the product side. The steam pressure and temperature was measured and the flow rate is calculated from the energy balance. The momentum correction factor is estimated to be $\beta = 0.975$

The composition of the deposit layer was determined in terms of dry matter and protein content (Table 5.8), yielding an average protein content of $66.37\% \pm 1.45\%$. This value is significantly higher than reported in previous studies where the deposit layer contained 15-20% protein for temperatures $T > 100^\circ\text{C}$ [33, 34, 37, 83]. The difference in composition of the fouling layer, can be attributed to a difference in heating rate. In many earlier studies analysis on the deposit layer has been performed at relatively low heating rates $1^\circ\text{C}s^{-1}$ and high Reynolds number [83, 96]. However, in this work, due to the constraints of the product formula the heating rate was $83.3^\circ\text{C}s^{-1}$ whereas the Reynolds number was relatively low. Moreover, the product composition of the referred research was either whole milk or skimmed milk which has a significantly different product matrix than used in this research. Due to the large differences in heating rates, flow regimes and product features a direct comparison with literature results is not appropriate.

Table 5.8: Composition of the deposit layer after dissolving in demi-water

Sample	Dry matter	Protein content
1	14.84 ± 0.24	10.07 ± 0.51
2	17.23 ± 0.23	11.19 ± 0.51

In figure 5.11 the predicted and measured steam pressure profiles are shown as a function of time for two different scenario's. The first only considers the adsorption of unfolded protein to the wall [10] whereas the second scenario, introduced in this study, the release

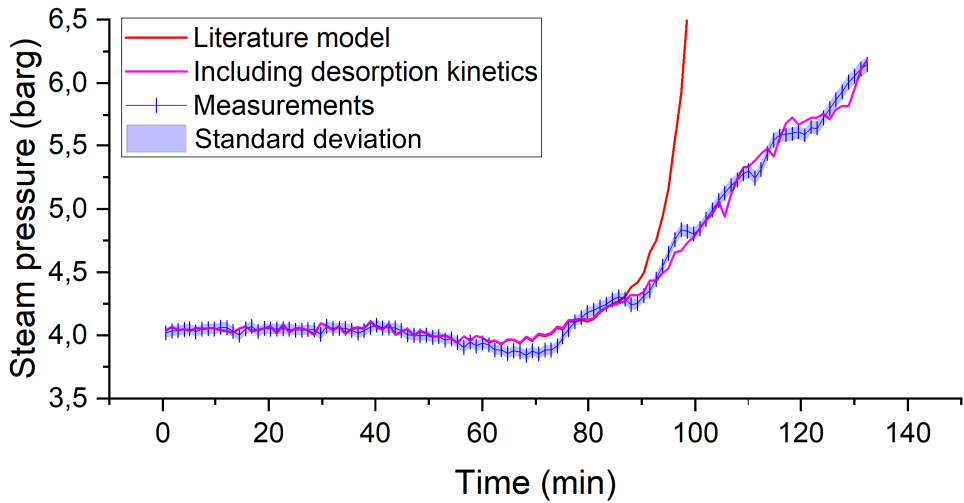


Figure 5.11: Comparison between the literature model [10] without desorption, proposed model and measured data as a function of time. Process set-points: Temperature $T = 135^{\circ}\text{C}$, 3.6 barg back-pressure.

of adsorbed protein into the bulk (Equation 5.30) is included. During the formation of the deposit layer the hydrodynamic area of the tube decreases resulting in an increase of the overall pressure drop as well as an increase in local velocity and skin friction at the wall. When the friction forces are stronger than the cohesion force of the deposit layer it can result in the sudden release of the deposit layer. This process has a strong dependency on the Reynolds number as well as on the composition of the product matrix. Due to a research gap on the physical properties of the deposit layer it is not possible to introduce a mechanistic model to incorporate this behaviour. Instead an empirical correlation (Equation 5.30) is introduced to describe the rate of desorption (r_R) as a function of the flow rate which includes a fit parameter (β_R) and the Reynolds number. With the inclusion of this parameter the exponential growth of the pressure profile can be damped and the disturbances can be introduced. The overall pressure increase is well captured by the model, however, the fluctuations are not captured with the same degree of accuracy as the thermal and mechanical balances presented earlier. In order to validate the desorption model the same experiment was executed with a target temperature of 150°C and the results are shown in Figure 5.12 together with the experiments with a 135°C DCC target temperature. It was found that the trend was again followed using the kinetic data estimated from the experiment at 135°C . The obtained reaction kinetics and the fit parameter are listed in Table 5.9.

$$r_R = -\beta_R \text{Re} \quad (5.30)$$

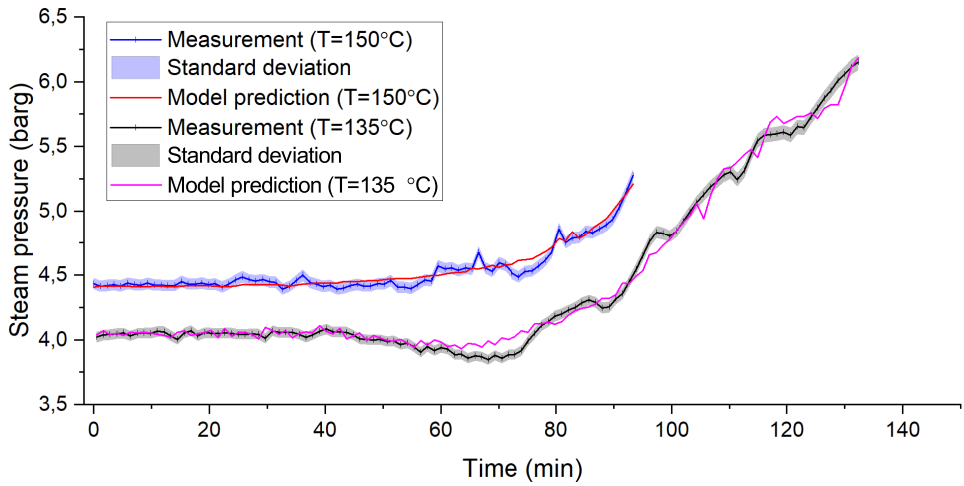


Figure 5.12: Comparison between simulation results at $T=135^{\circ}\text{C}$ and $T=150^{\circ}\text{C}$ and the corresponding experimental data. The kinetic parameters were fitted from the experimental data with $T=135^{\circ}\text{C}$ and used to simulate the experimental data at $T=150^{\circ}\text{C}$.

Table 5.9: Deposit layer adsorption and desorption kinetics fitted from the experimental data.

$\ln(k_0)$	3.61
E_{a_f}	$20.74 \text{ kJ mol}^{-1}$
β_R	$1.69 \times 10^{-6} \text{ m s}^{-1}$

5.6 Conclusion

Dairy products that need to remain food safe on the shelf at ambient conditions require a high heat treatment to ensure the right level of food safety. A sterilization process with Direct Contact Condensation (DCC) is often applied to satisfy the food safety criteria. During this process a protein rich deposit layer can be formed causing which can result in a loss of effective production time and an increase in cleaning cycles. In this chapter the dynamics of the heat treatment process have been modelled by describing the pre-heating as well as the high heat treatment step with the DCC. The model accurately represented the physical quantities such as the system pressure as well as the thermal performance of the tubular heat-exchangers. The reaction model proposed in this study includes a reversible unfolding reaction in which the protein loses/regains its tertiary structure as well as aggregation of the unfolded protein. The formation of the deposit layer is described by combining adsorption and desorption kinetics with the latter being a function of the Reynolds number. When the deposit layer builds-up the hydrodynamic area decreases causing an increase in wall friction which causes the release of the deposit layer. The model shows good agreement with experimental data and is capable of capturing the process dynamics, both for the heat exchanger and the steam injector. The deposit layer formation model is in agreement with the trend observed in the experimental data but is not fully capturing the process dynamics. The industrial relevance of this model is to predict process performance and efficiency. In future work it is recommended to research the material properties of the protein deposit layer in detail to improve the release rate model.

References

- [1] EFSA. “Opinion of the Scientific Panel on Biological Hazards on *Bacillus cereus* and other *Bacillus* spp in foodstuffs .” *The EFSA Journal* 1 (2005), pp. 1–48.
- [2] P.E. Granum and T. Lund. “*Bacillus cereus* and its food poisoning toxins”. *FEMS microbiology letters* 157.2 (1997), pp. 223–228.
- [3] A. Rajkovic, N. Smigic, and F. Devlieghere. “Contemporary strategies in combating microbial contamination in food chain”. *International Journal of Food Microbiology* 141 (2010), S29–S42.
- [5] M. Van Boekel. “Effect of heating on Maillard reactions in milk”. *Food Chemistry* 62.4 (1998), pp. 403–414.
- [6] P. Blanpain-Avet, C. André, M. Khaldi, *et al.* “Predicting the distribution of whey protein fouling in a plate heat exchanger using the kinetic parameters of the thermal denaturation reaction of β -lactoglobulin and the bulk temperature profiles”. *Journal of Dairy Science* 99.12 (2016), pp. 9611–9630.
- [7] P. de Jong, M.C. te Giffel, H. Straatsma, and M.M. Vissers. “Reduction of fouling and contamination by predictive kinetic models”. *International Dairy Journal* 12.2-3 (2002), pp. 285–292.
- [8] T. Davies, S. Henstridge, C. Gillham, and D. Wilson. “Investigation of whey protein deposit properties using heat flux sensors”. *Food and Bioproducts processing* 75.2 (1997), pp. 106–110.
- [9] B. Malmgren, Y. Ardö, M. Langton, *et al.* “Changes in proteins, physical stability and structure in directly heated UHT milk during storage at different temperatures”. *International dairy journal* 71 (2017), pp. 60–75.
- [10] P. de Jong. *Modelling and optimization of thermal processes in the dairy industry*. Delft University of Technology: ISBN:90-9009034-7, 1997.
- [13] E. Leeb, N. Haller, and U. Kulozik. “Effect of pH on the reaction mechanism of thermal denaturation and aggregation of bovine β -lactoglobulin”. *International Dairy Journal* 78 (2018), pp. 103–111.
- [30] A.J. Vasbinder and C.G. De Kruif. “Casein–whey protein interactions in heated milk: the influence of pH”. *International dairy journal* 13.8 (2003), pp. 669–677.
- [33] J. Visser and T.J. Jeurnink. “Fouling of heat exchangers in the dairy industry”. *Experimental Thermal and Fluid Science* 14.4 (1997), pp. 407–424.
- [34] H. Burton. “Reviews of the progress of dairy science”. *Journal of Dairy Research* 33 (1966), pp. 225–243.
- [35] M.C. Georgiadis and S. Macchietto. “Dynamic modelling and simulation of plate heat exchangers under milk fouling”. *Chemical Engineering Science* 55.9 (2000), pp. 1605–1619.
- [36] S. Guan and S. Macchietto. “A Novel Dynamic Model of Plate Heat Exchangers Subject to Fouling”. 43 (2018), pp. 1679–1684.
- [37] C. Hagsten, A. Altskär, S. Gustafsson, *et al.* “Composition and structure of high temperature dairy fouling”. *Food Structure* 7 (2016), pp. 13–20.

References

- [61] S.S. Safavi Nic, K.B. Buist, R.E.M. Verdurmen, and J.A.M. Kuipers. “Dynamic model to predict heat-induced protein denaturation and fouling in a Direct Contact Steam Condensation process”. *Chemical Engineering Science X* 8 (2020), pp. 841–855.
- [63] H. Ma, H. Zhao, L. Wang, Z. Yu, and X. Mao. “Modeling and investigation of a steam-water injector”. *Energy Conversion and Management* 151.May (2017), pp. 170–178. DOI: 10.1016/j.enconman.2017.08.068.
- [78] D.J. Oldfield, H. Singh, M.W. Taylor, and K.N. Pearce. “Kinetics of denaturation and aggregation of whey proteins in skim milk heated in an ultra-high temperature (UHT) pilot plant”. *International Dairy Journal* 8.4 (1998), pp. 311–318.
- [79] P. Blanpain-Avet, C. André, M. Khaldi, *et al.* “Predicting the distribution of whey protein fouling in a plate heat exchanger using the kinetic parameters of the thermal denaturation reaction of β -lactoglobulin and the bulk temperature profiles”. *Journal of dairy science* 99.12 (2016), pp. 9611–9630.
- [80] M. Khaldi, T. Croguennec, C. André, *et al.* “Effect of the calcium/protein molar ratio on β -lactoglobulin denaturation kinetics and fouling phenomena”. *International dairy journal* 78 (2018), pp. 1–10.
- [81] A. Tolkach and U. Kulozik. “Reaction kinetic pathway of reversible and irreversible thermal denaturation of β -lactoglobulin”. *Le Lait* 87.4-5 (2007), pp. 301–315.
- [82] M. Wolz and U. Kulozik. “Thermal denaturation kinetics of whey proteins at high protein concentrations”. *International dairy journal* 49 (2015), pp. 95–101.
- [83] M. Khaldi, G. Ronse, C. André, *et al.* “Denaturation kinetics of whey protein isolate solutions and fouling mass distribution in a plate heat exchanger”. *International Journal of Chemical Engineering* 2015 (2015).
- [84] T. Truong, K. Kirkpatrick, and S. S.G. “Role of β -lactoglobulin in the fouling of stainless steel surfaces by heated milk”. *International Dairy Journal* 66 (2017), pp. 18–26.
- [85] D.M. Phinney, A. Feldman, and D. Heldman. “Modeling high protein liquid beverage fouling during pilot scale ultra-high temperature (UHT) processing”. *Food and bioproducts processing* 106 (2017), pp. 43–52.
- [86] S.G. Anema. “Effect of pH on the viscosity of heated reconstituted skim milk”. *International Dairy Journal* 14 (2003), pp. 541–548.
- [87] R.J. Delahaije, H. Gruppen, E.L. van Eijk- van Boxtel, L. Cornacchia, and P.A. Wierenga. “Controlling the ratio between native-like, non-native-like, and aggregated β -lactoglobulin after heat treatment”. *Journal of agricultural and food chemistry* 64.21 (2016), pp. 4362–4370.
- [88] T. Nicolai, M. Britten, and C. Schmitt. “ β -Lactoglobulin and WPI aggregates: formation, structure and applications”. *Food Hydrocolloids* 25.8 (2011), pp. 1945–1962.
- [89] A. Mills. *Heat transfer*. ISBN:0139476245. New Jersey: Prentice-Hall, 1999.
- [90] M.D. Koretsky. “Engineering and chemical thermodynamics” (2012), pp. 648–652.
- [91] R. Bird Byron, E. Stewart Warren, and N. Lightfoot Edwin. *Transport phenomena*. ISBN:9780470115398. New York: John Wiley and Sons, 2006.

- [92] J. Luo, K. Ying, and J. Bai. “Savitzky–Golay smoothing and differentiation filter for even number data”. *Signal Processing* 85.7 (2005), pp. 1429–1434.
- [93] A.M. Joyce, A. Brodkorb, A.L. Kelly, and J.A. OMahony. “Separation of the effects of denaturation and aggregation on whey-casein protein interactions during the manufacture of a model infant formula”. *Dairy science & technology* 96.6 (2017), pp. 787–806.
- [94] D. Mulvihill and M. Donovan. “Whey proteins and their thermal denaturation-a review”. *Irish Journal of Food Science and Technology* 11.1 (1987), pp. 43–75.
- [95] H.B. Wijayanti, N. Bansal, and H.C. Deeth. “Stability of whey proteins during thermal processing: A review”. *Comprehensive Reviews in Food Science and Food Safety* 13.6 (2014), pp. 1235–1251.
- [96] C. Hagsten, N. Loren, L. Hamberg, *et al.* “A novel fouling and cleaning set-up for studying the removal of milk deposits produced during UHT-treatment”. *International Conference on Heat Exchanger Fouling and Cleaning*. 2013, pp. 457–464.

Chapter 6

Epilogue

6.1 Conclusions

Dairy products that need to remain food safe on the shelf at ambient conditions require a high degree of heat treatment to ensure the right level of food safety. A high-heat treatment (HHT) process with Direct Contact Condensation (DCC) is often applied to satisfy the food safety criteria. During this process a protein rich deposit layer can be formed which can result in a loss of effective production time and an increase in cleaning cycles. The work reported in this thesis has been aimed at understanding and modelling the complex multiphase flow for DCC, especially to generate methods to optimize the design & operation of a HHT line. Experimental and computational methods have been employed to study the complex and dynamic condensation behaviour of steam in a cross flow injector. The computational methods have been developed such that large time scales can be resolved at low computational cost. In addition a CFD model has been employed to study the transport phenomena inside the injector and allow optimization of the geometry. Finally a full HHT process was simulated to predict protein denaturation and fouling.

In chapter 2, an experimental campaign was conducted to investigate which parameters play a role in the direct steam condensation process. The results were processed using an image analysis protocol to obtain relevant steam cavity properties and further processed with machine learning models to provide objective classification and regime prediction possibilities. The experimental campaign yielded 299 experiments with 79 different logged variables and 2000 frames recorded per experiment that were used to generate the regime maps. It was also found that it is important to properly note, besides steam pressure, the channel pressure as it has a significant effect on the condensation regime boundaries. In addition machine learning algorithms were employed of which the LDA is the superior classification model with 96% accuracy, being able to both classify regimes in an objective fashion and predict the regime for new samples. A parameter study was performed via the inspection of the linear discriminants, which led to the insight that the outlet Prandtl number is a good predictor for condensation regimes. Besides the Prandtl number, the steam pressure, channel pressure, subcooling, velocity ratio are better variables for regime maps than steam mass flux and inlet temperature respectively. It is recommended to use steam pressure and subcooling as key variables for regime maps and to report the channel pressure. This method also proved scalable to a dual injection setup leading to the introduction of new regimes. The second jet influences the temperature gradients to such an extent that the two jets show oscillating behaviour, which has been classified as

"Interfacial oscillation".

In chapter 3, a transient one-dimensional two-fluid model based on a multiple flow regime was presented. The model was designed to predict the performance and gradients inside a steam injector at low computational costs. The benefit of such an approach is that it could be used in a flow-sheeting environment in which the entire HHT process can be simulated. The model was validated using both steady-state conditions as well as transient conditions. In all conditions the average of the last three sensors was taken in order to obtain a proper basis for comparison. The steady state validation showed that the model is accurate in its predictions. Whilst the model demonstrated good agreement for the dynamic tests it also proved to be limited in conditions in which the steam cavity is small and the flow becomes heterogeneous. This indicates that the model is well-suited for steam injector designs and operational conditions in which the fluids are well-mixed and feature plug flow behaviour.

In chapter 4, a Computational Fluid Mechanics model was presented using a commercial package. The employed model used a Eulerian Multiphase (EMP) approach with a multiple-flow regime topology. The model was validated against PIV data generated using a high-speed camera and PIVlab for its analysis. The PIV data could only be used for a qualitative validation as a consequence of the lighting method that had to be adopted to illuminate the particles. In addition the formation of large gas bubbles in experiments with an open back pressure valve leads to unreliable velocity data. Nevertheless the CFD model demonstrated similar flow patterns, vortical flow structures and directionality. In addition it allowed the analysis of the temperature gradients in more detail. It was found that for open back pressure experiments (conditions in which the 1D model is accurate) there is a formation of a local hot-spot as a consequence of recirculation. It also became clear that for experiments with an elevated back-pressure the local hot-spot disappears but that the temperature is no longer homogenous in the radial direction, which is in line with the conclusions found in chapter 3. The CFD model, whilst needing more validation and development, shows potential in investigating the dynamics inside the steam injector and optimizing its design.

In chapter 5, the dynamics of the heat treatment process have been modelled by describing the pre-heating as well as the high heat treatment step with DCC. The reaction model proposed in this study includes a reversible unfolding reaction in which the protein loses/regains its tertiary structure as well as aggregation of the unfolded protein. The formation of the deposit layer was described by combining adsorption and desorption kinetics with the latter being a function of the Reynolds number. The model shows good agreement with experimental data and is capable of capturing the process dynamics, both for the heat exchanger and the steam injector. The deposit layer formation model is in agreement with the trend observed in the experimental data but is not fully capturing the process dynamics.

6.2 Outlook

The work reported in this thesis has made a contribution to experimentally investigating the condensation mechanism of steam in water and its associated modelling. There are still aspects that future studies should address to further advance this study, both experimentally and numerically. The experimental work reported in chapter 2 regime maps did not consider the impact of high-viscous fluids. When dealing with high-protein dairy products the viscosity is significantly higher than that of water [97, 98]. Moreover, due to heating the viscosity is expected to increase [86]. Investigating sensitivity of the regime map towards viscosity (changes) is relevant as it would indicate that a *product-specific* approach would be required in the operation of the DSI. It can be anticipated that when the viscosity increases that the steam cavity has more difficulty to penetrate into the liquid causing a shift of the regime maps to the right.

In chapter 3 a transient one-dimensional model was proposed. The model demonstrated to be of good accuracy and capable to handle the dynamic features. It can be industrially relevant to extend this model with the denaturation and fouling model presented in chapter 5. This would add to the model complexity but can also increase the accuracy of the predicted protein concentrations. Another relevant upgrade to the model is to include a microbial growth [7, 99, 100] and inactivation model [4]. The application of such a model is to simulate the entire HHT process and identify the optimal process conditions between product quality, food safety and process efficiency.

The CFD model presented in chapter 4 showed qualitatively to be in good agreement with experimental data. However, the validation could be improved significantly by adjusting the steam injector design. The design should be simplified by removing the injection point and sensors at the bottom of the injector. This would enable the incorporation of a glass window for including a laser sheet for the PIV analysis. It has to be noted that by removing the sensors at the bottom it would become difficult to assess if the temperature profile is fully developed. Using a high-speed InfraRed (IR) camera could overcome this and also support the validation of the predicted temperature profiles. The model itself could improve by changing the multiphase strategy from Eulerian Multiphase with multiple-flow regimes to a Volume Of Fluid (VOF) approach to simulate the steam cavity. The remaining of the multiphase interaction can then be represented using a Continous-Dispersed (CD) method. This offers the benefit that the steam cavity will be better described. The CD method has the advantage over the multiple-flow regime that it reduces from 9 closures to 3 in total (Nusselt and drag correlations).

The model presented in chapter 5 focussed on dairy proteins. Currently the market segment of plant-based products increasing and new products aimed to serve as a proper high-protein substitute are emerging. There is a need to grow the knowledge of the heat induced changes of these products and to predict the fouling rate of these products. This will support in accelerating product development but also up-scaling production (capacity) and increasing first-time-right. The main challenge for plant-based proteins is that it lacks the rich literature database that dairy proteins have. It is recommended to employ data-driven models next to experimental analysis to rapidly identify mechanisms and generate mechanistic models.

References

- [4] J.v. Doornmalen and K. Kopinga. “Temperature dependence of F-D- and z-values used in steam sterilization process”. *Journal of applied microbiology* (2009), pp. 1054–1060.
- [7] P. de Jong, M.C. te Giffel, H. Straatsma, and M.M. Vissers. “Reduction of fouling and contamination by predictive kinetic models”. *International Dairy Journal* 12.2-3 (2002), pp. 285–292.
- [86] S.G. Anema. “Effect of pH on the viscosity of heated reconstituted skim milk”. *International Dairy Journal* 14 (2003), pp. 541–548.
- [97] Ö. Cokun, N. Raak, and M. Corredig. “Heat induced interactions in whey protein depleted milk concentrates: Comparison of ultrafiltration and microfiltration”. *Food Hydrocolloids* 137 (2023), p. 108354. DOI: <https://doi.org/10.1016/j.foodhyd.2022.108354>.
- [98] E.G. Murphy, J.T. Tobin, Y.H. Roos, and M.A. Fenelon. “The effect of high velocity steam injection on the colloidal stability of concentrated emulsions for the manufacture of infant formulations”. *Procedia Food Science* 1 (2011). 11th International Congress on Engineering and Food (ICEF11), pp. 1309–1315. DOI: <https://doi.org/10.1016/j.profoo.2011.09.194>.
- [99] L. Rosso, J. Lobry, and J. Bajard S.and Flandrois. “Convenient model to describe the combined effects of temperature and pH on microbial growth”. *Applied and environmental microbiology* (1995), pp. 610–616.
- [100] M. Zwietering, I. Jongenburger, F. Rombouts, and K.v.’. Riet. “Modeling of the bacterial growth curve”. *Applied and environmental microbiology* (1990), pp. 610–616.

List of publications

Journal articles

- S.S. Safavi Nic, T.H.P. van Veen, K.A. Buist, R.E.M. Verdurmen, and J.A.M. Kuipers. An objective classification of condensation regimes in Direct Contact Condensation. *AIChE Journal* (Apr. 2023)
- S.S. Safavi Nic, T.E. Kuipers, K.B. Buist, R.E.M. Verdurmen, and J.A.M. Kuipers. A transient mechanistic two-fluid model for Direct Contact Condensation. *Chemical Engineering Science* (2023)
- S.S. Safavi Nic, K.B. Buist, R.E.M. Verdurmen, and J.A.M. Kuipers. Dynamic model to predict heat-induced protein denaturation and fouling in a Direct Contact Steam Condensation process. *Chemical Engineering Science X* 8 (2020), pp. 841855.

Acknowledgements

To my wife, Cindy van de Vries. She always made fun of me whenever I had to travel 2 hrs to get to Eindhoven, making the remarks that I could have also stayed close to home (Delft). Her teasing always went hand-in-hand with love and support.

Back in fall 2017, when I was already working for over a year at Danone, I realised that I needed to continue my academic development. When I told this to Roel Moonen and Ruud Verdurmen, back then my managers, they directly supported me. Together we brainstormed about topics and with which academic partner. Special thanks goes to Ruud. Not only did you provide mental support, you also were very enthusiastic about the subject and gave valuable technical insights. I learned from you how to be a better process technologist and also how to be effective in a turbulent environment such as Danone. What made you a great leader was that you always gave a platform to your team-members to present to senior management. This gave a great boost to my dedication but also personal development. Thank you for mentoring me and believing in me.

After several interviews at various universities I found an agreement with Hans Kuipers. From the moment I pitched the project, Hans was enthusiastic and willing to supervise me. He always trusted my dedication and supported me throughout the project. I could never have completed my thesis without this. I am truly grateful for your supervision.

Right after starting I met Kay Buist and he was on-boarded as my *daily* supervisor. I have come to know Kay as a relaxed guy who gives a lot of autonomy and freedom to his students. At the same time he is always available when you need him. Even if it is just to chat about *martial arts*. We matched good and I have really enjoyed our time together.

One of the criteria of my project is that I wanted to also do experimental work. However, having two left hands, I am a disaster in a lab (or with anything practical). At home this is compensated by my wife and her father, who are obviously not available for the work at the University. Luckily I had brilliant technical people that were able to translate my ideas into reality. With help from the staff of the pilot plant of Nutricia Research and in particular Pieter Brons and Perry Belt we managed to move several pieces of equipment to Eindhoven. They also supported and advised in integrating the equipment into the experimental set-up we had designed. In Eindhoven I was lucky to work Joop Aarts. Joop has great technical insights, great humor and a great personality. With Joop we were able to create a robust setup that was the foundation of all of my publications. I should also mention the staff of the EPC lab of Eindhoven. They redesigned and improved my steam injector. These great technical minds made sure that I had a leak proof (I don't want to think about the amount of mopping I have done..) and high-quality experimental set-up .

Acknowledgements

As a part time PhD candidate it can sometimes be a challenge to find the right time to fully execute the experimental work. I was therefore lucky to work together with young talented students. The first one I want to mention is Dirk Buiter. The master thesis of Dirk was highly turbulent. When he started we had a lab that was under construction and half way through his thesis the first Corona wave hit us. From one day to another our lives came to a halt and everything, including the university, was closed. We redesigned his thesis giving it a numerical focus so that the impact on his thesis was limited. Dirk did set the foundation of the experimental work. Until the last experiments his original design for data collection and storage was used.

Afterwards the project was picked up by several other students such as Gloria Spijkers, Bob de Haas, Vilena Petrova, Thirza Kuipers, Meike Rijdsdijk, Tijmen van Veen and Jordy Vogels. With Tijmen we took an exciting step by including Machine Learning algorithms. Tijmens idea was not without risk because it came late in his project and we invested a lot of time in it. The investment payed itself back in the form of a publication in AIChe Journal and a chapter in this book. Tijmen was a phenomena to work with. I learned a lot from you and had a lot of fun, especially during the pubquiz.

I also want to extend special thanks to Thirza and Meike. Working with Thirza was really enjoyable. Not only because she delivered great work but also because she is full of energy, the bright light in each room. When I was working with Meike I sometimes forgot that she was a bachelors student at the time. She had the maturity level of a masters student.

I should not forget the people from Siemens that provided me support and advice. On the Star-CCM+ side there was Roman Thiele. He showed me how to work with the program, offered advice and debugged my model. On the PSE side there have been Andrew Salmon, David Slade, Silei Xiong, Leteris Charakleias and Caleb Murray.

Research always comes with set backs. Sometimes with a lot and with high frequency. I hope for all researchers that, when these times come, they have the same level of support as I had. In addition to the people already mentioned I gained a lot of energy from my friends and colleagues that always encouraged me to endure and push through the rough period. Thanks to Arend, Martijn van der Hoeven, Martijn de Munck, Katerina, Sara, Gabrie, Thomas. You provided a listening ear, emotional support and when I needed it: a kick to my *****.

I also want to thank the PhD's from the research group and in particular my paranimfs: Amir and Martijn.

I can't put in words what this achievement means for me. When I was growing up people always told me, that as a foreigner, I should just go for a labour position, start working and earn my lives upkeep. I am grateful for those around me that saw my potential and encouraged me to utilize and develop it. Mevrouw van Mill, mijn biologie docent die zich extra heeft ingezet om mij door te laten stromen van het Roncalli Mavo naar het Emmauscollege. Bij het Emmauscollege kreeg ik veel bijles van Koos Valkenier en Christiaan van der Veeke. Koos Valkenier heeft met zijn natuurkunde bijles de fundering gelegd voor mijn voorliefde voor transport verschijnselen.

In my educational lifetime I have collected many degrees. From VMBO until now a PhD. I endured setbacks, made great friends, had great times and above all I learned and developed myself. It gives me a lot of joy to develop myself and learn and I will keep doing this. On top of it I now can enter a phase in my live in which I can contribute to the development and learnings of my son and future children. This may even proof to be more rewarding.

Curriculum Vitae

Sherwin Safavi Nic was born on October 1st, 1990 in Teheran (Iran). At an age of 3 years, he fled together with his family to the Netherlands. After completing his elementary and secondary school, he studied Molecular Sciences and Technology at Leiden University and Delft University of Technology. In 2014 he started his Master Chemical Engineering at Delft University. His masters degree was completed in 2015 with a thesis titled “Separating Lactic Acid by means of Reactive Extraction”.

After his graduation, Sherwin started in May 2016 at Danone Nutricia Research as a Process Technologist. In this role he developed a model library to simulate the production process of Infant Milk Formulations (IMF). As part of his personal development, he started a PhD project in the Multi-scale Modelling of Multiphase Flows group of Prof. dr. ir. Hans Kuipers under the supervision of dr. ir. Kay Buist, of which the results are presented in this thesis. After completing his PhD Thesis, Sherwin continues his research efforts at Danone.



Chapter 7

Appendix A

Table 7.1: Features used in data set for models.

Parameter	Symbol	Unit
Liquid inlet temperature	$T_{L,in}$	°C
Subcooling	$\Delta T_{subcool} = T_{L,in} - T_{G,in}$	°C
Steam mass flux	G	kg/(m ² s)
Liquid inlet Reynolds number	$Re_{L,in}$	-
Steam inlet pressure	$P_{G,in}$	bar
Channel pressure	$P_{channel}$	bar
Channel pressure coefficient of variation	$CV_{P,channel} = \frac{\sigma_{P,channel}}{P_{channel}}$	-
Normalized penetration length	PL	-
Normalized steam plume area	A_G	-
Penetration length coefficient of variation	CV_{PL}	-
Steam plume area coefficient of variation	$CV_{A,G}$	-
Liquid temperature near the injector	$T_{L,inj}$	°C
Liquid outlet temperature	$T_{L,out}$	°C
Temperature increase	$\Delta T_{out-in} = T_{L,out} - T_{L,in}$	°C
Inlet liquid specific heat capacity	$c_{P,L,in}$	J/(kgK)
Outlet density	$\rho_{L,out}$	kg/m ³
Outlet viscosity	$\mu_{L,out}$	kg/(ms)
Outlet enthalpy	$H_{L,out}$	J
Outlet entropy of phase i	$S_{L,out}$	J/K
Outlet internal energy of phase i	$U_{L,out}$	J
Outlet specific heat capacity	$c_{P,L,out}$	J/(kgK)
Outlet speed of sound of liquid	$c_{L,out}$	m/s
Outlet thermal conductivity	$k_{L,out}$	J/(mKs)
Outlet surface tension	$\sigma_{L,out}$	J/m ²
Outlet liquid reduced pressure	$P_{R,out}$	-
Liquid outlet mass flow rate	$\dot{m}_{L,out}$	kg/s

